Fall 2013

A Novel Multiblock Immersed Boundary Method Enabling High Order Large Eddy Simulation Of Pathological And Medical Device Hemodynamics

Anupindi Kameswararao
Purdue University

Graduate School ETD Form 9
(Revised 12/07)

PURDUE UNIVERSITY
GRADUATE SCHOOL
Thesis/Dissertation Acceptance

This is to certify that the thesis/dissertation prepared

By Anupindi, Kameswararao

Entitled
A NOVEL MULTIBLOCK IMMERSED BOUNDARY METHOD ENABLING HIGH ORDER LARGE EDDY SIMULATION OF PATHOLOGICAL AND MEDICAL DEVICE HEMODYNAMICS

For the degree of Doctor of Philosophy

Is approved by the final examining committee:

Prof. Steven H. Frankel
Chair

Prof. Jie Shen

Prof. Gregory Blaisdell

Prof. Farshid Sadeghi

Prof. Jun Chen

To the best of my knowledge and as understood by the student in the *Research Integrity and Copyright Disclaimer (Graduate School Form 20)*, this thesis/dissertation adheres to the provisions of Purdue University's "Policy on Integrity in Research" and the use of copyrighted material.

Approved by Major Professor(s): Prof. Steven H. Frankel

Approved by: Prof. Dave Anderson 9/19/2013
Head of the Graduate Program Date

A NOVEL MULTIBLOCK IMMERSED BOUNDARY METHOD ENABLING HIGH ORDER LARGE EDDY SIMULATION OF PATHOLOGICAL AND MEDICAL DEVICE HEMODYNAMICS

A Dissertation

Submitted to the Faculty

of

Purdue University

by

Kameswararao Anupindi

In Partial Fulfillment of the

Requirements for the Degree

of

Doctor of Philosophy

December 2013

Purdue University

West Lafayette, Indiana

To my mom, dad and sister

ACKNOWLEDGMENTS

At the outset, I would like to thank my PhD adviser Prof. Steven H. Frankel, for his continuous support, providing me with freedom to explore new emerging research areas, his motivating ideas and discussions, patience, keeping me busy, and constant presence through the online world throughout my studies and research work. His untiring efforts to learn and understand new things and to experiment and try out emerging simulation tools and technologies have always amazed me. I am indebted to him for several opportunities that he provided me such as encouraging me to attend and present my research at several conferences. Acknowledgments are due to Purdue University for creating such a nice and conducive atmosphere that has made my studies, research and overall stay very enjoyable. I would like to thank all the Professors who taught me at Purdue through several courses that I have taken. I am thankful to Prof. Gregory Blaisdell, Prof. Jie Shen, Prof. Jun Chen and Prof. Farshid Sadeghi for readily agreeing to serve on my PhD advisory committee and providing me with their valuable suggestions and guidelines.

Many thanks go out to the Center for Compact and Efficient Fluid Power (CCEFP), Caterpillar Inc., Purdue School of Mechanical Engineering, Technology Assistance Program (TAP) at Purdue, Med Institute, West Lafayette, and National Institute of Health (NIH) for their financial support during my entire course of studies at Purdue. I would also like to acknowledge the computational time provided on several parallel clusters of Information Technology at Purdue (ITAP) and Ohio Super Computer (OSU), without which the research work accomplished in the present research would not have been possible.

I acknowledge the help received from the secretarial staff in Chaffee Hall and in Mechanical Engineering, especially, Mrs. Charlotte Bell, Mrs. Jacqueline Baumgardt, Mrs. Julayne Moser, Mrs. Cathy Elwell, and Mrs. Michelle Sarault. I am also grateful

for the support I received from the Office of International Students and Scholars (ISS) at Purdue University for making my entire stay hassle free.

I would like to thank all my labmates and friends who made my research and personal life at Purdue a memorable one. Acknowledgments are due to Dr. Dinesh Shetty, and Dr. Travis Fisher for free rides to Chaffee, suggestions and help on understanding the earliest version of the WenoHemo solver they wrote. I cannot thank enough my friends Vaibhav Bhutoria, Dr. Niranjan Ghaisas, Dr. Yann Delorme, Abhro Pal, Qian Li, Dr. Nagendra Dittakavi, Weichen Lai, Jeffrey Kennington, Jonathan DeGan for their several helpful suggestions and discussions on both research and personal front. My sincere thanks are due to all my current and previous roommates, members of team Asha for all their help and lively conversations that kept me going happily with my routine everyday. Many thanks go out to Chetan Bajaj, Bhagirath Duvvuri, Dr. Varun Kulkarni, Sumeet Kumar, Anup Mohan, Pratikash Panda, Nikhil Sangwan, Astitva Tripathi and Ajit Vallabhaneni for their friendship and support. Special thanks go out to Madhav Pernankil, my friend and classmate from undergrad, who tirelessly called me up to just get an informal weekly update and save me from the busy week for a while through his funny and informative discussions.

Finally, I would like to thank my family for their love and support. Throughout my studies, my parents, sister, uncles and aunts have been very supportive and patient.

TABLE OF CONTENTS

Page

LIST OF TABLES

LIST OF FIGURES

Figure Page

Figure Page

ABSTRACT

Anupindi, Kameswararao Ph.D., Purdue University, December 2013. A novel multiblock immersed boundary method enabling high order large eddy simulation of pathological and medical device hemodynamics. Major Professor: Steven H. Frankel, School of Mechanical Engineering.

Computational fluid dynamics (CFD) simulations are becoming a reliable tool in understanding disease progression, investigating blood flow patterns and evaluating medical device performance such as stent grafts and mechanical heart valves. Previous studies indicate the presence of highly disturbed, transitional and mildly turbulent flow in healthy and pathological arteries. Accurate simulation of the transitional flow requires high order numerics together with a scale resolving turbulence model such as large eddy simulation (LES). This in turn limits one to use a structured fluid flow solver on which complex, branching arterial domains that are typical in the human blood circulatory system could not be handled. To overcome this, a novel multiblock based immersed boundary method (IBM) is developed based on high order discretization schemes that can efficiently simulate blood flow in complex arterial geometries using structured Cartesian fluid flow solvers. The developed solver, WenoHemo, is systematically validated for each of the newly introduced numerics using a variety of numerical and experimental results available in the literature. Three dimensional laminar flow over a sphere, laminar flow in a backward facing step, laminar and transitional flow in an abdominal aortic aneurysm (AAA), transitional flow in a model stenosed artery, and turbulent flow in a mixing layer are used as benchmark cases for validating the solver thoroughly.

WenoHemo is then applied to study blood flow patterns in a pathological thoracic aortic aneurysm (TAA) and in a resulting thoracic aorta with a stent graft (TASG) geometry after an endovascular repair (EVAR). Phase averaged velocity profiles, tur-

bulence kinetic energy levels, viscous wall shear stresses and turbulence energy spectra are used to compare the similarities and differences between the blood flow patterns obtained. Presence of well developed turbulence is detected in the case of TAA whereas TASG showed periodic vortex shedding with lower turbulence levels and improved blood flow to the descending aorta. Application of the solver to simulate blood flow patterns obtained in a bi-leaflet mechanical heart valve (BMHV) placed in a model aorta with imposed kinematics of the leaflets is also carried out, which reveals complex blood flow patterns that need to be considered in the design of the same for reliability and to reduce post surgical complications.

1. INTRODUCTION

1.1 Motivation

The main motivation for the present work is to understand the blood flow patterns in physiologically relevant pulsatile inflow conditions in pathological arteries as well with those treated with a medical device solution. The present research focuses on simulating hemodynamics in two important but different categories of pathological blood flow that medical community is faced with. The first problem falls in the category of endovascular repair of an aortic aneurysm and the second one is related to a leaky natural heart valve that is replaced with a mechanical heart valve. In what follows, we provide quick introduction to both the problems and defer the detailed discussion until later in the respective chapters to follow.

An arterial aneurysm is a local, permanent dilation of the blood vessel. The likelihood that an aneurysm will rupture is influenced by its size, and expansion rate. Aortic aneurysms constitute the 14^{th} leading cause of death in the United States [1]. Endovascular repair (EVAR) of aneurysms has become a widespread treatment option for aortic diseases, as an alternative to open surgery [2]. In EVAR stent grafts are placed in the artery, excluding blood flow to the aneurysm, which prevents their rupture. However, post EVAR complications arise, such as stent graft migration, and endoleak. These complications cause severe pressure build up in the aneurysm region. Simulations of blood flow in pathological and medical device implanted arteries can provide insights into the disease progression (such as the expansion rate, and wall shear stress distribution) and the forces that act on the stent grafts. Computational fluid dynamics (CFD) simulations can provide valuable information to the medical device manufacturers and surgeons in making critical decisions in the treatment of aortic aneurysm repair.

Natural heart valves may become leaky because of age or an acquired disease owing to plaque formation. Leaky heart valves cannot hold blood during the diastolic phase as a result the primary function of the heart to pump oxygenated blood is not accomplished. Depending on the severity of the leakage and urgency of the need medical intervention is prescribed. This results in replacing the natural heart valves with either a tissue or biological heart valve or with a mechanical heart valve. There are several types of mechanical heart valves that are available in the medical device manufacturing market and none of them are perfect when it comes to reliability in the long run. It is very difficult if not impossible to test and monitor the health and function of the mechanical heart valves when implanted in a subject. The motivation of the present work is that understanding the blood flow dynamics in a mechanical heart valve will provide valuable information into the environments they are subjected to.

1.2 Cardiovascular Fluid Mechanics

The working fluid that transports oxygen, nutrients and waste in the human body is blood. Blood is a complex mixture of cells, proteins, lipoproteins, and ions [3]. Approximately 40% of the blood is occupied by red blood cells. Red blood cells are semisolid particles and affect the properties and behavior of the blood by increasing its viscosity. The viscosity of blood is a function of the flow rate and blood exhibits non-Newtonian behavior in the micro-circulatory system. The non-Newtonian behavior is most prominent in very low shear rate regions when the red blood cells clump together forming a large particle. Apart from the low shear rate regions, the non-Newtonian behavior is observed in small branches, and capillaries. However, in most arteries blood behaves as Newtonian fluid, and its viscosity can be taken as a constant [3]. In the present study the dynamic viscosity of blood is taken to be equal to 3.5 centipoise.

The cardiovascular system is a closed loop circulatory system that can be divided into the systemic circulation supplied by the left ventricle (LV) and the pulmonary

circulation supplied by the right ventricle (RV). The arteries are the larger blood vessels that carry the oxygenated blood from the heart to the micro circulation in the tissue to be perfused and then the veins carry the venous blood back to the heart [4]. The cardiovascular system typically features a low Reynolds number (Re) pulsatile flow due to the cyclic pumping motion of the heart. The heart ejects and fills the blood in alternating cycles called *systole* and *diastole*. Blood is pumped out of the heart during systole, and heart rests during the diastole, and no blood is pumped out. Because of this the blood flow and pressure are unsteady and pulsatile through out the cardiovascular system with varying values of pulsation. The presence of unsteady or pulsatile flow virtually through out the cardiovascular system makes the fluid flow problem an unsteady problem by including the local acceleration term. The typical Re range of blood flow in a healthy circulatory system varies from 1 in the small arteries to approximately 4000 in the largest artery, the aorta [3]. Pulsatile flows are characterized through a non-dimensional number known as Womersley or Witzig parameter, $\alpha = R\sqrt{\omega/\nu}$, where, R is the radius of the pipe, ω is the circular frequency of the pulsation, and ν is the kinematic viscosity of the fluid [3]. This is same parameter used in the similarity transformation developed in the well-known Stokes' Second Problem in fluid mechanics, in which the flow is induced by an oscillating flat plate [3, 5]. The Re being defined as the ratio of the inertia forces to the viscous forces, the Womersley parameter α can be interpreted as the ratio of the unsteady forces to the viscous forces. When the Womersley parameter is low the viscous forces dominate, velocity profiles are parabolic in nature, and the center line velocity in the pipe oscillates in phase with the driving pressure gradient. For Womersley parameters above 10, the unsteady inertial forces dominate, and the flow is essentially one of piston like flow motion with a flat or plug velocity profile. The amplitude of motion decreases at the higher frequencies, and there is a 90° phase shift between the driving pressure gradient and the flow velocity, similar to a low-pass filter [3].

In contrast to unsteadiness, several features of biological flows may be neglected in some situations as secondary in importance. These properties include vessel wall

elasticity, non-Newtonian viscosity, slurry particles in the fluid, temperature effects. These features of secondary importance are neglected in the present study as it simplifies the analysis greatly.

1.3 Background

There have been various studies of blood flows in aorta. In this section we provide a brief overview of various past studies that were conducted on abdominal and thoracic aortic aneurysms. Asbury et al. [6] experimentally investigated steady inflow in rigid models of abdominal aortic aneurysm (AAA). They performed laser Doppler velocimetry and color Doppler flow imaging on seven rigid models with a variety of diameter ratios of artery to the aneurysm. They observed a core of relatively fast moving fluid in the center of the dilation, surrounded by an outer annulus of slowly recirculating fluid. They concluded that there was a tendency for the larger models of aortic aneurysms to become turbulent at lower Re than the smaller models. In their study, the largest models produced turbulent velocity fluctuations as great as 40% of the mean center line velocities. Morris et al. [7] performed numerical simulations of blood flow through models of human aorta using commercial fluid dynamics software FLUENT 6.0. A pulsatile velocity inflow condition was used by the authors, and three different aortic arch configurations were constructed from the spiral computerized tomography (CT) scan of the aorta obtained from a single subject. All their thoracic aorta models did not have the peripheral arteries and hence there is only one inlet at the aortic arch and one outlet in the descending aorta region. The velocity profiles obtained in the aortic arch were different among the models owing to the fact that the aortic arch radius was different between them to begin with. However, in the descending aorta region all the models showing similar velocity profiles. They observed greatest recirculation and reverse flow regions during the maximum deceleration phase, due to the fact that a decelerating fluid is more unstable than an accelerating fluid. Salsac et al. [8] studied experimentally the spa-

tial and temporal distribution of wall shear stresses (WSS) during various stages of the aneurysm development, by constructing models with varying values of diameter ratios. The evolution of WSS and its gradient are important in understanding the aetiology, and progression of the aneurysm diseases, as they affect the wall structure integrity. They conclude that, the flow separation and the associated formation of a strong vortex ring and of internal shear layers lead to regions of perturbed stress distribution, which do not exist in a healthy abdominal aorta. Varghese et al. [9,10] performed direct numerical simulations (DNS) of steady and pulsating blood flow in a stenosed artery configuration. Stenosis forms the other extreme condition compared with an aneurysm. In stenosis, the arterial wall becomes constricted and thereby causing a pathological condition of the artery that needs to be treated. Recent, and seemingly first large eddy simulation (LES) study of blood flow in a subject specific thoracic aorta was performed by Lantz et al. [11]. They studied the distribution of low density lipoprotein (LDL) on the surface of the aorta using the commercial CFD package CFX, under physiological conditions of pulsating inflow conditions. They investigated the relationship between WSS and LDL surface concentration and found that the accumulation of LDL correlated well with WSS. In general, regions of low WSS correspond to regions of increased LDL concentration and vice versa. Biasetti et al. [12] performed numerical simulations of blood flow in patient-specific models of AAA, with a motivation to find possible correlation between the vortical structures (VS) and intra-luminal thrombus (ILT) formation. Aortic aneurysms are frequently characterized by the development of an ILT, which is known to have multiple biochemical and bio-mechanical implications. There have been many other studies that were performed utilizing experimental and/or computational tools for the investigation of hemodynamics, and the list discussed here is not complete. However, the most common feature, among the computational studies is that, they employ low order (first order) numerics to study hemodynamics in complex geometries with potentially transitional/mildly turbulent flows which may not capture the physics correctly. There

have been very few studies, which employed high order accurate solvers with an emphasis on validation. The present work is a step in that direction.

1.4 Objectives

Blood flow in pathological arteries is shown to be transitional and or mildly turbulent [9–11,13]. Simulation of turbulent fluid flow requires a high order solver with an accurate subgrid scale (SGS) model. Therefore the primary objective of the present work is to develop, test, and validate a high order LES solver that is capable of simulating hemodynamics in complex arterial flows. We validated several aspects of the developed solver, such as the immersed boundary method (IBM), the multiblock approach, the flow field obtained from pulsatile inflow conditions. The SGS model used has already been validated in the previous studies by Shetty et al. [14]. We also simulate a turbulent mixing layer and validate the results with those obtained in experiments.

Another objective of the present research is to apply the developed solver to study blood flow dynamics in a pathological and medical device solution arteries. To accomplish this two important problems that medical community is facing with are studied. The first one is related to identifying similarities and differences in blood flow patterns and the overall effect of stent graft on blood flow dynamics when implanted in a subject. The second one is resulting blood flow dynamics in an artery fitted with a mechanical heart valve.

1.5 Organization

An overview of the organization of the present document is presented in this section. Chapter 2 presents the computational methodology used in the present work. It starts with a description of the governing equations pertinent to the present problems of interest, and then the sub-grid scale modeling details are presented. The review and selection of the IBM is also presented in this chapter. It concludes with a

description about the multiblock methodology that is implemented, the parallelization strategy, and the details about the statistical averaging as applied to data reduction of the steady and pulsatile inflow conditions.

In Chapter 3 a thorough validation of the developed WenoHemo solver is presented. Laminar three dimensional simulation of flow over a sphere, laminar three dimensional simulation of flow over a backward facing step, transitional flow in a model stenosed artery, and finally turbulent flow in a mixing layer with and without cavitation are considered as benchmark cases and the results obtained are compared with the numerical or experimental data available in the literature.

Chapter 4 starts with an introduction to the blood flow circulatory system followed by anatomy of the human aorta, aneurysms, and their treatment procedures are presented. Thereafter simulations of AAA are presented under both laminar and turbulent regimes for steady inflow at a Reynolds number of 500 and 2600. The results obtained are compared to the experimental results available in the literature. To demonstrate the capability of the WenoHemo solver to handle complex geometry a steady inflow in a thoracic aortic aneurysm (TAA) case is considered, which is of academic interest, and the obtained flow field is studied at Reynolds numbers of 910 and 3727 which correspond to an average flow and peak flow conditions in a physiologically relevant pulsatile inflow condition profile. Finally, the clinically relevant problem of pulsatile inflow to TAA and thoracic aorta with stent graft (TASG) are considered to study the similarities and differences obtained in blood flow patterns.

Chapter 5 presents simulations performed for a bi-leaflet mechanical heart valve (BMHV) placed in a model aorta for both steady and pulsatile inflow conditions. The steady simulation considers fixed leaflets at maximum opening angle whereas the pulsatile inflow condition considers animated leaflets with imposed kinematics.

Chapter 6 contains directions for future work that can be considered in each of the several areas such as further enhancements to the WenoHemo solver, studies on TAA/TASG and studies on BMHV.

2. COMPUTATIONAL METHOD

2.1 Governing Equations

The governing equations for the present problem are the incompressible Navier-Stokes equations. In LES, these are filtered using a low-pass spatial filter and they are summarized below in non-dimensional form:

$$\frac{\partial \overline{u_i}}{\partial t} + \overline{u_j}\,\frac{\partial \overline{u_i}}{\partial x_j} = -\frac{\partial \overline{p}}{\partial x_i} + \frac{1}{Re}\,\frac{\partial^2 \overline{u_i}}{\partial x_j \partial x_j} - \frac{\partial \tau_{ij}}{\partial x_j} + g_i \tag{2.1}$$

$$\frac{\partial \overline{u_i}}{\partial x_i} = 0 \tag{2.2}$$

where u is the velocity vector, p is the fluid pressure, τ_{ij} is the sub-grid scale (SGS) stress tensor, Re is the Reynolds number, g_i is the gravitational acceleration vector, and the filtered quantity of variable ϕ is denoted in the equations 2.1,2.2 by $\overline{\phi}$. The SGS stress tensor τ_{ij} shown in the equation 2.1, represents the difference between filtered velocity product and the product of filtered velocities, and given by,

$$\tau_{ij} = \overline{u_i u_j} - \overline{u_i}\,\overline{u_j} - \frac{1}{3}(\overline{u_i u_j} - \overline{u_i}\,\overline{u_j}). \tag{2.3}$$

The residual stress tensor or SGS stress tensor shown above only contains the anisotropic part and the isotropic part is absorbed into the filtered pressure field and the modified filtered pressure is,

$$\overline{p} = \overline{p} + \frac{1}{3}(\overline{u_i u_j} - \overline{u_i}\,\overline{u_j}). \tag{2.4}$$

2.2 Numerical Methodology

A high order accurate LES solver developed and validated for fully inhomogeneous turbulent flows by Shetty et al. [14], is augmented with IBM, and multiblock to handle fluid flows arising in complex geometries. The key aspects of the numerical methods used in the solver WenoHemo are discussed here. For a complete explanation of the

numerical methods, readers are referred to the article by Shetty et al. [14]. The convective acceleration terms are discretized using a fifth-order weighted essentially non-oscillatory scheme (WENO) [15], and the viscous terms are discretized using the standard fourth-order central difference scheme. In order to maintain the order of accuracy of the spatial discretization even at the boundaries, ghost nodes lying outside the domain are made use of. The values at the ghost nodes are updated using a Stokes flow boundary condition described in Morinishi et al. [16].

The governing equations are integrated using a fractional time stepping algorithm, which solves the equations in a predictor-corrector manner. The velocity values are predicted with out considering the pressure gradient terms, and a pressure Poisson equation is solved at every corrector step to satisfy the divergence free condition of the velocity. The obtained pressure field is then used to correct the velocities that were computed in the predictor step. The time advancement is carried out using explicit 3^{rd} order accurate difference formulae described in Shetty et al. [17]. The pressure Poisson equation was solved using MUDPACK libraries in the original single block version of the code. However, in the present code multiblock version of the WenoHemo code, this has been replaced with the *hypre* [18], which solves the elliptic equations on a distributed memory machine employing MPI libraries, and a variety of fast iterative solvers.

2.3 Sub-grid Scale Modeling

The SGS stress tensor shown above in equation 2.3, needs to be modeled to close the filtered Navier-Stokes equations 2.1. The classical eddy-viscosity model which employs Bosinessque approximation relates the SGS stress tensor (τ_{ij}) to the filtered strain rate tensor as follows,

$$\tau_{ij} = -2\nu_t \overline{S_{ij}}, \tag{2.5}$$

where ν_t is the turbulent eddy viscosity, in the present case also known as the SGS eddy viscosity and $\overline{S_{ij}} = \frac{1}{2}(\frac{\partial \overline{u_i}}{\partial x_j} + \frac{\partial \overline{u_j}}{\partial x_i})$ is the filtered strain rate tensor. Next, we need

to determine the value of the SGS eddy viscosity (ν_t), and how this is determined defines different types of eddy viscosity based models. The first and simplest model that was used in LES studies is the classical Smagorinsky model [19], in which the eddy viscosity is computed as follows,

$$\nu_t = -2(C_s\Delta)^2|\overline{\mathbf{S}}|, \tag{2.6}$$

where C_s is the Smagorinsky model coefficient, Δ is the width of the LES filter, and $\overline{\mathbf{S}} = \sqrt{2\overline{S_{mn}}\ \overline{S_{mn}}}$ represents the modulus of the filtered strain-rate tensor. The model coefficient C_s is not a universal constant rather it varies depending on the flow. Smagorinsky model cannot be used to model transitional flows as it provides non-zero SGS viscosity in laminar or resolved flow regions, and it cannot handle back-scatter of energy from the subgrid scales to the filtered scales. Because of these limitations, in the present study we use another eddy viscosity model developed by Vreman [20] and referred here as Vreman model. This model is also a global coefficient eddy viscosity model, but it is applicable to fully inhomogeneous flows [14, 20]. The eddy viscosity in this model is computed as follows

$$\nu_t = C\Pi^g, \tag{2.7}$$

where

$$\Pi^g = \sqrt{\frac{B_\beta}{\alpha_{ij}\alpha_{ij}}}, \tag{2.8}$$

$$\alpha_{ij} = \frac{\partial \overline{u}_j}{\partial x_i}, \tag{2.9}$$

$$\beta_{ij} = \Delta_m^2 \alpha_{mi}\alpha_{mj}, \tag{2.10}$$

$$B_\beta = \beta_{11}\beta_{22} - \beta_{12}^2 + \beta_{11}\beta_{33} - \beta_{13}^2 + \beta_{22}\beta_{33} - \beta_{23}^2. \tag{2.11}$$

In the present study, the global coefficient of the Vreman model, C, is taken equal to 0.07. Further details and validation of the model can be found in the original article by Vreman [20].

2.4 Spatial Discretization

The domain of interest is discretized using a staggered grid, which stores the values of pressure at the vertices and each of the velocity components at mid points between the vertices. According to the present staggered scheme the u, v and w velocity components are stored at mid points between the vertices in the x, y and z directions respectively. This staggering scheme is different from those typically used in finite volume discretizations. In a finite volume discretization, say in a two dimensional grid, usually u velocity is stored at the mid point between the vertices in y direction and v velocity is stored at the mid point between vertices in the x direction. Using the same approach followed in Shetty et al. [14] and Zhang et al. [21] the convective acceleration terms in the filtered momentum equations are discretized using a fifth-order WENO scheme [15]. Like any other upwind scheme the direction of the upwind is determined based on the component of velocity that is premultiplying the convective derivative term for which WENO discretization is employed. For the sake of completeness, the working details of the WENO scheme discretization are provided here, however, full details of the derivation of this scheme can be found in the original articles [15,21]. Any variable f under consideration can be reconstructed as follows,

$$\hat{f}_{i+1/2} = \sum_{k=1}^{3} \omega_k \overline{f}^k_{i+1/2} \tag{2.12}$$

$$\omega_k = \hat{\omega_k} / \sum_{l=1}^{3} \hat{\omega_l} \tag{2.13}$$

$$\hat{\omega_l} = \gamma_l / (\epsilon + \beta_l)^2. \tag{2.14}$$

If $u_{i+1/2} \geq 0$ then $\gamma_1 = 0.3$, $\gamma_2 = 0.6$, $\gamma_3 = 0.1$ and $\hat{f}^k$ is calculated as follows,

$$\overline{f}^1_{i+1/2} = \frac{1}{3} f_i + \frac{5}{6} f_{i+1} - \frac{1}{6} f_{i+2} \tag{2.15}$$

$$\overline{f}^2_{i+1/2} = -\frac{1}{6} f_{i-1} + \frac{5}{6} f_i + \frac{1}{3} f_{i+1} \tag{2.16}$$

$$\overline{f}^3_{i+1/2} = \frac{1}{3} f_{i-2} + \frac{7}{6} f_{i-1} + \frac{11}{6} f_i \tag{2.17}$$

and β_l is calculated as,

$$\beta_1 = \frac{13}{12}(f_i - 2f_{i+1} + f_{i+2})^2 + \frac{1}{4}(3f_i - 4f_{i+1} + f_{i+2})^2 \tag{2.18}$$

$$\beta_2 = \frac{13}{12}(f_{i-1} - 2f_i + f_{i+1})^2 + \frac{1}{4}(f_{i-1} - f_{i+1})^2 \tag{2.19}$$

$$\beta_3 = \frac{13}{12}(f_{i-2} - 2f_{i-1} + f_i)^2 + \frac{1}{4}(f_{i-2} - 4f_{i-1} + 3f_i)^2 \tag{2.20}$$

if $u_{i+1/2} < 0$ then the values of $\gamma_1 = 0.1$, $\gamma_2 = 0.6$, $\gamma_3 = 0.3$ and $\hat{f}^k$ can be computed as follows,

$$\overline{f}^1_{i+1/2} = \frac{11}{6}f_{i+1} - \frac{7}{6}f_{i+2} + \frac{1}{3}f_{i+3} \tag{2.21}$$

$$\overline{f}^2_{i+1/2} = \frac{1}{3}f_i + \frac{5}{6}f_{i+1} - \frac{1}{6}f_{i+2} \tag{2.22}$$

$$\overline{f}^3_{i+1/2} = -\frac{1}{6}f_{i-1} + \frac{5}{6}f_i + \frac{1}{3}f_{i+1} \tag{2.23}$$

with the values of β_l given as follows,

$$\beta_1 = \frac{13}{12}(f_{i+1} - 2f_{i+2} + f_{i+3})^2 + \frac{1}{4}(3f_{i+1} - 4f_{i+2} + f_{i+3})^2 \tag{2.24}$$

$$\beta_2 = \frac{13}{12}(f_i - 2f_{i+1} + f_{i+2})^2 + \frac{1}{4}(f_i - f_{i+2})^2 \tag{2.25}$$

$$\beta_3 = \frac{13}{12}(f_{i-1} - 2f_i + f_{i+1})^2 + \frac{1}{4}(f_{i-1} - 4f_i + 3f_{i+1})^2. \tag{2.26}$$

Once the values of the function are reconstructed using the above formulae, the gradient of the function is then calculated from the reconstructed fluxes as,

$$\frac{\partial f}{\partial \eta} = \frac{\hat{f}_{i+1/2} - \hat{f}_{i-1/2}}{h} \tag{2.27}$$

where h denotes the distance between the adjacent vertices. The diffusion terms appearing in the filtered momentum equations are discretized using a fourth-order central difference scheme [22] as follows,

$$h^2\frac{\partial^2 f_i}{\partial \eta^2} = -\frac{1}{12}(f_{i-2} + f_{i+2}) + \frac{4}{3}(f_{i-1} + f_{i+1}) - \frac{5}{2}f_i. \tag{2.28}$$

The first-order derivatives needed in the evaluation of gradient calculations of the SGS stress tensor are also computed using a fourth-order accurate central difference scheme [22] as follows,

$$h\frac{\partial f_i}{\partial \eta} = \frac{1}{12}(f_{i-2} - f_{i+2}) + \frac{2}{3}(f_{i-1} - f_{i+1}). \tag{2.29}$$

2.5 Immersed Boundary Method

2.5.1 Motivation for the Development of a Multiblock IBM Solver

Computational fluid dynamics (CFD) simulations are becoming a reliable tool to not only understand disease progression in pathological blood vessels, but also design and gauge the performance of several medical device solutions, such as stent grafts and ventricle assist devices [23, 24]. Pathological and medical device hemodynamics often involve, transitional or mildly turbulent unsteady disturbed flows with streamline curvature and rotation [9, 10]. In order to accurately simulate such flows, a scale resolving turbulence model such as LES is required.

Turbulence modeling based on LES further requires that high order (greater than 2^{nd} order) methods be used for discretizing and solving the governing equations numerically. However, usage of high order numerical methods often limits one to use structured grids, which may not be able to handle a variety of complex geometries that arise in arterial flow domains. IBM emerged as an attractive methodology because of its ability to efficiently handle complex moving and rotating geometries on structured grids. The tedious job of mesh generation for complex flow domains is by-passed in these methods by constructing a global domain containing both the solid and fluid regions. IBM was introduced by Peskin [25], in which the flow field is solved on a Eulerian mesh and the immersed surface is discretized using Lagrangian points and the method was applied to the two-dimensional simulation of flow around a natural Mitral valve. IBM simulations can handle moving or deforming bodies with complex surface geometry relatively easily without the need for re-meshing at every time step of the flow simulation as is needed in conventional body-fitted mesh simulations. There have been many works by several authors, in applying IBM to various fluid mechanics problems such as dragonfly flight aerodynamics [26], fish swimming [26,27], human walking as an application of multiple moving immersed objects [28], blood flow in heart [29], fluid-structure interaction of aortic heart valve [30] and turbo machinery [31], to name a few. Certainly, the application list mentioned here is incomplete

and the reader is referred to the articles by Mittal et al. [32] and by Peskin et al. [33] to gain a complete insight. Simulations based on IBM can be readily applied to external aerodynamics problems [34, 35] where the volume of the solid region is much smaller compared to the fluid region thereby reducing the amount of unnecessary grid. Adaptive mesh refinement (AMR) was used by Vanella et al. [36] as a way of reducing the amount of unnecessary grid and also to increase the resolution only in the regions of interest. Griffith et al. [37] also employed an adaptive, second order accurate IBM to simulate blood flow in heart and great vessels. They achieved enhanced boundary layer resolution in model heart valve by using locally refined mesh methodology. Using AMR one can specifically refine the mesh based on geometric or solution driven parameters.

Although IBM based simulations are quite successful in external aerodynamics problems [28, 32, 34, 35], their applications to internal fluid flow in complex geometries such as blood flow in arteries are scarce. Yokoi et al. [38] used a Cartesian grid approach together with IBM and simulated blood flow in a cerebral artery with multiple aneurysms. They used a 0.6 million Cartesian grid to immerse the cerebral artery. Although, no mention of the percentage of total grid nodes in the fluid region is made in their article, given the ratio of the diameter of the cerebral artery to its lateral extents it is apparent that a large portion of grid nodes were in the exterior of the fluid domain. Delorme et al. [24] performed LES studies of powered Fontan hemodynamics with relatively short vena cavae and long pulmonary arteries in order to reduce the amount of grid nodes lying in the exterior of the fluid domain. However, again given the longitudinal and lateral extents of the total cavopulmonary connection (TCPC) compared to its internal diameter a significant number of grid nodes were located outside of the fluid domain, as was reported in their article. These are few examples of the short comings of IBM directly applied to simulate complex arterial networks. Recently, in an effort to extend IBM to simulate complex arterial geometries, de Zélicourt et al. [39] developed a serial flow solver, using an unstructured Cartesian grid approach and studied blood flow in a real-life TCPC anatomy. As de Zélicourt

et al. [39] point out in their article, one possible reason for the scarcity of studies on IBM applied to study blood flow in complex internal flow configurations, could be because of the prohibitive memory and computational demands on the single block grids that arise in order to handle these geometry. Another point that is of concern in handling complex geometries on structured grids is the constraint that all the inflow and outflow boundaries of the geometry have to terminate only on the boundary faces of the global bounding box that encloses both the fluid and solid regions. This requirement could be met in certain cases (as was done in Yokoi et al. [38] and Delorme et al. [24]) by properly truncating the complex geometry and in some cases it is not possible. Such alterations of the complex geometry to make it compatible for single block simulations might result in altering the results obtained compared to the unaltered geometry and sometimes the inflow boundary conditions may not even be known at the altered locations. In order to overcome the aforementioned problems and extend the applicability of IBM to simulate blood flow in complex anatomies, we propose a method based on a combination of multiblock structured grids and IBM on an inherently parallel framework. This particular methodology not only enables simulation of fluid flow in complex geometries but also reduces the amount of unnecessary grid that goes into the solid regions.

2.5.2 Review and Selection of Immersed Boundary Method

In the present section, we provide a quick review of three types of IBMs, falling into two different categories. The advantages of applying one method over the other are discussed. Also, the problems encountered and possible solutions to make the methods work better are also explained. And the motivation behind choosing the Ghost Point IBM (GP-IBM) in the present work is explained. First, we quickly review the following two types of IBM that were previously planned to be used in the current code and the issues of stability, and mass conservation are the main factors

for not considering them further, rather the GP-IBM was selected as the method of choice in the present work.

2.5.3 Reproducing Kernel Particle Method IBM (RKPM-IBM)

Pinelli et al. [35] developed this IBM for general finite-difference and finite-volume Navier-Stokes equations. The motivation behind considering this method is that it can be extended to higher order by simply changing the polynomials used in the interpolation and spreading operators. These operators are based on the Reproducing Kernel Particle Methods [40]. An important property that is satisfied by the interpolation and spreading operators developed in this method is that the integrals of the force field and its moment are conserved, independent of the grid topology. The presence of the IB is felt by the Eulerian fluid flow solver through the forcing terms that are introduced which are non-zero only surrounding the IB. The magnitude of the force field that needs to be set depends on the deviation of the predicted velocity field from the boundary value that needs to be attained on the IB, as follows,

$$\mathbf{F}^*(\mathbf{X_k}, t^n) = \frac{\mathbf{U}^\Gamma(\mathbf{X_k}, t^n) - \mathbf{U}^*(\mathbf{X_k}, t^n)}{\Delta t}, \tag{2.30}$$

where $\mathbf{F}^*$ is the vectorial force field that needs to be added to make the flow field attain a value of $\mathbf{U}^\Gamma$ from the present predicted value of $\mathbf{U}^*$. The other variables in the equation 2.30 are, $\mathbf{X_k}$ the coordinates of the Lagrangian surface mesh, t^n is the current time instant, Δt is the time step size. The target value of the velocity on the IB which is $\mathbf{U}^\Gamma$ is known, and the predicted Lagrangian velocity field ($\mathbf{U}^*$) is interpolated from the Eulerian predicted velocity field ($\mathbf{u}^*$) using the interpolation operator as follows,

$$\mathbf{U}^*(\mathbf{X_k}, t^n) = \mathcal{I}\left[\mathbf{u}^*(\mathbf{x_{i,j,k}}, \mathbf{t^n})\right], \tag{2.31}$$

where $\mathcal{I}$ is the interpolation operator that interpolates the field variable from the Eulerian mesh to the Lagrangian mesh. The computed force field on the Lagrangian

mesh has to be distributed back to the Eulerian mesh using a spreading operator as follows,

$$\mathbf{f}^*(\mathbf{x}_{i,j,k}, t^n) = \mathcal{C}\left[\mathbf{F}^*(\mathbf{X}_k, t^n)\right], \tag{2.32}$$

where $\mathcal{C}$ is the spreading operator that is used to translate the singular force field on the IB to the volume force field defined on the Eulerian mesh points $\mathbf{x}_{i,j,k}$. The interpolation $\mathcal{I}$, and spreading $\mathcal{C}$ operators are derived using the RKPM methods which satisfy the conservation of integrals of the force and its moment. A Dirac delta function was used to limit the force field to the nearby points in the discrete formulation. A rich treatment of the polynomial manipulations was presented by Pinelli et al. [35] in the article and the above operators finally involve element matrices whose elements further depend on the distance between the Eulerian and Lagrangian mesh points identified within a window of interest. To overcome the possibility of encountering a singular element matrices, small perturbations were added in deriving the metrics that make up the element matrix entries. The element matrix entries strongly depend on the distance between the Eulerian and Lagrangian mesh points and various combination of their products as shown in Pinelli et al. [35].

This method does not need to distinguish the fluid points from the solid points as the force field is spread over to all the neighboring Eulerian mesh points in the identified window for every Lagrangian mesh point. Thus the flow field computed using this method sets up an equal and opposite velocity field (virtual flow field) inside the solid region, which was referred to as a secondary flow field that is not of interest in the article [35]. For stationary IB problems, the element matrices can be precomputed and inverted and stored for each Lagrangian mesh point, so that they just have to be multiplied at every time step of the simulation which only adds to a small fraction of the computation time. In the following, we mention the points that make this method attractive

- This method does not require classification of the Eulerian mesh points into those belonging to solid and fluid regions

- Can be readily extended to higher than second order IBM, by incorporating higher order polynomials in constructing the interpolation and spreading operators, and with a higher order discrete delta function.

Although this method seems promising, there are couple of issues that needs to be addressed when applying this method to internal fluid flow problems, and we will return to this discussion in section 2.5.5

2.5.4 Physical Virtual Model IBM (PVM-IBM)

The PVM-IBM method was proposed by Silva et al. [41]. This method also belongs to the same category as that of the RKPM-IBM in a sense that it sets up an opposing virtual flow field inside the solid region. The main difference comes in the calculation of the forcing function that is computed to drive the fluid to the boundary velocity on the IB. In the present method the force field is computed as that equal to all the terms in the Navier-Stokes equations unlike just the local acceleration term as was done in RKPM-IBM above. Hence, the expression for the force field on the Lagrangian mesh points is given as follows,

$$\mathbf{F}^*(\mathbf{X_k}, t^n) = \frac{\partial \mathbf{U}^*(\mathbf{X}_k)}{\partial t} + (\mathbf{U}^*.\nabla)\mathbf{U}^*(\mathbf{X}_k) + -\nu\ \nabla^2\mathbf{U}^*(\mathbf{X}_k) + \nabla P(\mathbf{X}_k), \qquad (2.33)$$

which contains not only the components coming from local acceleration term, but also the convective acceleration, viscous forces, and the pressure forces, and this makes the method free of adjustable parameters. The first, and second order derivatives on the Lagrangian mesh shown in equation 2.33 are computed by constructing a local vector triad that points in the direction of the fluid region and by interpolating the values from the background Eulerian mesh. Simple linear interpolation was used in the article [41].

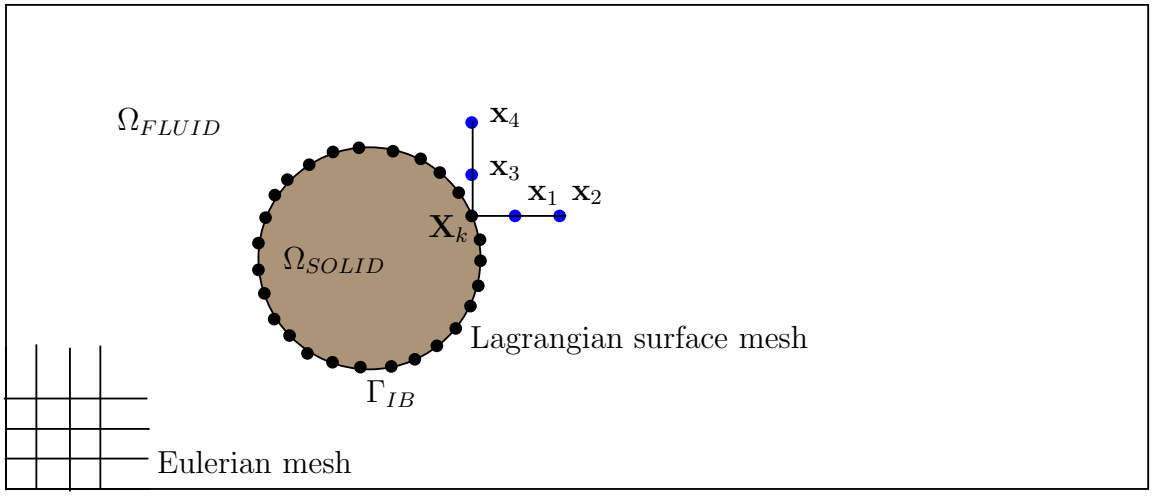

Figure 2.1. Schematic showing the local vector triad constructed on the Lagrangian point to evaluate various terms shown in equation 2.33.

Table 2.1. Ratio of volumes of the solid region to the total region in the test cases considered in the RKPM-IBM article by Pinelli et al. [35].

Test Case	Total volume	Volume of solid	Volume ratio
Fluid flow over a	$\Omega = \Omega_{FLUID} + \Omega_{SOLID}$	Ω_{SOLID}	Ω_{SOLID}/Ω
Circular cylinder	$49 \times 34 = 166$	0.7854	$4.7e-04$
Hill	$35 \times 1 = 35$	0.075	$2.1e-04$
Sphere	$14 \times 8 \times 8 = 896$	0.5236	$3.4e-03$
Normal flat plate	$12 \times 9 = 108$	0.0	0.0

2.5.5 Issues with RKPM-IBM, and PVM-IBM

The IBM methods that were discussed previously, namely, RKPM-IBM and PVM-IBM are readily applicable to external aerodynamics problems. But a few issues show up when they are applied to solve internal fluid flow. Unfortunately, all the test cases that were considered in the article by Pinelli et al. [35] are external flow problems. The volume ratio of the solid region to the fluid region for all the cases solved in the article [35] is shown in the Table 2.1. As we can see from Table 2.1, the volume ratio (Ω_{SOLID}/Ω) is very small and it is less than or equal to $\mathcal{O}(10^{-3})$. Not only the wastage of grid points (those grid points lying in Ω_{SOLID}) is less in these cases but also, the issue of satisfying mass-conservation does not surface. In both the IBMs (RKPM and PVM), the pressure Poisson equation that arises in the corrector step of the fractional time-stepping algorithm gets affected by this volume ratio in the following way. The following pressure Poisson equation is solved every time-step of the simulation on the entire domain:

$$\nabla^2 \overline{p}_{n+1} = \frac{\nabla . \mathbf{u}^*}{\Delta t} \quad in \quad \Omega. \tag{2.34}$$

Solving for equation 2.34 is not the same (numerically) as solving the pressure Poisson equations 2.35, 2.36 separately on each of the domains individually as follows:

$$\nabla^2\overline{\phi}_{n+1} = \frac{\nabla.\overline{\mathbf{u}}^*}{\Delta t} \quad in \quad \Omega_{FLUID} \tag{2.35}$$

$$\nabla^2\overline{\psi}_{n+1} = \frac{\nabla.\overline{\mathbf{u}}^*}{\Delta t} \quad in \quad \Omega_{SOLID}. \tag{2.36}$$

We argue that, the pressure field obtained by solving equation 2.34 is not equal to the sum of the pressure fields obtained by solving equations 2.35, and 2.36, even after providing consistent boundary conditions for both the cases, at least numerically, and this can be written as follows,

$$\overline{p} \ in \ \Omega \neq \overline{\phi} \ in \ \Omega_{FLUID} \ \cup \ \overline{\psi} \ in \ \Omega_{SOLID}. \tag{2.37}$$

From the numerical experiments, we observe that this inequality is a growing function of the volume ratio of the solid to the total region (Ω_{SOLID}/Ω). In a different way, we can interpret this as the pressure correction obtained by solving the equation on the entire domain only ensures mass conservation on the entire domain (Ω), but not individually on each of the domains. This phenomenon, unfortunately, did not surface in the external flow simulations performed by Pinelli et al. [35] as the volume ratios are quite small, which has only negligible effect on the mass conservation. Whereas, when applied to solve internal fluid flow problems this ratio is around 0.5 or more and the velocity corrections provided by solving the pressure Poisson equation do not ensure solenoidality of velocity in the fluid region alone. This motivates us to chose another IBM approach which is known as mirroring IBM or ghost point IBM (GP-IBM) which does not suffer from the mass conservation issue and is well suited for internal as well as external fluid flow computations.

2.5.6 Ghost Point Immersed Boundary Method (GP-IBM)

For the sake of completeness, here we describe the working details of GP-IBM. The GP-IBM method was proposed and tested by Mark et al. [42] for incompressible

flow simulations. The same method was also tested by Chaudhuri et al. [43] for compressible flow simulations with shocks. In the IBM, a Lagrangian surface mesh of the immersed boundary is used to demarcate the solid and the fluid regions on the Eulerian mesh which happens to be the domain on which the governing equations (2.1) are solved. Identification of inside/outside of a surface is known as point in polyhedron problem in computer graphics and in the present work we make use of the algorithm described by Choi et al. [28]. A function known as level set was constructed from the algorithm described in Choi et al. [28]. Level set function (ϕ) assumes values as follows,

$$\phi = 0 \ on \ \Gamma_{IB} \tag{2.38}$$

$$\phi > 0 \ in \ \Omega_{FLUID} \tag{2.39}$$

$$\phi < 0 \ in \ \Omega_{SOLID}. \tag{2.40}$$

where Ω_{FLUID} indicates the fluid domain, Ω_{SOLID} represents the solid domain and Γ_{IB} demarcates the fluid domain from the solid domain and serves as the Lagrangian immersed boundary. To compute the level set function, each Eulerian mesh point has to be compared with the Lagrangian mesh point and this becomes a slow process as the number of Eulerian mesh points increase. In order to speed up the level set computation considerably we make use of kd-tree based searching as described in Kennel [44]. The search algorithm used in kd-data structure is a generalization of the binary search tree to higher dimensional spaces. Using kd-tree search algorithm one can locate the closest neighbor to a chosen vector only in $O(logN)$ time instead of the linear search that requires $O(N)$ time, with N being the number of degrees of freedom of the Eulerian mesh. The Fortran95 version of the open source package KDTREE2 developed by Kennel [44] is used in the present work and the same is available for download from [44]. The immersed body was meshed with triangular elements by using the commercial mesh generation package GAMBIT(developed and marketed by ANSYS Inc.). Then this surface mesh description was read by the WenoHemo

solver, to compute the level set function. As described in Chaudhuri et al. [43], a mapping function is defined based on the values of the level set function as follows,

$$\zeta_{ijk} = 0 \;\; if \phi < 0 \tag{2.41}$$

$$\zeta_{ijk} = 1 \;\; if \phi \geq 0. \tag{2.42}$$

Next step is the identification of the ghost points (GP), boundary points(BP), and image points (IP), surrounding the immersed boundary points. Both the mapping function, as well as GP, BP, IP are identified for each velocity component on the staggered grid. Let Γ be the set consisting of GP, BP, and IP. Ghost points are defined as the points in the solid region ($\Omega SOLID$ that have at least one fluid neighbor or next neighbor. This is identification to include next neighbor points is required by the WENO scheme stencil, so that at least two ghost point layers are marked inside the solid region, surrounding the IB. The ghost points are computed along all three coordinate directions, and stored in the set Γ as follows,

$$\Gamma_{gp} = (x_i, y_j, z_k) \in \Omega_{SOLID} \;\; if \;\; \exists \;\; (x_l, y_m, k_n) \in \Omega_{FLUID} \;\; for \tag{2.43}$$

$$l = i-2, ..., i+2, \tag{2.44}$$

$$m = j-2, ..., j+2, \tag{2.45}$$

$$n = k-2, ..., k+2. \tag{2.46}$$

Once the GP are marked, their corresponding BP, and IP need to be identified. The BP are located on the IB, and IP are located in the fluid region being a mirror image of the GP about the Lagrangian mesh face normal. The GPs are always located on the Eulerian mesh, but the IPs may or may not be located on the Eulerian mesh. Hence, the primitive variables at the IPs are interpolated from the neighboring bounding box that is identified. A tri-linear interpolation is performed to obtain the staggered

velocity values in each direction at the IP. The metrics that are dependent on the grid are computed once and stored as follows,

$$\alpha = \frac{(x_{i+1} - IP_x)}{(x_{i+1} - x_i)} \tag{2.47}$$

$$\beta = \frac{(y_{j+1} - IP_y)}{(y_{j+1} - y_j)} \tag{2.48}$$

$$\gamma = \frac{(z_{k+1} - IP_z)}{(z_{k+1} - z_k)}, \tag{2.49}$$

where IP_x, IP_y, IP_z are the Cartesian coordinates of the IP. The staggered velocity in the x-direction at the IP can then be assigned at every time step as follows,

$$\begin{aligned} u_{ip} \;=\; & \alpha\beta\gamma \; u_{i,j,k} \\ & +(1-\alpha)\beta\gamma \; u_{i+1,j,k} \\ & +\alpha(1-\beta)\gamma \; u_{i,j+1,k} \\ & +\alpha\beta(1-\gamma) \; u_{i,j,k+1} \\ & +(1-\alpha)(1-\beta)\gamma \; u_{i+1,j+1,k} \\ & +(1-\alpha)\beta(1-\gamma) \; u_{i+1,j,k+1} \\ & +\alpha(1-\beta)(1-\gamma) \; u_{i,j+1,k+1} \\ & +(1-\alpha)(1-\beta)(1-\gamma) \; u_{i+1,j+1,k+1}. \end{aligned} \tag{2.50}$$

Staggered velocity values at each GP are then assigned before calling the predictor step, as follows,

$$\overline{u}_{gp} = 2\,\overline{u}_{bp} - \overline{u}_{ip}, \tag{2.51}$$

where u_{bp} is the target value of velocity on the IB, and u_{ip} was computed in equation 2.50. After the predictor step the velocities predicted in the solid region are nullified before feeding the velocity field to the pressure Poisson solver as described in Mark et al. [42], so as to maintain mass conservation, and homogeneous Neumann pressure boundary condition across the IB. GP-IBM is very robust when compared with the other two IBM methods discussed above in a sense that the coupling of the Lagrangian mesh and the Eulerian meshes is eliminated once the ghost points are identified. This makes GP-IBM suitable candidate for high Re simulations.

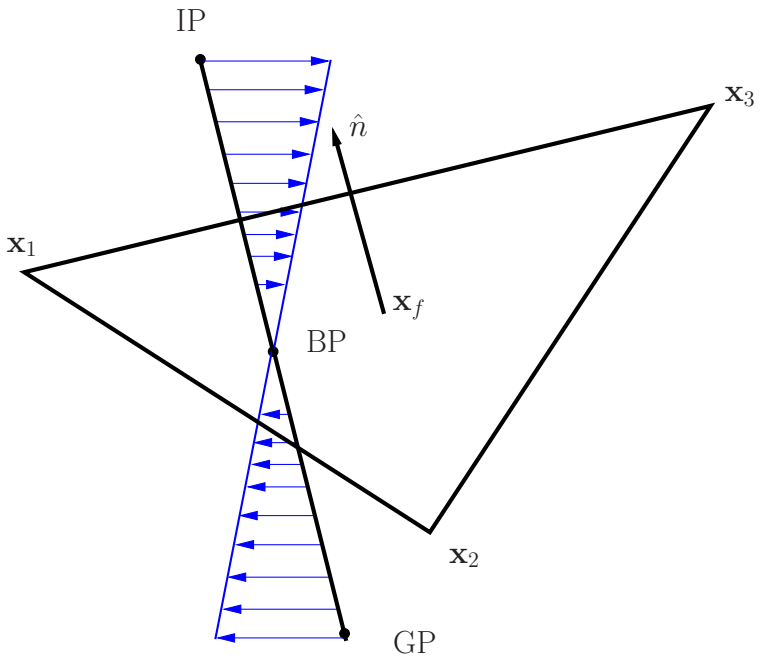

Figure 2.2. Schematic of the ghost point immersed boundary method; $\mathbf{x_1}, \mathbf{x_2}$, and $\mathbf{x_3}$ are the coordinates of the vertices of the triangles that make up the Lagrangian surface mesh. $\mathbf{x_f}$ is the face centroid, and $\hat{n}$ is the face normal vector of the triangle, that always points in the direction of the fluid. IP, BP, and GP are respectively the image points, boundary point and the ghost point.

2.6 Multiblock Methodology

In the present work, equal blocks with uniform mesh size are utilized thus making the block interface to be conformal and no special interpolation have to be performed at the block-interfaces. These equal sized blocks are used to cover the simulation domain based on the immersed boundary geometry as the input. Special care was taken for the blocks which have inlet or outlet faces ending on them, so that they have one of the block faces to be perfectly aligned with the inlet and outlet faces of the immersed boundary. As many blocks as needed are arranged such that they entirely enclose the given immersed body. Each block is assigned to one parallel processor. In the present simulations the block sizes and positions are determined manually and fed to the code. Efforts are under progress to automate the process of block discretization for any given immersed boundary so that WenoHemo tool can be used quickly for other bio-medical flow applications. The superiority of the multiblock approach over the single block approach can be explained by referring to Figure 2.3. A schematic of TAA is shown in Figure 2.3. The *Inlet* face labeled in Figure 2.3 is where aortic valve is located through which blood is pumped by heart to the ascending aorta. The three outlets labeled as *O1, O2,* and *O3* are the brachiocephalic artery, left common carotid artery and left subclavian artery respectively that carry oxygenated blood to arms and to brain. The main outlet marked as *O4* carries blood to the abdomen. As can be seen from Figure 2.3(a), single block representation of the flow domain cannot be used to simulate this problem without altering the geometry. Since the faces *Inlet* and *O4* do not terminate at one of the faces of the bounding box, they have to be either extended or truncated in order to be able to simulate using a single block grid. The results obtained from such an altered geometry may not be a true representation of the results that would be obtained by simulating the original geometry. Hence, the solver has to be augmented such that it does not alter the geometry of the complex arteries in order to solve for the fluid flow. The multiblock approach as shown in Figure 2.3(b) can handle all the inlet and outlet faces without altering them. This

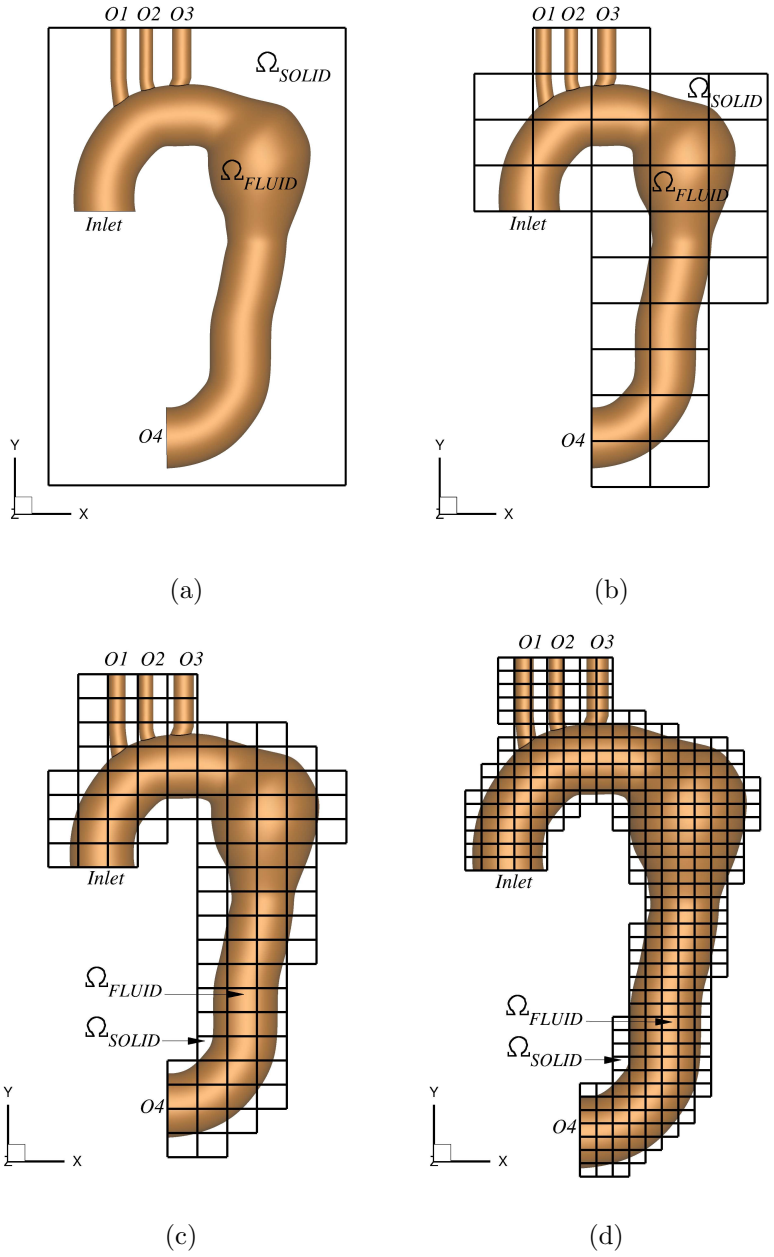

Figure 2.3. Geometry of the thoracic aortic aneurysm enclosed in a (a) single block domain (SB) (b) multiblock decomposition with 31 blocks (MB1). (c) A multiblock decomposition with 100 blocks (MB2) (d) A multiblock decomposition with 325 blocks (MB3). The surface *Inlet* indicates inflow to the domain and the surfaces $O1, O2, O3$ and $O4$ indicate the outlets to brachiocephalic artery, left common carotid artery, left subclavian artery and to abdominal aorta respectively. Ω_{FLUID} and Ω_{SOLID} represent the fluid and the solid regions respectively.

Table 2.2. Description of several block arrangements and the corresponding Volume Ratio (VR) values that maintains the same grid size in each direction by enclosing the entire fluid domain to be simulated.

Case	SB	MB1	MB2	MB3
No. of blocks	1	31	100	325
Grid points/block	$400 \times 800 \times 80$	$80 \times 80 \times 80$	$40 \times 40 \times 80$	$20 \times 20 \times 80$
Total grid points	$25,600,000$	$15,872,000$	$12,800,000$	$10,400,000$
Volume Ratio (VR)	100%	62%	50%	40%

approach reduces the amount of wasted grid points (that is those mesh points lying in the Ω_{SOLID} region). Clearly, from Figure 2.3 we can note that

$$[\Omega_{SOLID}]_{singleblock} > \sum_{k=1}^{nb} [\Omega_{SOLID}]_k \tag{2.52}$$

where nb is the number of blocks in the multiblock case shown in Figure 2.3(b). Frames (c) and (d) denote multiblock decomposition with 100 and 325 processors respectively. In addition, the multiblock approach does not alter the original geometry to be simulated, thus it makes an attractive method to simulate internal fluid flows in complex geometries. In the present work only two-dimensional block/domain decomposition is used owing to the symmetry of the problems considered about one of the axis, but the methodology presented here can be extended to three-dimensional domain decomposition without any computational difficulty.

To further establish the superiority of multiblock simulation methodology over a single block simulation we consider using several multiblock arrangements that enclose the entire fluid domain to be simulated as shown in Figure 2.3. We consider a single block case (SB) as shown in frame (a) of the figure and three multiblock cases, MB1, MB2 and MB3 which utilize respectively 31, 100 and 325 blocks to enclose the fluid domain of interest. We then compute the number of mesh points required per block in order to maintain the same grid spacing in each direction. These values are presented in Table 2.2. A metric known as Volume Ratio (VR) is defined that computes the

volume of the multiblock domain to the equivalent single block domain that would be required to simulate the same problem. VR directly relates to the savings in number of mesh points. As we can see from this table for the MB1 case we are simulating on a 62% of the mesh count, whereas for the MB2 case we are working on only 50% of the mesh size that would be needed for a single block simulation and finally for the MB3 case with 325 processors the blocks enclose the fluid domain very efficiently such that only 40% of the single block mesh resolution is sufficient to simulate the problem at the same grid spacing. Of course, in a limit the minimum VR that could be obtained would equal the ratio of volume of the fluid domain of interest to the volume of the single block domain. Hence, by efficiently arranging the blocks around the fluid domain we can achieve such a locally structured but globally unstructured mesh that simulates the problem at a reduced computational cost.

2.7 Solution of Poisson Equation

The pressure Poisson equation that results in the fractional time step method needs be to solved at every time step of the flow simulation. This equation for pressure can be derived by by forcing the velocity field at the next time level $\overline{u}_i^{n+1}$ to be divergence free [14] and can be written as follows:

$$\nabla^2 \overline{p}^{n+1} = \frac{\nabla . \overline{u}_i}{\Delta t} \tag{2.53}$$

where $\overline{u}_i$ is the predicted velocity field from the velocity field at the latest available time level $\overline{u}_i^n$, Δt is the time step size, and $\overline{p}^{n+1}$ is the pressure field to be computed such that the velocity field at the next time level $(\overline{u}_i^{(n+1)})$ is divergence free. This elliptic equation is discretized in the present work using a second order central differ-

ence operator. Using this the left hand side of the equation (2.53), leaving the over bar and the time step level for brevity, can be written as follows:

$$\nabla^2 p_{i,j,k} = \frac{\partial^2 p}{\partial x^2} + \frac{\partial^2 p}{\partial y^2} + \frac{\partial^2 p}{\partial z^2}, \tag{2.54}$$

$$\frac{\partial^2 p}{\partial x^2} = \frac{p_{i+1,j,k} - 2p_{i,j,k} + p_{i-1,j,k}}{\Delta x^2}, \tag{2.55}$$

$$\frac{\partial^2 p}{\partial y^2} = \frac{p_{i,j+1,k} - 2p_{i,j,k} + p_{i,j-1,k}}{\Delta y^2}, \tag{2.56}$$

$$\frac{\partial^2 p}{\partial z^2} = \frac{p_{i,j,k+1} - 2p_{i,j,k} + p_{i,j,k-1}}{\Delta z^2}, \tag{2.57}$$

and similarly the right hand side of the equation, for brevity leaving the over bar that denotes filtering operation, can also be written as follows:

$$\frac{\nabla . u_i}{\Delta t} = \frac{1}{\Delta t}\left(\frac{\partial u}{\partial x} + \frac{\partial v}{\partial y} + \frac{\partial w}{\partial z}\right), \tag{2.58}$$

$$\frac{\partial u}{\partial x} = \frac{u_{i+1/2,j,k} - u_{i-1/2,j,k}}{\Delta x}, \tag{2.59}$$

$$\frac{\partial v}{\partial y} = \frac{v_{i,j+1/2,k} - v_{i,j-1/2,k}}{\Delta y}, \tag{2.60}$$

$$\frac{\partial w}{\partial z} = \frac{w_{i,j,k+1/2} - w_{i,j,k-1/2}}{\Delta z} \tag{2.61}$$

where Δx, Δy and Δz are the grid sizes in x, y and z directions respectively. In the present work, we use the *hypre* [18, 45] library to solve the Poisson equation on a multiblock grid in parallel. Preconditioned conjugate gradient (PCG) method was used with geometric multigrid as the preconditioner for solving the discretized Poisson equation as described in Ashby et al. [46]. The convergence criterion was set to a relative tolerance of $1e-12$ and 3 iterations of pre- and post- sweeps are performed on each multigrid level. The Dirichlet boundary conditions on pressure were symmetrized in order to form a symmetric matrix that is required for solving the system using a conjugate gradient method. Symmetrization of a matrix at grid nodes that have a Dirichlet boundary condition can be explained as follows. Let a one-dimensional grid be represented as $i = 0, 1, ..., N-1, N$, where $i = 0$ is the left boundary and $i = N$ is the right boundary. If a Dirichlet boundary condition is applied at grid node $i = N$, then symmetrization process transfers all the entries

of the matrix at the grid node $i = N - 1$ that have coefficients associated with the known Dirichlet value at $i = N$ to the right hand side vector of the linear system.

2.8 Parallelization Strategy

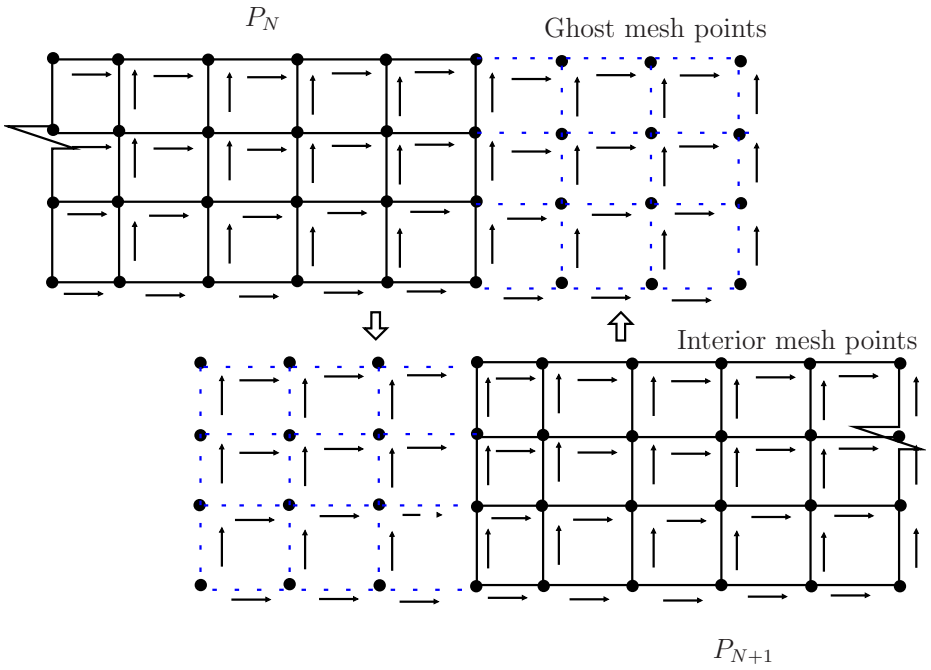

Figure 2.4. Two dimensional schematic showing the $1D$ decomposition of the domain in parallel solver. The horizontal arrows indicate the location where u velocity values are stored, vertical arrows indicate the location where v velocity values are stored and the circles indicate the location of pressure (p) points. A sample of three ghost layers of the grid is shown. Labels P_N and P_{N+1} indicate n^{th} and $(n+1)^{th}$ processors respectively in a parallel decomposition.

The WenoHemo solver is parallelized using the message passing interface (MPI). MPI allows the code to be run on a distributed memory cluster which is apt for large scale computing. A sample one-dimensional decomposition of a two-dimensional domain is shown schematically in Figure 2.4. The horizontal and vertical arrows in Figure 2.4 represent the location where u and v velocity components are stored respectively. In the figure, filled circles indicate the location where pressure is stored.

Each processor has a ghost layer of grid points, which store the values from the neighboring process. The ghost layers on each processor are shown by dotted lines in the Figure 2.4. After data exchange the ghost layers are populated with the latest values from the neighboring processor. The interior mesh points on the processor $N+1$ and the ghost mesh points on the processor N are also marked in the Figure 2.4, which corresponds to one pair of data exchange between P_N and P_{N+1} processors. In order

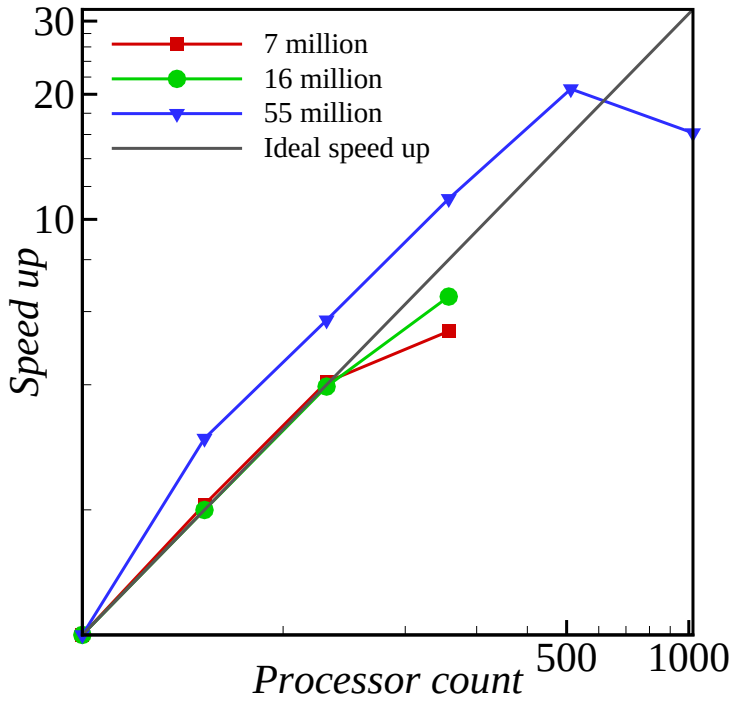

Figure 2.5. Parallel performance of the WenoHemo solver.

to evaluate the parallel performance of the solver, we select a test problem of mixing layer on a cubic domain and a sample of 100 time steps are simulated. Three different grid sizes of approximately 7, 16 and 55 million points are used for estimating the speed up of the WenoHemo solver. Processors ranging from 32 to 256 are used for testing the cases of of 7 and 16 million grid points whereas up to 1024 processors is used for testing the 55 million grid points case. The time taken by the 32 processors simulation is taken as the base line simulation to calculate the speed up. The parallel

performance of the WenoHemo solver is shown plotted in Figure 2.5. Together with the three grid sizes the figure also shows the ideal speed up curve. As we can see from this figure, linear speed up is obtained for grid sizes of 7 and 16 million grid points up to a processor count of 128, beyond which they deviate from the ideal speed up curve. At a processor count of 256 the higher grid size case of 16 million points shows better speedup than the lower grid size case of 7 million points. This behavior could be due to more computations involved per processor in the former case owing to a larger grid size. Based on the same reasoning the results obtained from the largest grid size considered could also be explained. The largest grid size case of 55 million grid points shows super linear speed up till a processor count of 512, beyond which it drops to sub linear speed up. The cluster on which these simulations were performed contains Intel Xeon x5650 CPUs with 12 cores per node and 48 GB of RAM per node. The CPUs are connected through a quad data rate (QDR) InfiniBand interconnect.

2.9 Statistical Averaging of Simulation Data

In the present study both steady and pulsatile inlet flow conditions are used, and the averaging operations used in order to gain insight into the turbulent flow quantities are described here for both the types.

In a steady inflow condition case, one can define a time-averaged mean flow quantity $\langle \overline{f}(x,y,z,t) \rangle$, for any filtered flow variable $\overline{f}(x,y,z,t)$ as follows

$$\langle \overline{f}(x,y,z,t) \rangle = \frac{1}{T_f} \int_{t_0}^{t_0+T_f} \overline{f}(x,y,z,t)\, dt \tag{2.62}$$

where, T_f is flow time over which the averaging is accomplished and t_0 is the time after the start of the simulation at which the averaging process is initiated. In a turbulent flow since the flow field is quickly changing, one can define a fluctuation of a flow variable as the its deviation from its time-averaged value as follows,

$$f'(x,y,z,t) = f(x,y,z,t) - \langle \overline{f}(x,y,z,t) \rangle \tag{2.63}$$

Further, root mean square (r.m.s) quantity of the fluctuation variable can be computed as,

$$f'_{r.m.s}(x,y,z,t) = \sqrt{\langle f'(x,y,z,t)^2 \rangle} \tag{2.64}$$

In an unsteady flow, various averaging operations can be defined and used similar to the time-averaged mean flow defined above in equation 2.62. Whereas in a pulsatile flow, which is used in the present case there is a specific periodicity of inlet flow which induces a time scale on the problem under study. Because of this periodicity of the problem, using an ensemble-average or a phase-average is more appropriate than a time average. The ensemble average or phase average operation that represents the time varying response to the pulsation can be defined over N time period cycles as follows,

$$\langle \overline{f}(x,y,z,t) \rangle_p = \frac{1}{N} \sum_{n=0}^{N-1} \overline{f}(x,y,z,t+nT) \tag{2.65}$$

To identify the fluctuation of the flow field with respect to the pulsating inlet, the fluctuation quantity is defined as follows,

$$f''(x,y,z,t) = \overline{f}(x,y,z,t) - \langle f(x,y,z,t) \rangle_p \tag{2.66}$$

The r.m.s quantity of the phase averaged fluctuation quantity is computed as follows,

$$f''_{r.m.s}(x,y,z,t) = \sqrt{\langle f''(x,y,z,t)^2 \rangle_p}. \tag{2.67}$$

Additionally, the averaging in the spanwise direction is denoted by the operator $\langle \rangle_z$.

3. VALIDATION OF WENOHEMO SOLVER

In this chapter, we first test the overall order of accuracy of the WenoHemo solver using a Taylor Green vortex problem in a periodic domain with a sphere placed at the center of the domain. Then the IBM, and the multiblock approach are the additional numerics that were added to the code over and above the basic fluid flow solver which was validated in Shetty et al. [14]. So, in order to be confident about the results that are produced with the present solver, we first validate these two new implementations one by one in the present chapter. The solver, as a whole consisting of both the methods is validated in the next chapter in the AAA simulations and comparisons are made to the experimental results. In order to validate the IBM, we chose the flow over a sphere case, and to validate the multiblock approach. Since, pulsatile simulations will be performed to study blood flow in thoracic aorta and in a model aorta fitted with a bi-leaflet mechanical heart valve, it is critical that validation of pulsatile flow be performed in order to gain confidence in the results obtained. To accomplish this, a model stenosis problem that was previously studied in the literature is simulated using the present solver and a comparison is made to the results reported in the literature. The present solver will also be applied to study cavitation potential in a mechanical heart valve in future. Motivated by this, preliminary validation studies are performed with existing cavitating and non-cavitating mixing layer experimental results available in the literature.

3.1 Test of Order of Accuracy

The spatial order of accuracy of the present LES solver without the IBM has been previously calculated and it was shown to be 5^{th} order on a periodic domain for a Taylor-Green Vortex (TGV) solution in Shetty et al. [14]. The spatial order of

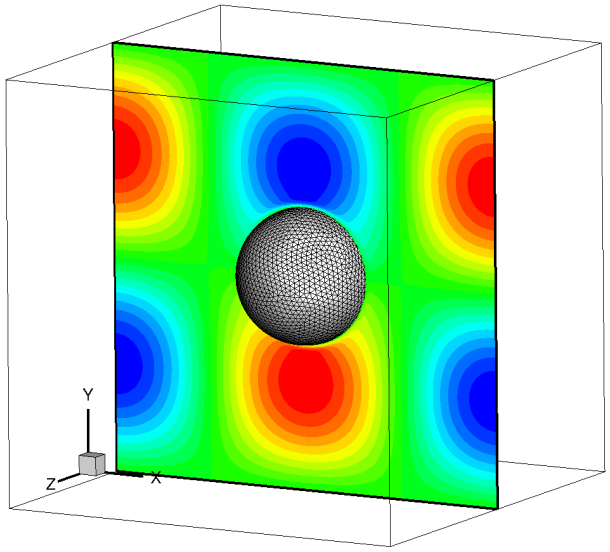

(a)

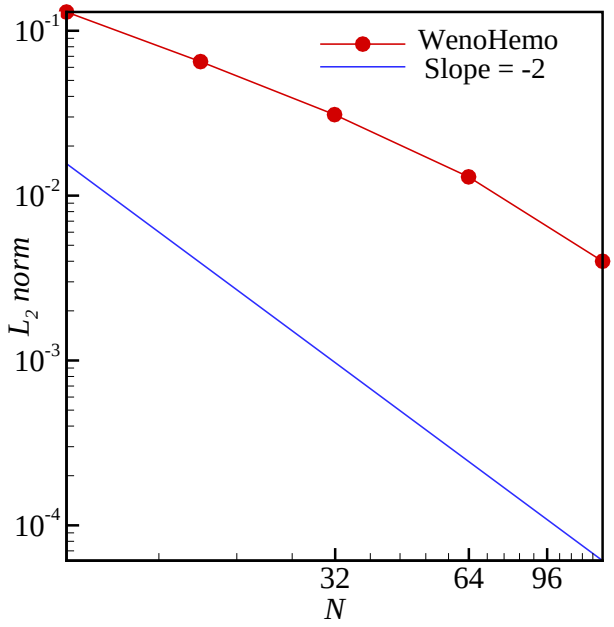

(b)

Figure 3.1. (a) Contours of u-velocity component on $z = 0$ plane for the grid size of 256^3 (b) Variation of L_2 error norm of the u-component of velocity as a function of the grid size depicting the spatial order of accuracy of the present solver.

accuracy of the IBM was also previously evaluated by Mark et al. [42] by simulating laminar flow over a sphere and by further computing it's drag coefficient. They showed that mirroring IBM method is second order accurate from these simulations. For the sake of completeness, here we perform test of spatial order of accuracy for the developed WenoHemo solver using the three-dimensional TGV that evolves from an initially two-dimensional velocity and pressure fields given by:

$$u(x, y, z, t) = -\cos(kx)\sin(ky)\exp(-2k^2t/Re), \tag{3.1}$$

$$v(x, y, z, t) = +\sin(kx)\cos(ky)\exp(-2k^2t/Re), \tag{3.2}$$

$$p(x, y, z, t) = -\frac{1}{4}(\cos(kx) + \cos(ky))\exp(-4k^2t/Re); \tag{3.3}$$

is considered. A domain of size $[-\pi, +\pi]^3$ is considered with $k = 1$, $Re = 100$ and a time step of $\Delta t = 0.001$. In order to bring in the effect of the IBM on this flow field, a stationary sphere is placed at the origin. All the simulations are run for 100 time steps at an equal time step on grids of sizes $8^3, 16^3, 32^3, 64^3, 128^3$. The result obtained on a grid size of 256^3 is considered as the base line result for calculating the error estimates. The contours of u-velocity component on the $z = 0$ plane are shown plotted in Figure 3.1(a). The L_2 norm of the error in the u-velocity component is shown plotted in Figure 3.1(b). As we can see from this figure the present solver shows second order accuracy in space owing to the inclusion of the IBM method.

3.2 Steady Inflow over a Sphere

To validate the IBM that was implemented into the code, we performed simulations of flow over a sphere at various Re numbers. We compared the results to the the experimental results of Johnson et al. [47]. The definition of various quantities such as the length of the re-circulation region, the coordinates of the center of the eddies (XC, YC) is shown in the schematic Figure 3.3. Flow over bluff bodies is of interest in many areas, to understand the wake dynamics, and the flow forces induced by them which further get transmitted to the structure they are attached to. Flow over a sphere forms a simple fluid dynamics problem in this area. Up to $Re = 300$

the flow behind a sphere exhibits attached eddies, and at $Re = 300$, the flow becomes unsteady, with periodic vortex shedding although the upstream flow is still steady.

The simulation domain used in the present study, and the triangulated surface mesh on the sphere are shown plotted in Figure 3.2. The diameter of the sphere (d) is taken as the length scale and the inlet velocity ($U = 1$) is taken as the velocity scale. The domain extends 25 in the x direction, and $8D$ in the y, and z directions. The mesh size was set as 385 grid points in the x direction, and 129 points in each of y and z directions, making a total resolution of 6.4 million points.

The length of the re-circulation region, and the eddy center are shown compared in Figure 3.4, as the Re is increased from 50 to 200 all the measured quantities increase, agreeing very well with the experimental results. The out-of-plane vorticity contours are shown plotted in Figure 3.5, which shows as the Re is increased, the effect of the wake behind the sphere increases by more and more vorticity production in the wake region. Also, in frames (b), (c), and (d) of Figure 3.5, we notice that there are small attached vorticity regions just behind the sphere in addition to the large scale vorticity regions that are observed. For all the simulations in the Re range of 50 to 200 the simulation remains steady, with attached eddies behind the sphere. As the Re is increased to a value of 300, instability sets up and the sphere starts shedding the eddies in an alternating fashion giving rise to a Von-Karman vortex street. The vortex shedding is visualized by plotting the iso-surfaces of $\lambda_2 = -0.5$ and colored by y-vorticity as shown in Figures 3.7, 3.6. As we can see from Figure 3.7, the eddies that are shed are quite symmetric in the xy plane, and they grow as they convect downstream. The positive and negative rotations of the eddies can be identified with the help of the y-vorticity color.

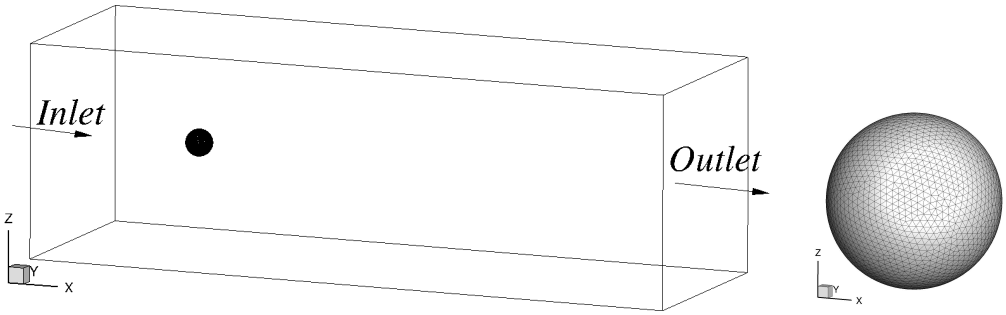

(a) Computational domain (b) Triangulated surface mesh

Figure 3.2. Schematic showing the (a) computational domain used for the simulation of flow over a sphere and the (b) Lagrangian surface mesh on the sphere.

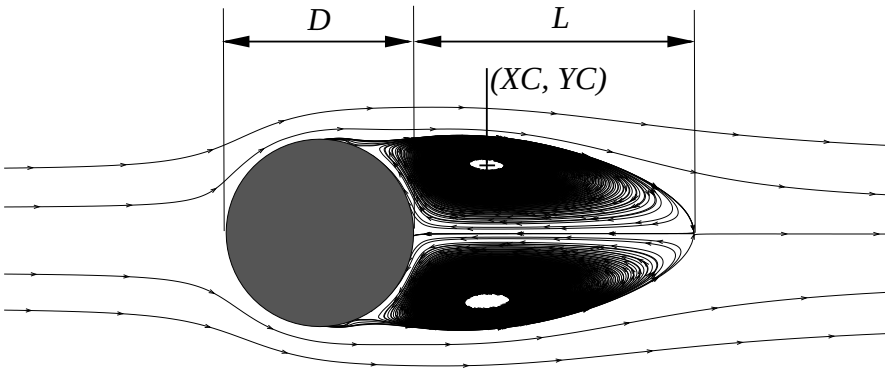

Figure 3.3. Schematic showing the definition of the center of the bubble (XC, YC), with the center of the sphere at the origin $(0, 0)$, and the length of the separation bubble (L).

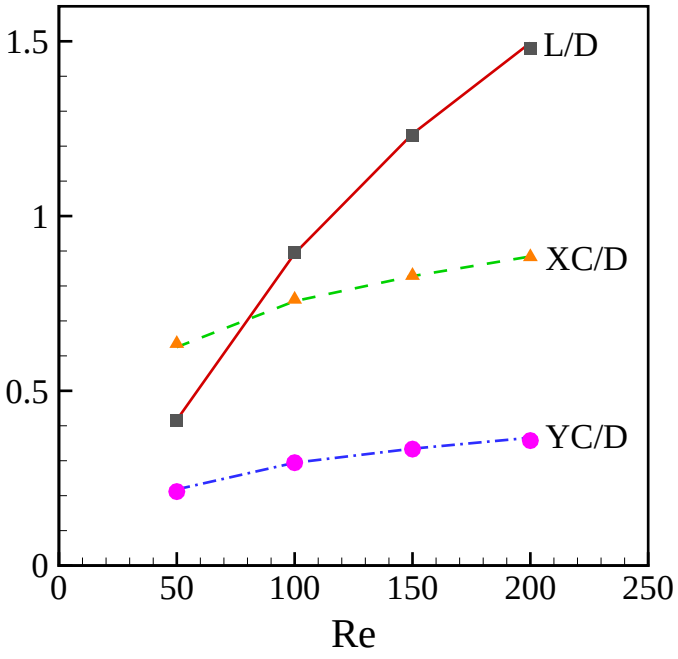

Figure 3.4. Comparison of the separation bubble parameters to experimental results of Johnson et al. [47]; lines denote the present computations with WenoHemo solver, symbols denote the simulation results obtained by Johnson et al. [47].

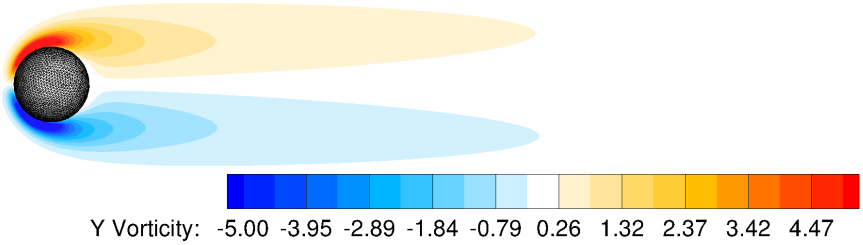

(a) $Re = 50$

(b) $Re = 100$

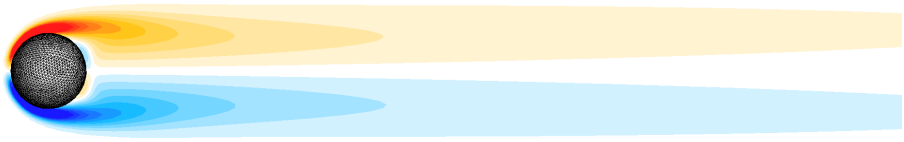

(c) $Re = 150$

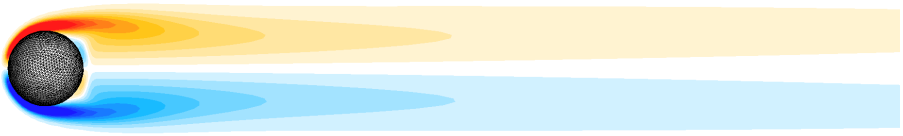

(d) $Re = 200$

Figure 3.5. Contours of out-of-plane vorticity for indicated Re; 20 equidistant contours ranging between -5 (blue) to $+5$ (red) are shown.

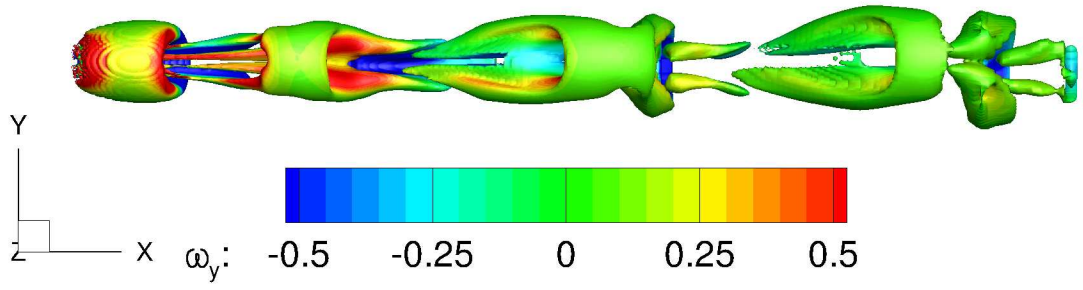

Figure 3.6. Vortex shedding behind the sphere at a $Re = 300$, colors indicate the y-component of vorticity; 20 equally spaced contours between $-1/2$ (blue) and $1/2$ (red) are shown.

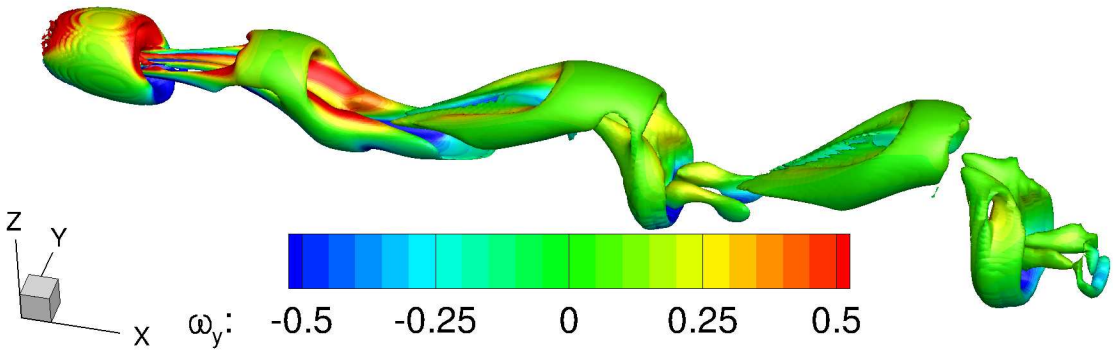

Figure 3.7. Iso-metric view, see Figure 3.6 for caption.

3.3 Steady Inflow over a Backward Facing Step

In order to validate the multiblock solver as it is with out the immersed boundary method, we performed simulations of flow over a backward facing step and compared the results to those obtained by the experiments conducted by Tylli et al. [48].

Flow over backward facing step is a standard benchmark problem for numerical methods. The geometry considered here is same as that of the one used by Tylli et al. [48] in their experiments, and the schematic together with the multiblock decomposition into 35 equal sized blocks is shown in Figure 3.8. The backward facing step considered here has an expansion ratio of 2 and a downstream aspect ratio of 20. The inlet channel height was chosen as the length scale and a curve fit for the laminar flow in a plane channel was used as the velocity profile at the inlet. The domain extents in the non-dimensional units are -1 to 34 in the x-direction, -0.5 to $+0.5$ in the y-direction in the step region, and -1.5 to $+0.5$ in the y-direction in the channel region, and -20 to $+20$ in the z-direction. Dirichlet velocity boundary condition was used on the inlet with a parabolic velocity profile given by,

$$u = \left[1 - exp\left(\frac{-z-20}{0.35}\right)\right] \times \left[1 - exp\left(\frac{z-20}{0.35}\right)\right] \times [1 - 4y^2]. \tag{3.4}$$

No-slip, impermeable wall boundary condition was used on the walls in the y and z-direction. Outflow boundary condition employing homogeneous Neumann boundary condition on all components of the velocity is used at the outlet of the domain. The simulation used $29, 29$ and 241 mesh points in x, y, and z direction respectively in each block, giving a total of about 7.1 million mesh points. Two simulations were considered here to compare the results with the experiments and they have $Re = 300$ and 648. Both the cases showed steady flow in the experiments [48] and hence they can be compared to steady flow simulation results as was done here. In fact, from the experiments [48], the flow was noted to be steady, for Re up to approximately 700. The first case with $Re = 300$ is a low Re case, and only $2D$ simulation could have been employed as the side wall effects does not effect the flow on the central plane

($z = 0$). But we resort to $3D$ simulations in both the Re cases. In the $Re = 648$ case, three-dimensional effects are noted and hence the results obtained from a two-dimensional simulation would not match those obtained with the three-dimensional experiments or simulation results.

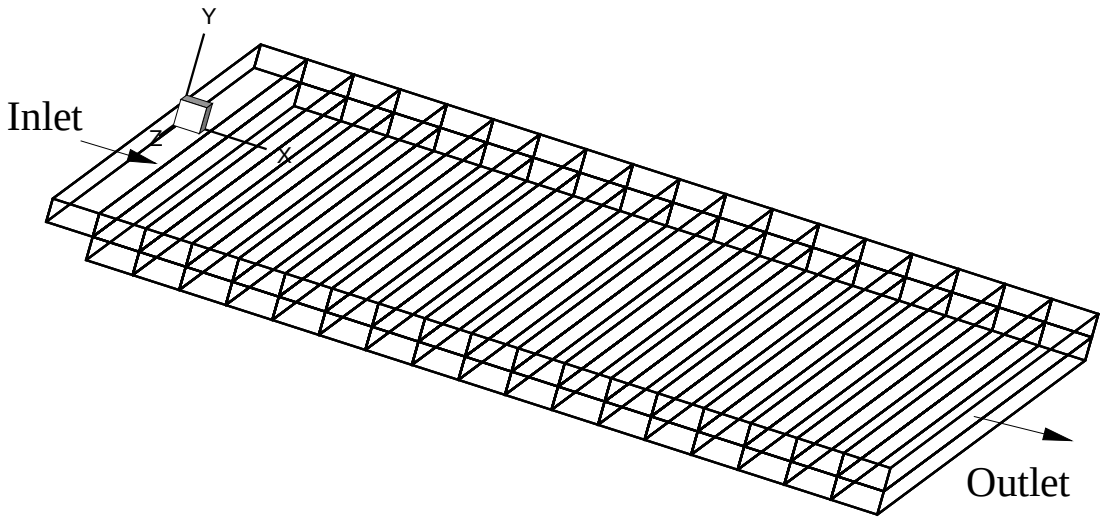

Figure 3.8. Schematic of the backward facing step geometry used in the present calculations. The decomposition of the domain into 35 equal sized blocks to create the step and and outlet geometry is also depicted.

Re = 300

Here, we compare the axial velocity profiles sampled at various x locations along the length of the channel as a function of the y coordinate. The comparison is shown in Figure 3.9. As we can see from Figure 3.9, the computed solution matches very well with the experimental data until $0 \leq x \leq 4$ and after $8 \leq x \leq 16$. At locations $x = 5$ and $x = 6$, the match is not exact but the lower region ($-1.5 \leq y \leq -0.5$) seems to be matching better when compared to values in the upper region ($-0.5 \leq y \leq +0.5$).

The contours of velocity magnitude on the central plane ($z = 0$) are shown plotted in Figure 3.10. The re-circulation zone, forming immediately after the step and above the bottom wall, can be seen in the Figure 3.10. This primary re-circulation zone is a manifestation of the *coanda effect* [49, 50]. In addition to this primary re-circulation zone, a secondary re-circulation zone can be seen on attached to the top wall. Streamlines shown plotted in Figure 3.11 depict the direction of rotation of the fluid in both the re-circulation regions. In the primary re-circulation zone, the fluid moves in clockwise direction, whereas in the secondary re-circulation region, fluid moves in counter-clockwise direction. The contours of out-of-plane (z) vorticity shown overlapped on the streamlines in Figure 3.11 explain the direction of rotation of the fluid in these re-circulation regions.

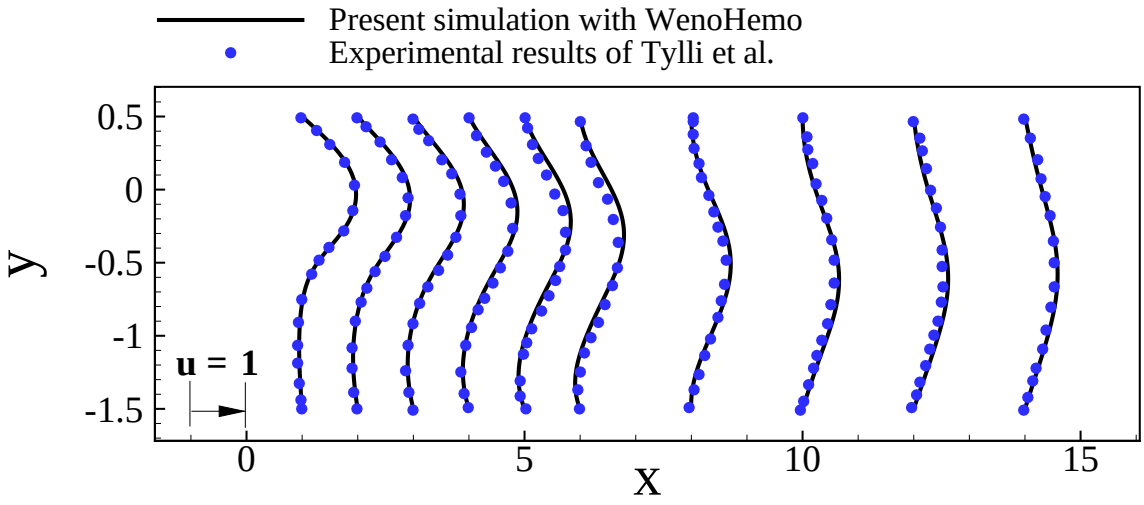

Figure 3.9. $Re = 300$: u-velocity profiles vs y coordinate, at a number of stream-wise cross sections, for $z = 0$ plane, for experiment and simulation.

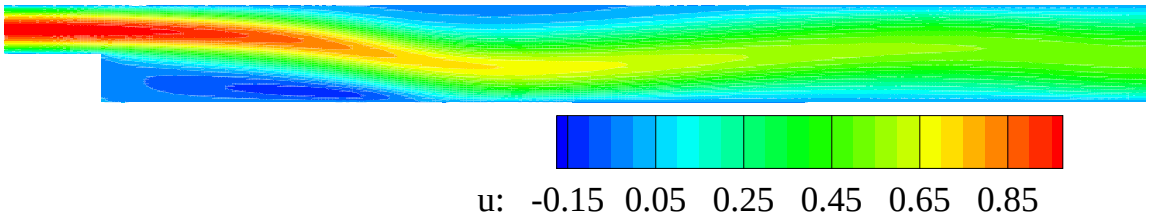

Figure 3.10. Contours of u-velocity on $z = 0$ plane at a Reynolds number of 300.

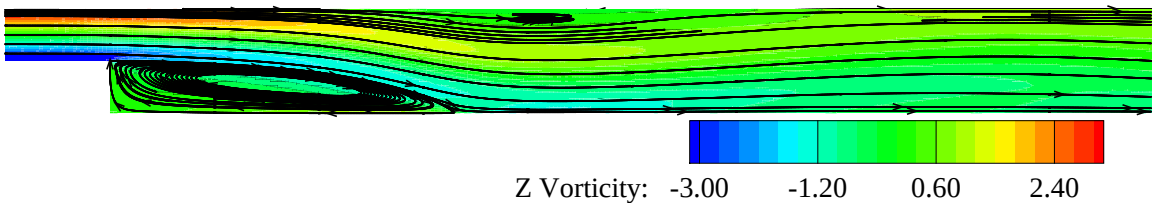

Figure 3.11. Contours of out-of-plane vorticity together with the streamlines on $z = 0$ plane at a Reynolds number of 300.

Re = 648

When we increase the Re from 300 to 648, the flow is still steady and laminar but three-dimensional effects get introduced into the problem. First, we compute the u-velocity profiles as a function of the channel height (y) at various stream-wise cross sections. Figure 3.12, shows the comparison between present simulations and experimentally measured values of Tylli et al. [48] on the central ($z = 0$) plane. From Figure 3.12, we see that the results match very well in the range $0 < x < 12$, but slight deviations are observed towards the outlet of the domain the range $12 < x < 20$, both in the lower and upper regions of the channel height. Similar behavior in the match is observed on the plane $z = 10$, as shown in Figure 3.13, which is located half way between the channel side wall and the center of the channel. Another comparison in results is made on the plane $z = 18$ which is very close the side wall of the channel. The comparison is shown plotted in Figure 3.14. Despite the proximity of the plane to the side wall a very good agreement in results is obtained in the range $0 < x < 8$ and the match is relatively not good in the range $8 < x < 20$. But unlike the previous z planes that were plotted the results deviate from the experiments in the lower part of the channel height when considering the range $8 < x < 20$. The contours of u-velocity profiles are shown plotted in Figure 3.15, from which we can visually notice a longer primary and secondary re-circulation zones compared to the $Re = 300$ case shown in Figure 3.10. Having compared the u-velocity profiles, we turn our attention to look at the three-dimensional effects of the backward facing step problem. In Figures 3.16(a)-(c), the w-velocity profiles are shown plotted on the yz-plane at three x locations ($x = 4, 8, 12$). As was observed in the previous studies [48], we see the presence of a wall-jet close to the lower wall of the channel that is directed towards the mid-plane of the channel. Only half of z planes are shown plotted in Figure 3.16(a)-(c), owing to the symmetry of the wall jet about the mid-plane. In order to further understand the wall jet formation, a number of w-velocity profiles are extracted and plotted a function of y on the yz-plane at the indicated x locations in the left column

of the Figure 3.17 (frames (a),(c), and (e)). An interesting observation noted by Tylli et al. [48], is that, as the wall-jet develops along the span wise direction, the w-velocity profiles become self similar. The self similar velocity profiles are shown plotted in the right column of the Figure 3.17 (frames (b), (d) and (f)). The w-velocity components were normalized by the maximum w velocity of the profile (w_{max}) and the channel height was normalized using the half width (y_{half}, which equals the distance from the wall where the w velocity becomes half of the w_{max} velocity on the decreasing part of the profile). The y_{wall} used in the normalization equals -0.15 in the present case. As we can see from the right column of the Figure 3.17 the velocity profiles overlap in accordance with the self similar nature. However, on the $x = 12$ plane there seems to be a reverse flow in the jet close to the wall which do not overlap. This discrepancy needs to be further analyzed as to whether it is related to the mesh resolution of the simulation.

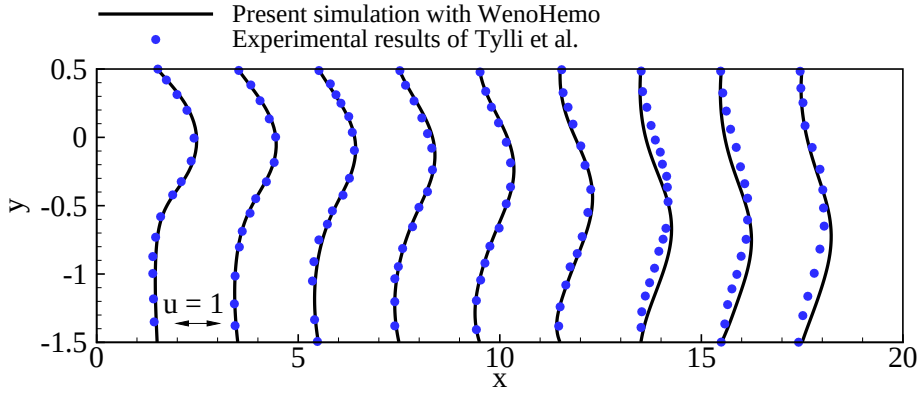

Figure 3.12. $Re = 648$: u-velocity profiles vs y coordinate, at a number of stream-wise cross sections, for $z = 0$ plane, for experiment and simulation. The x and y scales are not the same and the u scale is same as shown in Figure 3.9.

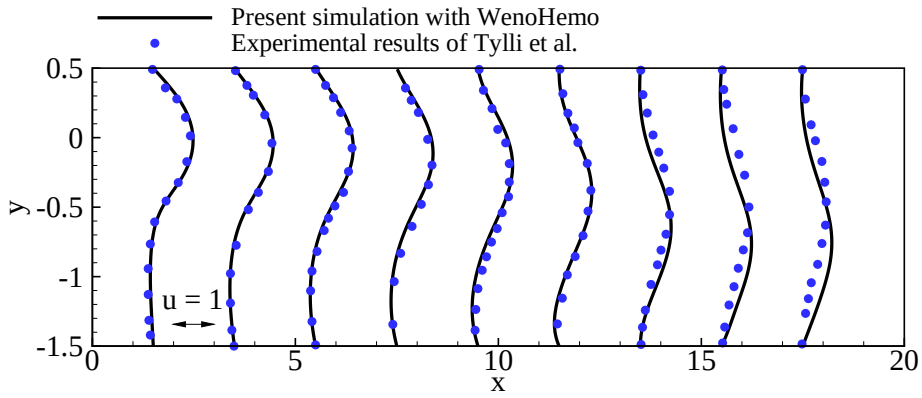

Figure 3.13. $Re = 648$: u-velocity profiles vs y coordinate, at a number of stream-wise cross sections, for $z = 10$ plane, for experiment and simulation. The x and y scales are not the same and the u scale is same as shown in Figure 3.9.

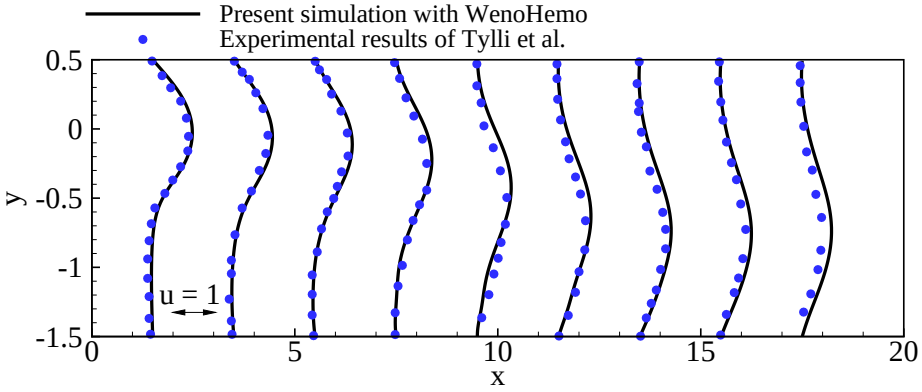

Figure 3.14. $Re = 648$: u-velocity profiles vs y coordinate, at a number of stream-wise cross sections, for $z = 18$ plane, for experiment and simulation. The x and y scales are not the same and the u scale is same as shown in Figure 3.9.

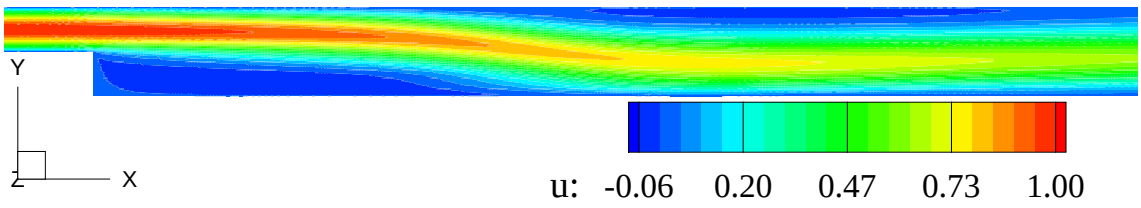

Figure 3.15. Contours of u-velocity on $z = 0$ plane at a Reynolds number of 648.

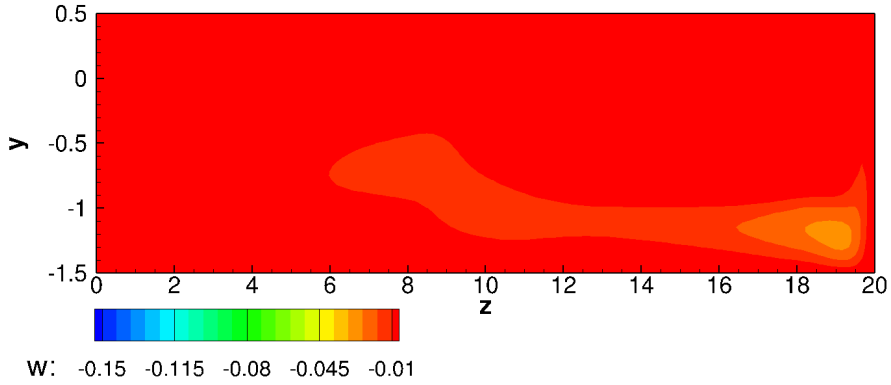

(a) $x = 4$

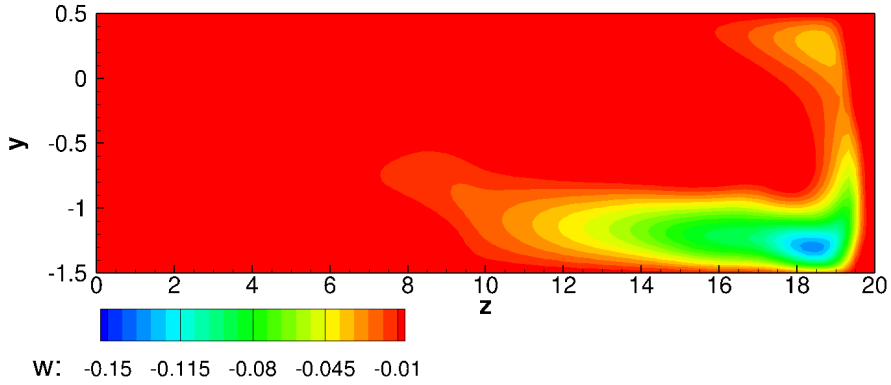

(b) $x = 8$

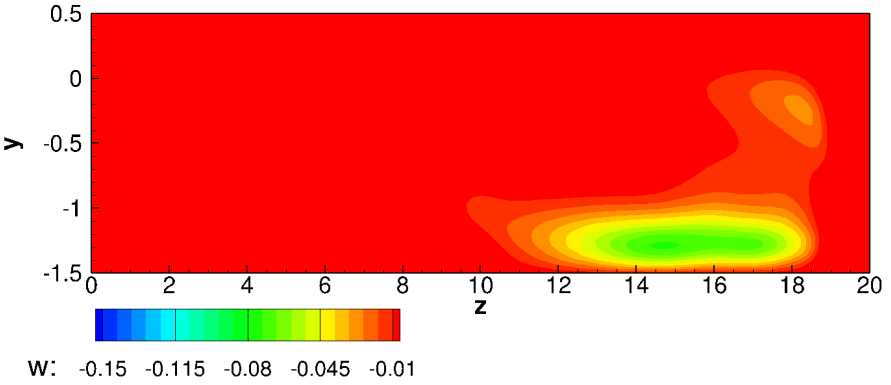

(c) $x = 12$

Figure 3.16. $Re = 648$: contours of w velocity for a number of yz-planes at indicated x locations. The y and z scales are not the same.

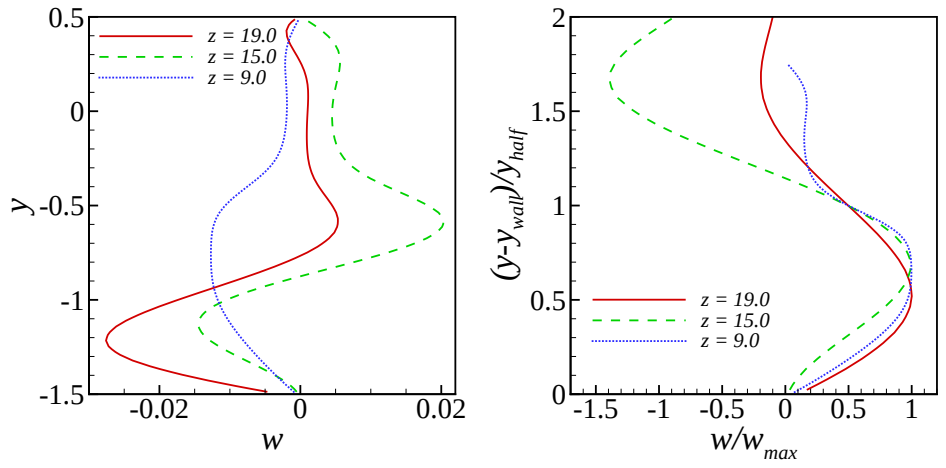

(a) $x = 4$ (b) $x = 4$

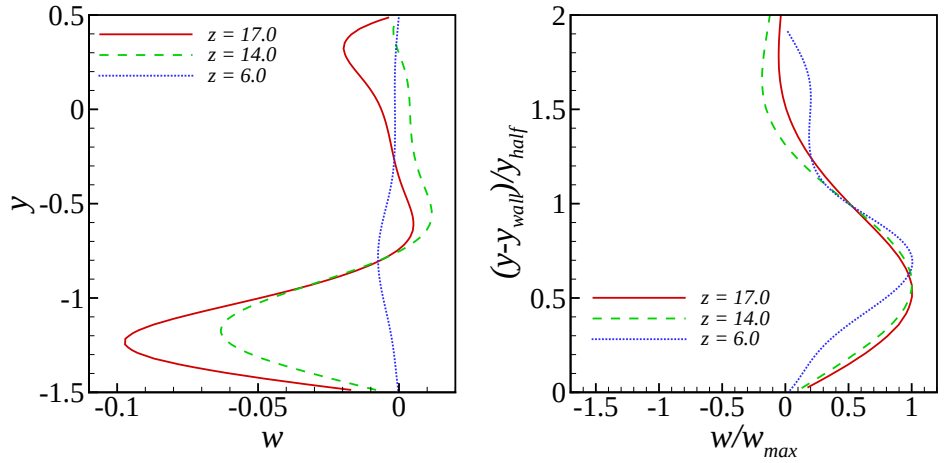

(c) $x = 8$ (d) $x = 8$

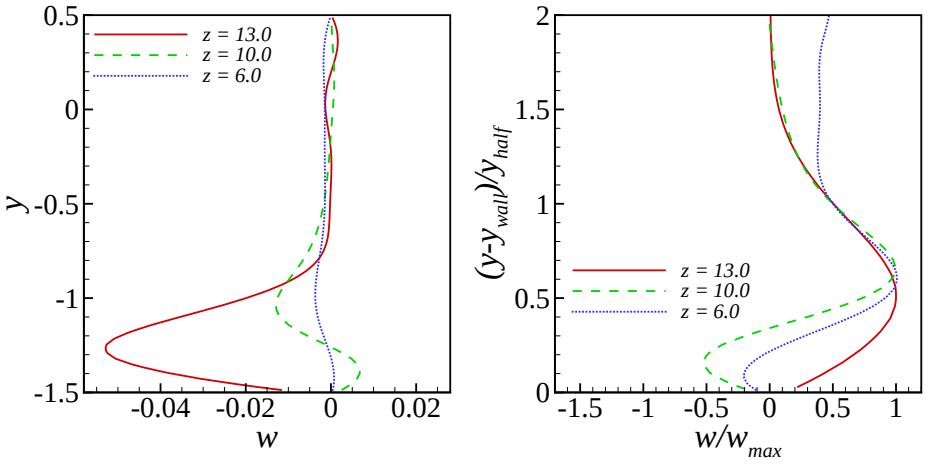

(e) $x = 12$ (f) $x = 12$

Figure 3.17. $Re = 648$: w-velocity profiles: original (left column) and normalized (right column); plotted as a function of y-coordinate at indicated z locations, and x planes.

3.4 LES of Pulsatile Inflow in a Model Stenosed Channel

All the previous cases are validated only for steady inflow conditions . As the focus of the present work is pulsatile flow it is critical that a comparison of the results obtained from WenoHemo solver be made to the existing results in the literature. In order to this, we choose the model stenosis problem first studied by Mittal et al. [51] and recently used as validation problem in Molla et al. [52]. This model stenosis problem serves as a good candidate for validation owing to its simple geometrical configuration and a sinusoidal pulsating inlet velocity profile. The geometry of the model stenosis problem consists of a channel with a height $h = 1$ extending -5 to 15 in the x direction, with a semi circular constriction at $x = 0$ location. The domain extends -2 to $+2$ in the span wise or z direction. At the inlet to the domain a time varying parabolic inflow profile $u(y,t) = 2U_{max}(y/h)(1 - y/h) + (U_{max}/4)(1 - cos(2\pi t/T))$ is imposed. At the outlet of the domain simple homogeneous Neumann boundary condition on velocity is applied. A no-slip boundary condition is applied on the lower and upper walls. A free slip boundary condition on velocities is applied on the front and back planes in the z direction. The Reynolds number for the present validation study is defined as $Re = U_{max}h/\nu$ based on the maximum velocity U_{max} as the velocity scale and the height of the channel h as the length scale. Consistent with the previous works [51, 52] the simulation was conducted for $Re = 2000$ to be able to make comparisons. The grid system used consisted of $15 \times 30 \times 64$ per block and with $40 \times 3 \times 1$ block in each of the x, y and z directions respectively, making a total grid points of $600 \times 90 \times 64$. The grid resolution used are higher than those used in the previous studies [51, 52], this is justified because the present simulations are based on an IBM solver, whereas the previous studies used a body fitted mesh. A bulk velocity scale $\overline{U}$ is used instead of the maximum velocity U_{max} to perform post processing of the data similar to the previous studies [51, 52].

A comparison of normalized time averaged axial velocity profiles from the present simulations obtained using Vreman SGS stress model, and the results obtained by

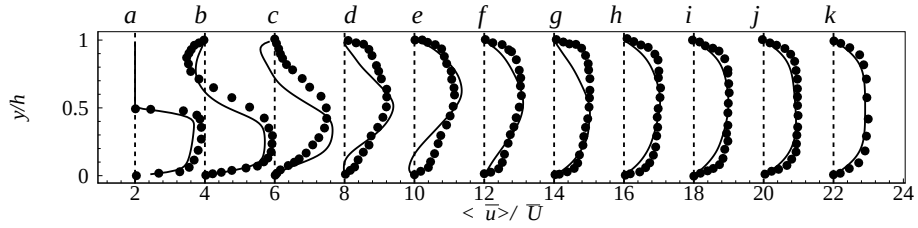

Figure 3.18. Comparison of normalized time averaged axial velocity profiles between the present results (lines) and the simulation results of Molla et al. [52] (solid dots) at several locations (a) $x/h = 0$ (b) $x/h = 1$ (c) $x/h = 2$ (d) $x/h = 3$ (e) $x/h = 4$ (f) $x/h = 5$ (g) $x/h = 6$ (h) $x/h = 8$ (i) $x/h = 10$ (j) $x/h = 12$ (k) $x/h = 15$. The dashed lines at each location indicate local zero value for axial velocity.

Molla et al. [52] using dynamic SGS stress model are shown plotted in Fig. 3.18 at indicated locations along the axis of the channel. As can be seen from this figure the axial velocity profiles match closely at the throat ($x/h = 0$) and immediate next probe location ($x/h = 1$), however, as we move along further downstream there are differences between the results obtained from the present solver and those obtained by Molla et al. [52]. There is a back flow that is detected by the present simulations at the lower wall that is noticed at $x/h = 3$ and $x/h = 4$, however, such a back flow region is absent in the results of Molla et al. [52]. Also on the top wall the back flow region seems to be extending from $x/h = 1$ till beyond $x/h = 2$, whereas back flow region is only limited between $x/h = 1$ and $x/h = 2$ in the results of Molla et al. [52]. As we move further downstream a fully developed turbulent profile is noticed and both results seem to overlap. These discrepancies are thought to be arising because of different SGS stress models used in the studies under consideration.

Wall shear stresses play an important role in the formation of atherosclerosis lesions. The calculation of wall shear stresses is an important step in any hemodynamics calculations. Since, in the present study the wall shear stresses occurring in the thoracic aorta are going to be computed, we first validate the wall shear stresses obtained from the present WenoHemo solver with those reported by Mittal et al. [51] and Molla et al. [52]. A skin friction coefficient is defined as, $C_f = 2\tau_w/\rho\overline{U}^2$, where τ_w is the

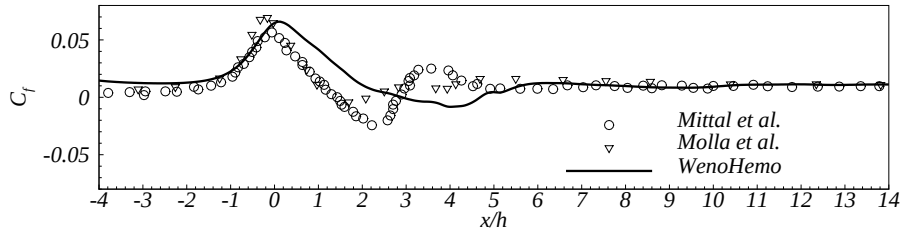

(a) Lower wall

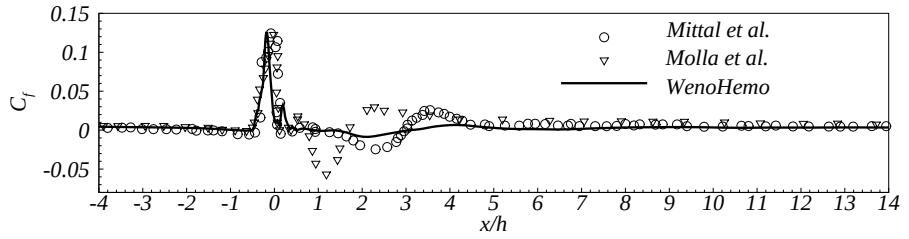

(b) Upper wall

Figure 3.19. A comparison of skin friction coefficient on the lower and upper walls between the present simulation and the previous LES simulations of Mittal et al. [51] and Molla et al. [52].

wall shear stress. The variation of skin friction coefficient along the axial direction on the lower and upper walls is shown plotted in frames (a) and (b) of Fig. 3.19. As we can see from this figure the peak values of the skin coefficient match closely with the other results reported in the literature, however, there are discrepancies that exist at other locations.

In this model stenosis problem, the flow breaks down into small scale turbulence in the post stenotic region. The unsteady jet that gets issued from the stenotic region can be identified by looking at the contours of nondimensional vorticity magnitude $|\omega|h/\overline{U}$ as shown in frame (a) of Fig. 3.20. The coherent structures that are present in the post stenotic region are educed using the λ_2 criterion and are shown plotted in frame (b) of Fig. 3.20. From these figures the shear layer instabilities and the introduction of three dimensional effects beyond $x/h = 4$ are observed.

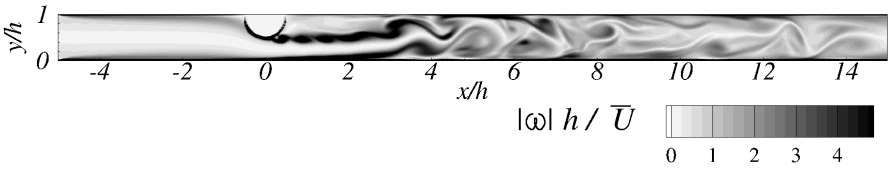

(a)

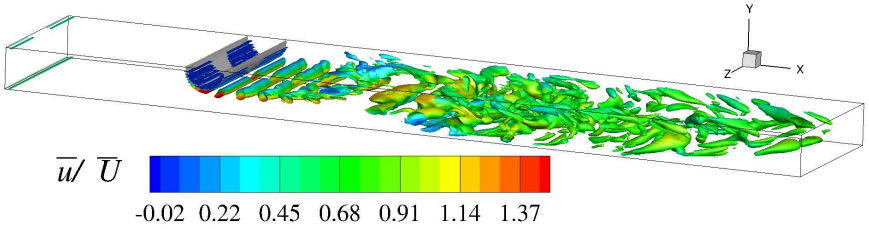

(b)

Figure 3.20. (a) Instantaneous contours of normalized vorticity magnitude on the central $z = 0$ plane. (b) Instantaneous iso-surfaces of λ_2 colored by normalized axial velocity, visualizing the coherent structures in the post stenotic region.

3.5 LES of Non-Cavitating and Cavitating Mixing Layer

3.5.1 Motivation

Another objective of the present study is to simulate and look for possible evidence of cavitation in the case of blood flow occurring in BMHV. A cavitation model will be implemented in to the code and it will be first validated with the available data. The experiments on cavitating and non-cavitating mixing layer were conducted by Aeschlimann et al. [53], and we would use this data to validate the WenoHemo solver together with the cavitation model. In the present chapter, we provide quantitative validations for the non-cavitating mixing layer case with the experimental results and only qualitative validation for the cavitating mixing layer case.

3.5.2 Introduction

A mixing layer is one of the classical free shear layer problems that was studied in experimental and computational fluid mechanics. A shear layer is characterized by a velocity discontinuity between two fluids. When fluid is issued from either side of the splitting plate at different velocities ($U1$ on the upper side is taken to be larger than the $U2$ on the lower side of the plate) Kelvin-Helmholtz instabilities develop at the interface of the fluid streams and creates eddies as shown schematically in Figure 3.21. This region where eddies get formed and grow as they convect downstream where vorticity production takes place is terms as the mixing layer. When these eddies become large enough they interact with the neighbors forming pairing and thereby creating a larger eddy [54]. A shear layer can be characterized by its growth rate δ'_ω, which stays constant along the longitudinal direction (x) when the flow becomes self-similar, as,

$$\delta'_\omega = \frac{d\delta_\omega}{dx}, \tag{3.5}$$

where δ_ω is the vorticity thickness, defined as follows

$$\delta_\omega = \frac{\Delta U}{\frac{dU}{dy}|_{max}}, \tag{3.6}$$

where $\Delta U = U_1 - U_2$, U_1, and U_2 are the velocities of the fluid on the upper and lower side of the splitting plate as shown in Figure 3.21. The tip of the splitter plate is located at $x = 0$ and $y = 0$ and the computational domain starts this location. Aeschlimann et al. [53, 55] performed non-cavitating and cavitating mixing layer simulations using X-ray attenuation measurements. In the present work, simulations of non-cavitating mixing layer are performed and compared the computed results with the experimental results of Aeschlimann et al. [55]. The details of the domain and the operating conditions were taken to be same as the experiments [55], are, as follows. The thickness of the splitting plate (h) is $6mm$, the velocities on the upper and lower side of the splitter plate are $U_1 = 15.8m/s$, and $U_2 = 3.5m/s$, giving the difference in velocities to be $\Delta U = 12.3m/s$. The boundary layer thickness on the upper and lower sides of the splitting plate are, $\delta_1 = 7mm$, and $\delta_2 = 4mm$ respectively. The length

and velocity scales for the simulation are taken as, the thickness of the splitting plate (h), and the velocity difference (ΔU). However, the results are presented with a mix of dimensional and non-dimensional quantities so as to be able to compare them to the experimentally measured curves. The length scale could also be taken as the vorticity thickness as was done in other studies, but in the present study, δ_ω was taken as length scale only during presenting the results. The Re is $73,800$ calculated based on h and ΔU, and by taking the kinematic viscosity of water as $\nu_{water} = 1.0e-06$

The simulation domain extends $60 \times 40 \times 10$ non-dimensional units in the x, y, and z respectively. Blasius boundary profile was with the exact boundary layer thickness as in the experiments on the upper ($y \geq 0$) and lower ($y < 0$) regions of the inlet. At the exit of the domain in x-direction at $x = x_{max}$ a simple homogeneous Neumann boundary condition on all components of velocity were used. In the lateral direction, on the planes $y = y_{min}$ and $y = y_{max}$, a impermeable, slip condition was used. In the z direction free slip boundary condition was used on all the velocity components. Homogeneous Neumann boundary condition on pressure was used on all the boundary planes except at the exit of the domain ($x = x_{max}$), where a Dirichlet boundary condition with $p = 0$ was used. Random velocity perturbations were imposed at the inflow plane in the boundary layer region only on the v-component of velocity, so that, the flow breaks down into turbulence within the simulation domain considered. The maximum value of the perturbation velocity was chosen as 0.05 the mean velocity. The simulation domain was discretized into 6 by 5 blocks in x, and y direction respectively. Within each block the mesh size was chosen as $60 \times 41 \times 50$ in the x, y, and z directions amounting to a total resolution of 3.69 million grid points. The time step was taken as 0.01 and the simulation was run till a non-dimensional time of 500 of which the last 200 time steps was used to collect the turbulent statistics defined in section 2.9.

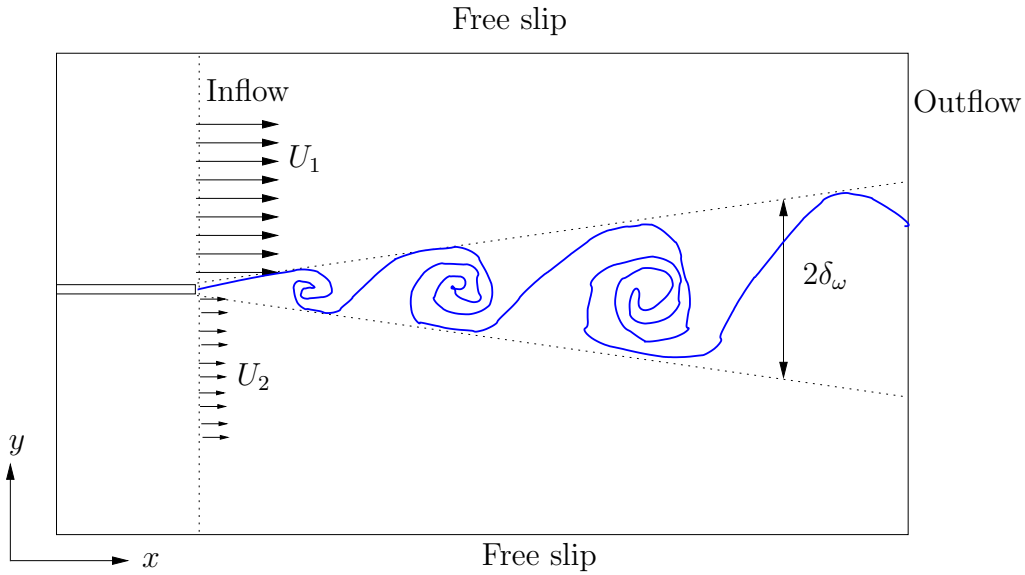

Figure 3.21. Schematic of the mixing layer, showing the higher and lower velocities issuing from either side of the splitter plate.

3.5.3 LES of Non-Cavitating Mixing Layer

First we compare the evolution of the vorticity thickness, between the present simulations and the experiments [55]. The evolution of the vorticity thickness (δ_ω) is shown plotted in Figure 3.22. The vorticity growth rate obtained from the experiments is $\delta'_\omega = 0.123$, which is very close to the growth rate obtained from the present simulations, which is 0.098. The location where the mixing layer becomes self-similar is strongly dependent on the inlet turbulence levels and the effect of the wake of the splitting plate. Hence, the location where the vorticity thickness (δ_ω) grows at a constant rate is not the same between experiments and the simulation, and that is acceptable as long as the vorticity growth rate is predicted accurately. With properly chosen non-dimensional length and velocity scales, the time averaged longitudinal velocity profiles at various x locations become self-similar. To verify this fact, we plotted the time and span-wise averaged longitudinal velocity profiles non-dimensionalized using the vorticity thickness ($\delta_\omega(x)$) as the length scale and ΔU as the velocity scale, in Figure 3.23. The y_{ref} in Figure 3.23, is the location where $\overline{\langle u \rangle_z} = \frac{(U_1+U_2)}{2}$. As we can see from Figure 3.23, various velocity profiles collapse onto one single curve demonstrating the self-similar nature. Further, we compare the averaged longitudinal velocity profiles with the experiment in Figure 3.24. Frame (a) of the Figure 3.24 shows the velocity vectors, and contours of averaged longitudinal velocity obtained from experiments [55], and (b) shows those obtained from Weno-Hemo. This comparison presents a qualitative comparison between the two, which nonetheless helps in assessing the simulation results with in visual limits. Next we turn our focus to look at the second order statistics. First, we compare the z-averaged r.m.s longitudinal velocity fluctuations plotted along y in Figure 3.25. As we can see from this figure a very good agreement is obtained with the experiments [55]. Both the trend as well as the peak value of the variation of longitudinal velocity fluctuations is captured very closely by the present simulation. The lateral velocity fluctuations, as well as the turbulent diffusion, also show profiles similar to the longitudinal veloc-

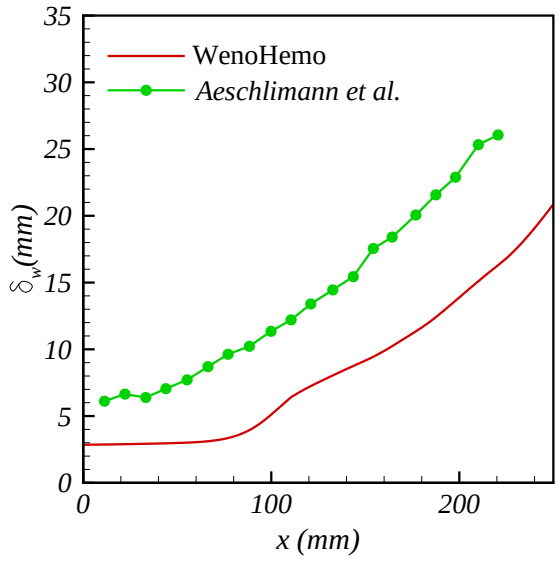

Figure 3.22. Comparison of vorticity thickness ($\delta_\omega(x)$) evolution between present simulations and experimental results of Aeschlimann et al. [55].

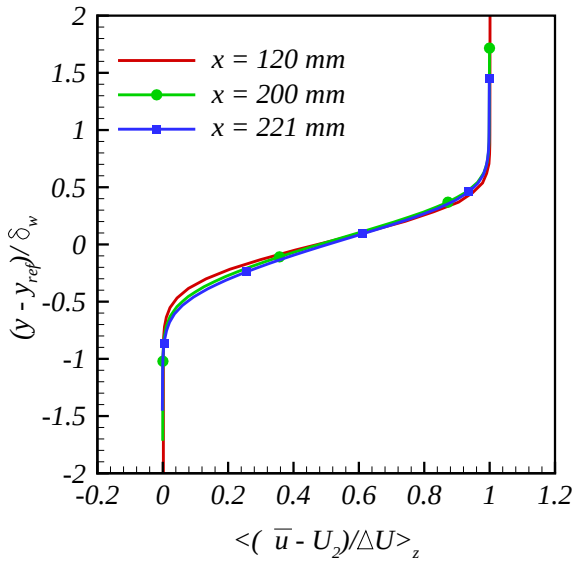

Figure 3.23. Self similar solution of the time-averaged non-dimensional axial velocity at indicated axial locations.

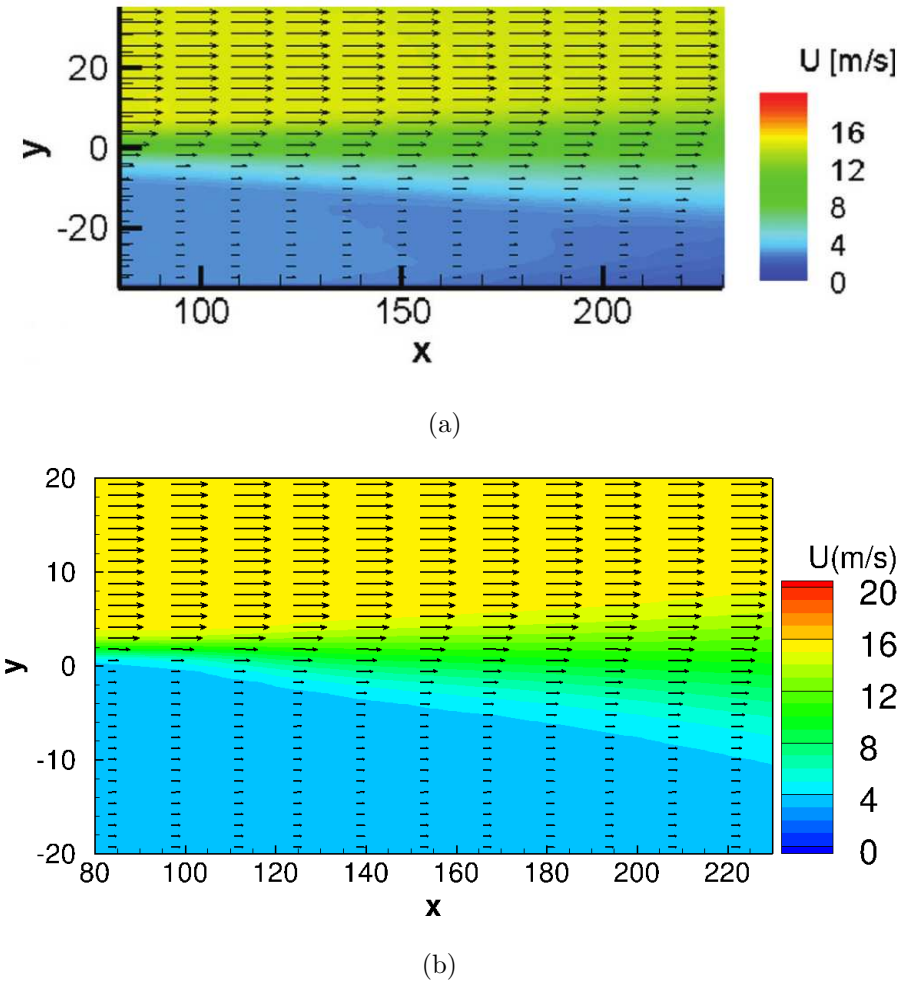

Figure 3.24. Comparison of mean velocity profiles between (a) experimental results of Aeschlimann et al. [55] and (b) present computations using WenoHemo.

ity fluctuations. The profiles, attain a maximum value at the center of the mixing layer, decreasing to zero outside the mixing area. Hence, further comparisons between experiments and simulations were only made, by comparing the variation of the maximum fluctuation values (obtained at $y = 0$) along the longitudinal direction (x). The

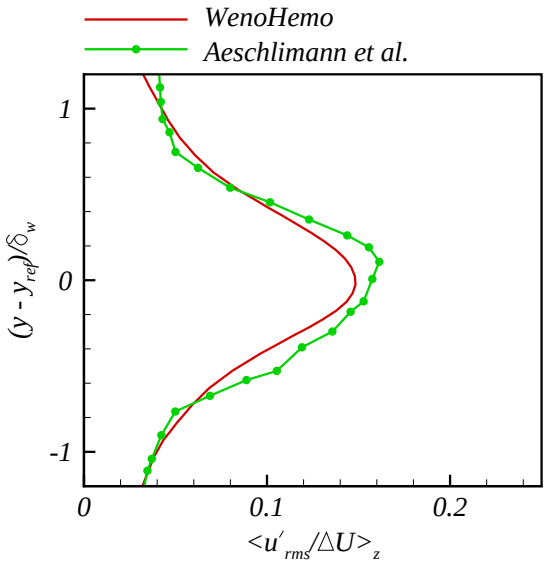

Figure 3.25. Comparison of longitudinal velocity fluctuations between present simulations and experimental results of Aeschlimann et al. [55], at $x - x_0 = 120\ mm$.

longitudinal velocity fluctuations are shown plotted in Figure 3.26 as a function of x. As we can see from Figure 3.26, the fluctuations stabilize to a constant value in the self similar region. The same behavior is observed both from the experiments [55], as well from the present simulations. The lateral velocity fluctuations also show a similar behavior, as can be noted from Figure 3.27. Next, we compare evolution of turbulent diffusion along the longitudinal axis. The turbulent diffusion ($u'v'$), was negative in the mixing layer region, reaching a maximum absolute value at the center of the mixing layer, and null outside the mixing layer region. The evolution of turbulent diffusion is compared in Figure 3.28, and as can be seen excellent agreement is reached between the present simulations and the experiments [55].

Further, we notice that the longitudinal fluctuations have a greater amplitude, than the transverse ones, a tendency that was also observed in shear flows. Having compared several quantities to the experiments, we now look at the instantaneous vortical structures produced in the flow. The iso-surfaces of $\lambda_2 = -0.01$ criterion of Jeong & Hussain [56] are shown plotted in Figure 3.29. The intense mixing and the three-dimensionality of the flow can be clearly noticed from these Figures. In order to visualize the vortex pairing in the mixing layer region, we plot the instantaneous z-vorticity contours on the mid plane ($z = 0$) in Figure 3.30. The core of these vortical regions or eddies are the regions of low pressure. These low pressure regions are sources of cavitation formation. In Figure 3.31, we plot the iso-surface of pressure ($p = -0.11$) overlapped on the z-vorticity contours on the mid-plane. We can see from Figure 3.31, the low pressure regions occurring at the core of the eddies.

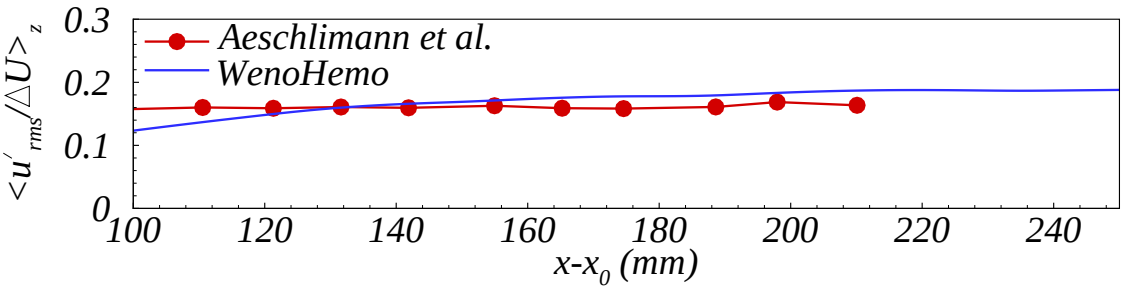

Figure 3.26. Comparison of maximum longitudinal velocity fluctuations ($\langle u'_{rms}/\Delta U\rangle_z$) between present simulations and experimental results of Aeschlimann et al. [55], along the longitudinal direction ($x - x_0$) at $y = 0$.

3.5.4 Cavitation Modeling

Introduction

Cavitation is evaporation of the fluid when the local fluid pressure falls below the vapor pressure of the fluid. Evaporation of liquid can happen either because

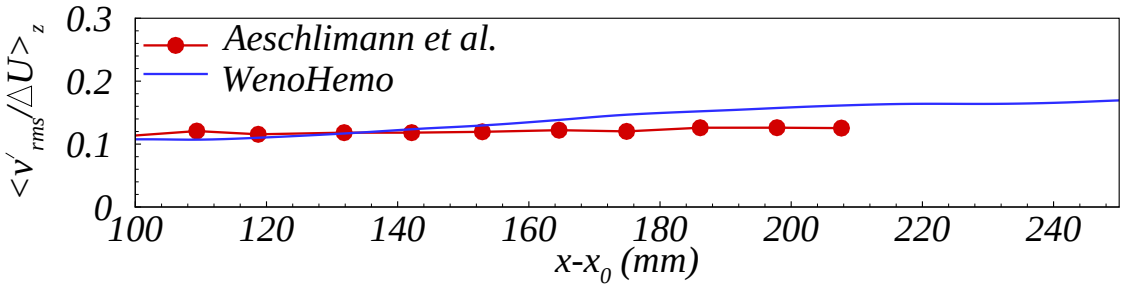

Figure 3.27. Comparison of maximum lateral velocity fluctuations ($\langle v'_{rms}/\Delta U\rangle_z$) between present simulations and experimental results of Aeschlimann et al. [55], along the longitudinal direction ($x - x_0$) at $y = 0$.

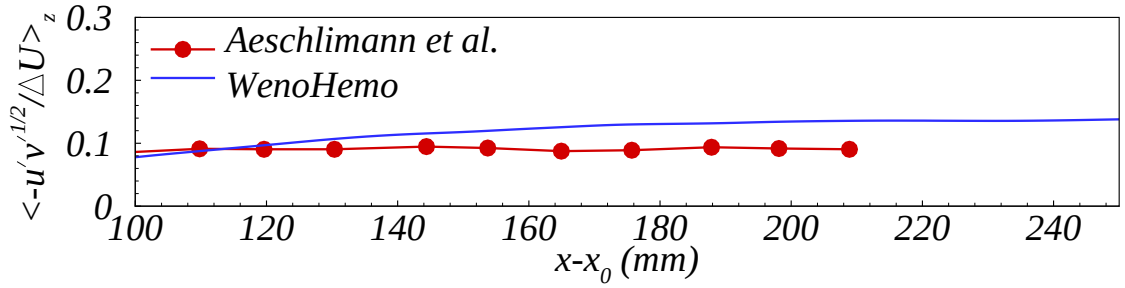

Figure 3.28. Comparison of maximum turbulent diffusion ($\langle\sqrt{-u'v'/\Delta U^2}\rangle_z$) between present simulations and experimental results of Aeschlimann et al. [55], along the longitudinal direction ($x - x_0$) at $y = 0$.

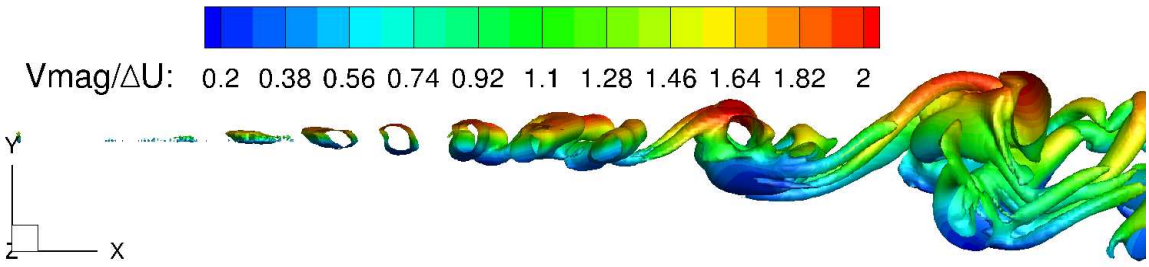

(a) xy plane

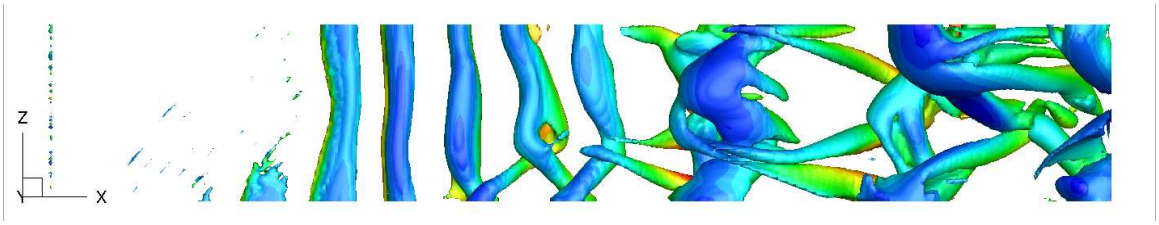

(b) xz plane

Figure 3.29. Instantaneous vortical structures in the spatially developing mixing layer visualized by plotting iso surfaces of $\lambda_2 = -0.01$, colored by non-dimensional velocity magnitude shown on two different planes.

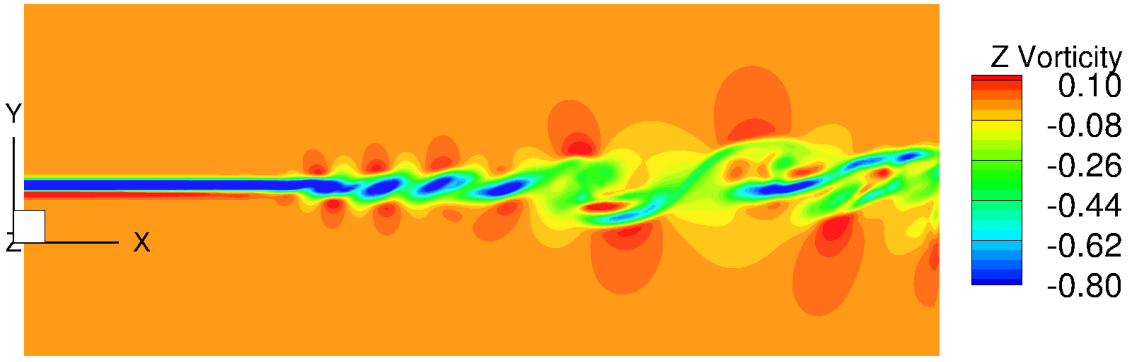

Figure 3.30. Instantaneous z-vorticity contours plotted on the mid plane, $z = 0$.

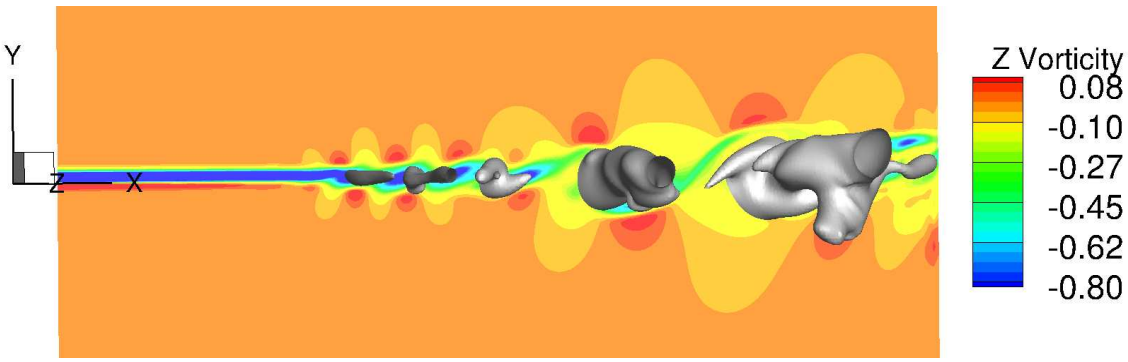

Figure 3.31. Instantaneous iso-baric surface of $p = -0.11$ shown together with the z-vorticity contours on the mid plane, $z = 0$.

of boiling or cavitation. Boiling occurs when the local temperature is greater than the boiling point of the liquid. Whereas, in cavitation although the temperature is much below the boiling point of the liquid the reduction in pressure below the vapor pressure of the liquid causes the liquid to evaporate. The phase change from liquid to vapor makes the local speed of sound to drop by a factor of 1000 making the flow in the two-phase flow occurring in the mixing region to be supersonic. Cavitation can be simulated by two different approaches. The direct and most straight forward approach is to integrating the compressible Navier Stokes equations, together with a homogeneous equilibrium model, as was done in studies performed by Shin et al. [57] and Dittakavi et al. [58], and many other studies not listed here. The other approach is to use the incompressible Navier-Stokes formulation and solve a separate scalar transport equation for describing the evolution of the liquid fraction equation. This approach was used in a number of studies [59–62]. In the present study, we take the latter route to cavitation modeling and specifically work with the model described in Senocak et al. [59] with the phase transformation rates taken from Kunz et al. [63]. The governing equations are presented in the next section for solving the multi-phase flow arising in the mixing layer region in the cavitating case.

Governing Equations

The governing equations for the cavitating mixing layer simulation are the incompressible mixture fraction equations together with a separate scalar equation for the liquid fraction as shown below,

$$\frac{\partial \rho_m}{\partial t} + \frac{\partial}{\partial x_j}(\rho_m \, u_j) = 0 \tag{3.7}$$

$$\frac{\partial(\rho_m u_i)}{\partial t} + \frac{\partial}{\partial x_j}(\rho_m u_i u_j) = -\frac{\partial p}{\partial x_i} + \frac{\partial}{\partial x_j}\left(\mu_m \left(\frac{\partial u_i}{\partial x_j} + \frac{\partial u_j}{\partial x_i} - \frac{2}{3}\frac{\partial u_k}{\partial x_k}\delta_{ij}\right)\right) \tag{3.8}$$

$$\frac{\partial \alpha_l}{\partial t} + \frac{\partial(\alpha_l u_j)}{\partial x_j} = (\dot{m}^- + \dot{m}^+) \tag{3.9}$$

The mixture density ρ_m and the mixture viscosity μ_m are defined as follows:

$$\rho_m = \rho_l \alpha_l + \rho_v (1 - \alpha_l) \tag{3.10}$$

$$\mu_m = \mu_l \alpha_l + \rho_v (1 - \alpha_l) \tag{3.11}$$

where ρ_l is the liquid density, ρ_v is the density of the vapor, u_j is the mixture velocity vector, p is the mixture pressure, α_l is the liquid fraction, $\dot{m}^-$, and $\dot{m}^+$ are the source terms modeling the evaporation and condensation respectively. Using the continuity equation 3.7, the momentum equation 3.8 can be simplified as follows,

$$\rho_m \left(\frac{\partial u_i}{\partial t} + u_j \frac{\partial u_i}{\partial x_j} \right) = -\frac{\partial p}{\partial x_j} + \frac{\partial}{\partial x_j} \left(\mu_m \left(\frac{\partial u_i}{\partial x_j} + \frac{\partial u_j}{\partial x_i} - \frac{2}{3} \frac{\partial u_k}{\partial x_k} \delta_{ij} \right) \right). \tag{3.12}$$

We can further modify the Eq. 3.12, by defining the following nondimensionalization $u_i = U u_i^*, \rho_m = \rho_l \rho_m^*, t = \frac{l}{U} t^*, \mu_m = \mu_l \mu_m^*, Re = \rho_l l U / \mu_l$. The above momentum equation can be re-written, after dropping the asterisk in the superscript and noting that all the terms are now in dimensionless form, as follows,

$$\rho_m \left(\frac{\partial u_i}{\partial t} + u_j \frac{\partial u_i}{\partial x_j} \right) = -\frac{\partial p}{\partial x_i} + \frac{1}{Re} \frac{\partial}{\partial x_j} \left(\mu_m \left(\frac{\partial u_i}{\partial x_j} + \frac{\partial u_j}{\partial x_i} - \frac{2}{3} \frac{\partial u_k}{\partial x_k} \delta_{ij} \right) \right). \tag{3.13}$$

The momentum equation is further filtered and results in a SGS stress tensor that needs to be modeled. In the present work, we use Vreman [20] model to compute this tensor. The filtered equations are written as follows,

$$\overline{\rho_m} \left(\frac{\partial \overline{u_i}}{\partial t} + \overline{u_j} \frac{\partial \overline{u_i}}{\partial x_j} \right) = -\frac{\partial \overline{p}}{\partial x_i} + \frac{1}{Re} \frac{\partial}{\partial x_j} \left(\overline{\mu_m} \left(\frac{\partial \overline{u_i}}{\partial x_j} + \frac{\partial \overline{u_j}}{\partial x_i} - \frac{2}{3} \frac{\partial \overline{u_k}}{\partial x_k} \delta_{ij} \right) \right) + \overline{\rho_m} \frac{\partial \tau_{ij}}{\partial x_j}. \tag{3.14}$$

Like before, the SGS stress tensor τ_{ij} only contains the anisotropic part and the isotropic part is absorbed into the filtered pressure field. The expression for the anisotropic SGS stress tensor is written as follows,

$$\tau_{ij} = \overline{u_i u_j} - \overline{u_i} \, \overline{u_j} - \frac{1}{3} (\overline{u_i u_j} - \overline{u_i} \, \overline{u_j}). \tag{3.15}$$

The source terms $\dot{m}^-$ and $\dot{m}^+$ that represent condensation and evaporation processes are taken from Senocak [59] and are given as follows,

$$\dot{m}^- = \frac{C_{dest} \rho_v \alpha_l \mathrm{MIN}(0, p - p_v)}{\rho_l \left(1/2 \rho_l U_0\right) t_0} \tag{3.16}$$

$$\dot{m}^+ = \frac{C_{prod} \rho_v \alpha_l^2 (1 - \alpha_l)}{\rho_l t_0} \tag{3.17}$$

where t_0 is the time scale which is the ratio of characteristic length scale l to the reference velocity (l/U_0) and C_{dest} and C_{prod} are empirical constants taken from Senocak et al. [59] as 9×10^5 and 3×10^4 respectively. The ratio of liquid to vapor densities ρ_l/ρ_v is taken equal to 1000.

3.5.5 LES of Cavitating Mixing Layer

The simulations are performed for the same back pressure setting as in case 3 of the experiments of Aeschlimann et al. [55]. The simulations are started from a non-cavitating case that was previously run and the cavitation model is switched on then on. A qualitative comparison of the contours of liquid fraction obtained are shown in Figure 3.32. Frame (a) depicts the instantaneous results from the experiments [55], whereas frame (b) denotes the instantaneous values obtained from the present simulation. The experimental values indicate a maximum vapor fraction of 30% for the darkest contours whereas only as high as 10% vapor fraction is achieved in the present simulations. This indicates that the model parameters may have to tuned in order to match the experimental results accurately for at least one of the cases and then these should hold good for the other cases to be studied. The variation of vapor fraction profiles along y direction when plotted with proper nondimensionalization should result in a self similar profile. In order to verify this fact, void fraction profile are extracted at three locations along the axis of the mixing layer and are shown in Figure 3.33. As we can see from this figure a perfect self similarity of the profiles is not attained and the deviations are more in the lower speed side of the mixing layer than on the upper side which is located in the high speed stream. The results obtained from the present simulations can only be considered to be qualitatively validated as a perfect match with the experimentally measured values was not obtained rather only a similar trend is observed.

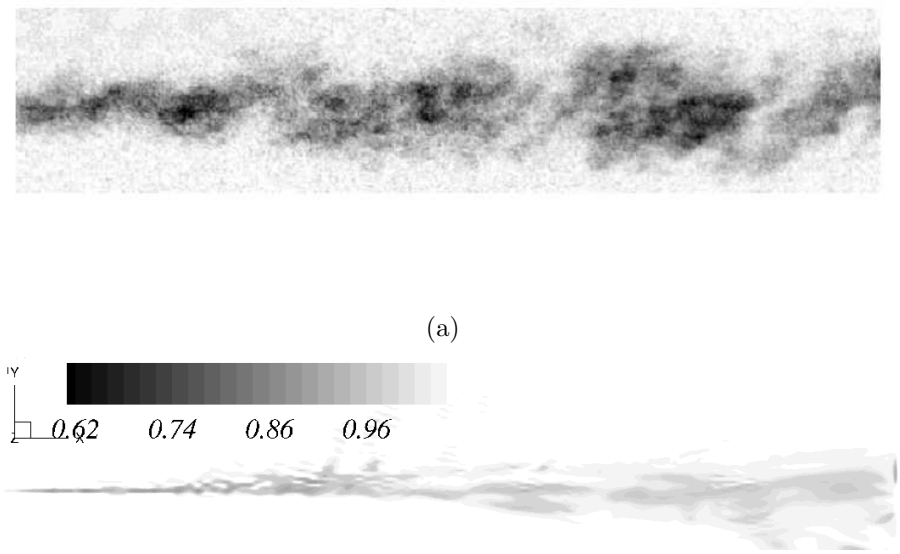

Figure 3.32. Qualitative comparison of experimental and numerical simulations obtained for the liquid fraction. (a) Instantaneous contours of liquid fraction on the central plane $z = 0$ from experiments of Aeschlimann et al. [55]. (b) Instantaneous contours of liquid fraction on the central plane $z = 0$ from simulation.

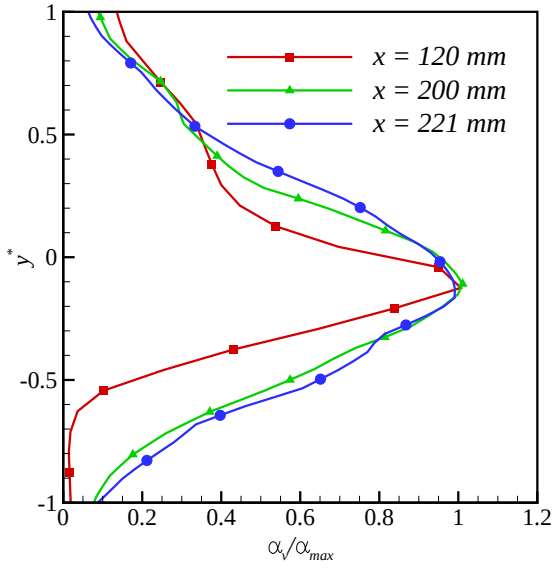

Figure 3.33. Variation of void fraction along the y axis at indicated axial locations.

3.5.6 Summary

In summary, we performed non-cavitating and cavitating mixing layer simulations with the WenoHemo solver and compared the results to the experiments [55]. A very good agreement in results is obtained validating the numerical methodology used in WenoHemo solver for the non-cavitating mixing layer case. However, only qualitative validation of the cavitating mixing layer case is obtained and future work should focus on performing quantitative validation of the results.

4. LARGE EDDY SIMULATION OF BLOOD FLOW IN AORTA

4.1 Introduction

4.1.1 Anatomy of Aorta

The aorta is the largest artery in the human body. It originates from the left ventricle of the heart and extends down to abdomen where it separates into two smaller arteries known as the common iliacs. The oxygenated blood from heart is carried by the aorta and supplied to the body through systemic circulation. A schematic of the aorta is shown in Figure 4.1(a), which shows its relative location with respect to the heart. Normally the aorta is left sided and in very rare cases right sided aortas were found. The left and right references in this entire chapter are with respect to the subject in discussion. The aorta can be divided into four distinct segments as follows

- Ascending aorta
- Aortic arch
- Descending aorta
- Abdominal aorta

The various segments are shown marked in Figure 4.1(b). Oxygenated blood is pumped by heart into the ascending aorta during systole through the opening and closing of the aortic valve. Aortic valve is a tri-cuspid valve that operates based on the pressure differential between the left ventricle and the aorta. Aortic arch is a U shaped lumen that divides into three smaller arteries namely, brachiocephalic artery, left common carotid artery, and left subclavian artery. The brachiocephalic artery further bifurcates into right subclavian and right common carotid arteries. Only a

small portion of the blood is carried by these four arteries and a major portion of oxygenated blood enters the descending aorta and further into the abdominal aorta. The left and right common carotid arteries supply the blood to the head and neck, whereas the left, and right sub-clavian arteries supply the blood to the left, and right hand respectively.

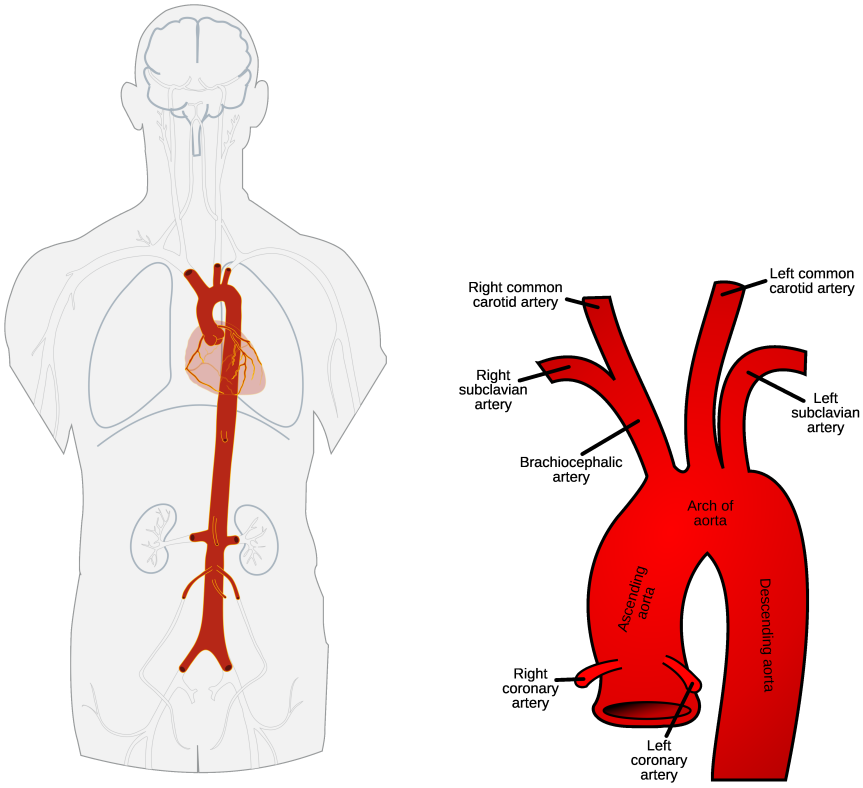

(a) Schematic of the aorta showing the three main branches emanating from the aortic arch

(b) Schematic of the thoracic aorta depicting its various segments and branches

Figure 4.1. Schematic of the human aorta. Source: Wikipedia.

The aortic walls are made up of three layers, and are contracting and expanding as blood is pumped through them. As a result the middle layer is prone to thinning and can cause potential rupture. The thinning of the aortic walls leads to a pathological condition known as an aneurysm which is further described in the next section.

4.1.2 Aortic Aneurysm

Aneurysm is a permanent dilatation or ballooning of the aorta. Aneurysms pose a danger as they can potentially rupture and cause severe bleeding. The thinning of the aortic walls leads to the ballooning effect and they can be broadly classified into two categories depending on their structure, as follows,

1. Saccular Aneurysm
2. Fusiform Aneurysm

The saccular aneurysm looks more like a sac/bag, whereas the fusiform aneurysm is a local dilatation which looks similar to a elongated, spindle like swelling. The aneurysm we will be dealing with in this thesis is fusiform aneurysm. Further depending on the location where an aneurysm occurs in the aorta it can be classified as follows,

- Ascending thoracic aortic aneurysm
- Aortic arch thoracic aneurysm
- Descending thoracic aortic aneurysm

In the present work, we focus on descending thoracic aortic aneurysm and here after refer to that by just thoracic aortic aneurysm (TAA).

4.1.3 Aortic Aneurysm Repair

Aneurysms whose diameter is more than 1.5 times the normal diameter of the aorta have to be surgically repaired as they can potentially rupture causing bleeding. The two common types of aneurysm repair are the following,

- Thoracic aortic aneurysm open repair
- Endovascular aneurysm repair (EVAR)

The thoracic aortic aneurysm open repair procedure involves making a large incision and allows the surgeon to visualize the aorta directly to repair the aneurysm by replacing the walls of the aneurysm with a synthetic graft. In the EVAR procedure, only a small incision needs to be made and guided through X-ray imaging and specifically designed instruments a tube known as stent-graft is inserted and secured in place through barbs and hooks. The stent-graft acts like a new lumen allowing the blood to pass through it and the aneurysm region will be completely concealed thereby not allowing it to grow or burst in future.

4.1.4 Objectives of the Present Study

We study the blood flow in AAA and thoracic aortic aneurysm (TAA). Further we investigate the resulting difference in hemodynamics in a thoracic aorta with the introduction of the stent graft (TASG). We perform a comparison of the results obtained with the present solver with the experimental results of Asbury et al. [6]. The time averaged axial velocity profiles and axial variation of turbulence intensity in the case of steady inflow to AAA at two different Reynolds numbers are used to make the comparisons.

4.2 Steady Inflow in Abdominal Aortic Aneurysm (AAA)

The geometry of the AAA, used in the simulations is shown in Figure 4.2, which is obtained from the article by Asbury et al. [6]. The diameter ratio (D/d), where D is the diameter of the aneurysm, and d is the diameter of the undilated portion of the artery equals 2.75. A steady velocity was imposed with parabolic profile at the inlet of the geometry. Two different Re configurations were simulated. The $Re = 500$ case is a laminar case, and the $Re = 2600$ case is a turbulent case. The domain extended from $-8d$ to $+10d$ in the x-direction and $1.2D$ in both y and z directions. A total of 22 blocks were used to discretize the domain with $40 \times 50 \times 80$ grid points in each

of the x, y, and z directions in each block amounting to a total of 3.52 million grid points.

We simulate steady inflow in AAA for which experimental results are available in the literature. The blood flow through the arterial network is remarkably stable and the arterial walls withstand the repetitive wall stress. Unfortunately, in some cases, due to disease or other complex processes, the arterial wall becomes weak and bulges out permanently forming an aneurysm [64]. Although, there are many sites at which aneurysms can form in the arterial tree, the most common are thoracic aortic aneurysms, abdominal aortic aneurysms and cerebral aneurysms. In the present section, we focus on steady inflow simulations in AAA and comparing them to the experimental results of Asbury et al. [6]. The walls of the aorta are assumed to be rigid.

The geometry of the AAA considered in the present work is taken from the experiments of Asbury et al. [6] and is shown in Figure 4.2(a). The inlet and outlet to the aorta have the same diameter ($d = 2r_i$), whereas the diameter of the aneurysm is denoted by D. The diameter ratio of the aneurysm $D/d = 2.75$ is considered in the present work. Two different Reynolds numbers 500 and 2600 are considered. The diameter of the inlet (d) and the average velocity at the inlet section ($\overline{U}$) are used as the length scale and the velocity scale respectively to define the Reynolds number. A parabolic inlet velocity profile is applied at the inlet of the domain, and a homogeneous Neumann boundary condition is applied to all the velocity components at the outlet of the domain. A Dirichlet boundary condition on the pressure is applied at the outlet of the domain and a homogeneous Neumann boundary condition for pressure is set on all other boundaries. Figure 4.2(b) shows the multiblock decomposition of the AAA geometry into 81 equal sized blocks used for the simulation. The length of the domain from inlet to outlet measures $18d$. Each block has a mesh of $24 \times 24 \times 80$ making it a total mesh resolution of 3.7 million points.

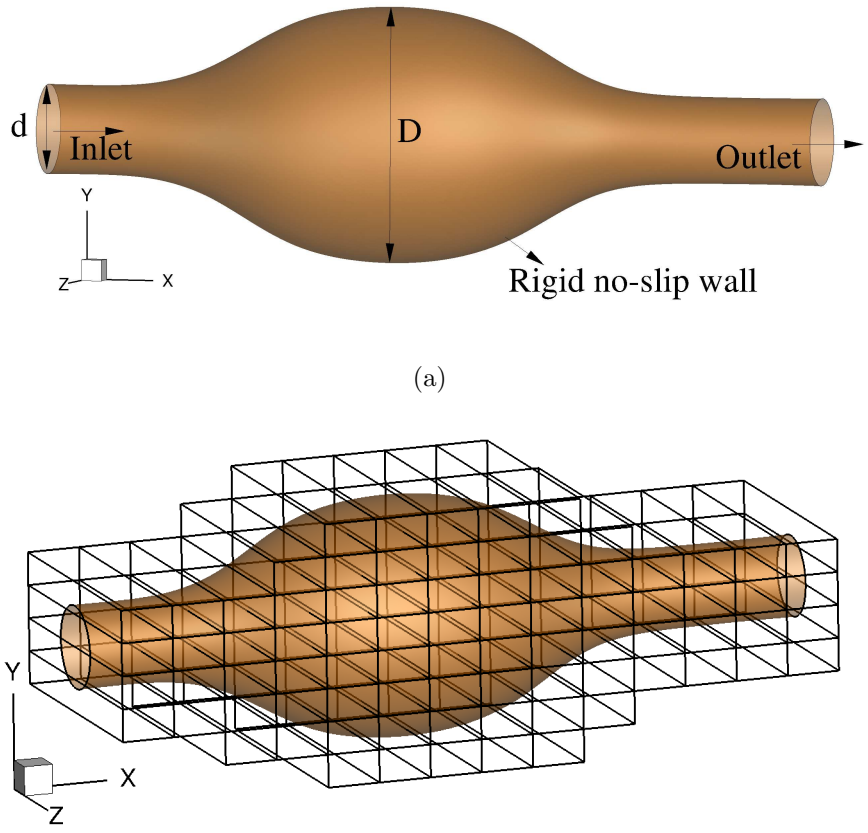

(a)

(b)

Figure 4.2. (a) Geometry of AAA reconstructed from the experiments of Asbury et al. [6]. (b) Multiblock decomposition of AAA into 81 equal sized blocks.

4.2.1 Re = 500

The profiles of mean axial velocity $< \overline{u} > /\overline{U}$ are shown in Figure 4.3(a), at indicated locations along the streamwise direction of the aorta on the xy-plane, at $z = 0$, at a Reynolds number of 500. The operator <> denotes time average or mean quantity. A good match between the present simulation results and the experimental results of Asbury et al. [6] is seen from the figure. The parabolic shape of the velocity profiles is maintained similar to the experimental results throughout the abdominal aorta. The streamlines on the xy-plane at $z = 0$ are shown in Figure 4.3(b). From Figure 4.3(b) the recirculating fluid in the aneurysm can be clearly noticed. The recirculating region has a center measured in the xy-plane at $(2.25r_i, 1.55r_i)$.

4.2.2 Re = 2600

Next, we compare the results obtained for a Reynolds number of 2600. The profiles of mean axial velocity ($< \overline{u} > /\overline{U}$) are shown in Figure 4.4(a) at several locations along the axis of the aorta in the xy-plane at $z = 0$. Compared to the 500 Reynolds number case, a clear recirculation zone is noticed from the Figure 4.4(a). A perfect match with the experimental results could not be obtained, but until $x/r_i = 4$, the peak and the qualitative behavior of the profiles is captured by the simulations. The experimental results are not quite symmetric about the $y = 0$ line. The streamlines in the xy-plane at $z = 0$ are shown in Figure 4.4(b). The recirculating eddy seems to be more elongated and pushed towards the distal end of the aorta in this case when compared with the Reynolds number of 500 case. The center of the recirculating fluid, when measured in the xy-plane has a center at $(3.74r_i, 1.16r_i)$, which is nearer to the distal end by a value of $1.5r_i$ units and closer to the axis of the aorta by $0.4r_i$ when compared with the Reynolds number of 500 case.

The variation of turbulence intensity of the axial component of velocity, defined as $I_u = u'_{r.m.s}/ < \overline{u} >$, is compared next between the present simulations and the experiment for 2600 Reynolds number case. The axial variation of turbulence intensity I_u is

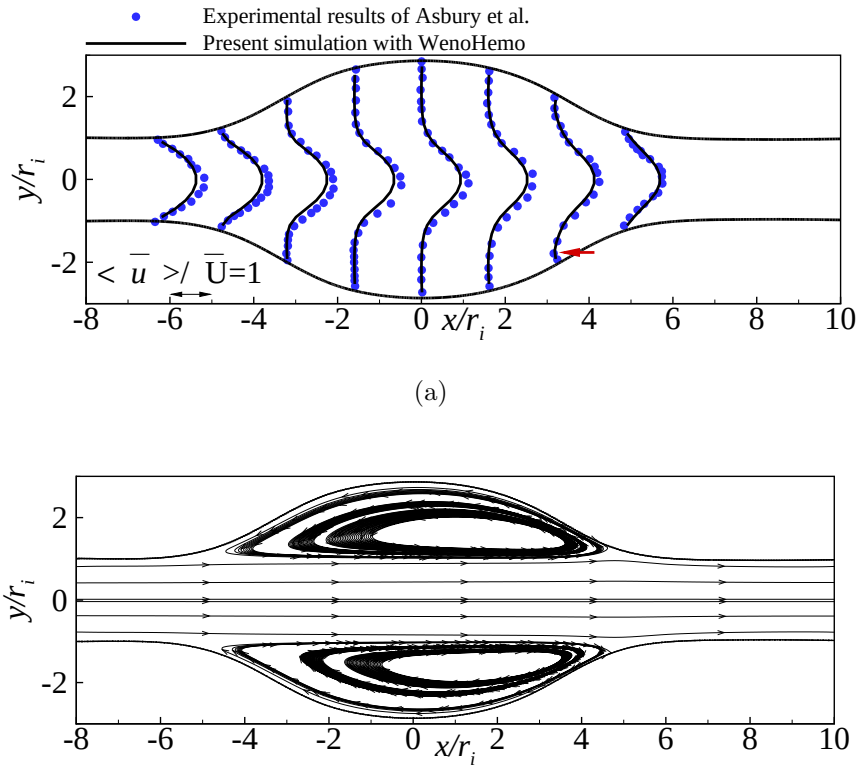

Figure 4.3. (a) Comparison of mean axial velocity profiles between present simulations and the experimental results of Asbury et al. [6] for a Reynolds number of 500. Arrow indicates sample location of retrograde flow close to the wall in the aneurysm region. (b) Streamlines on the xy-plane at $z = 0$, depicting the recirculating zone in the aneurysm region.

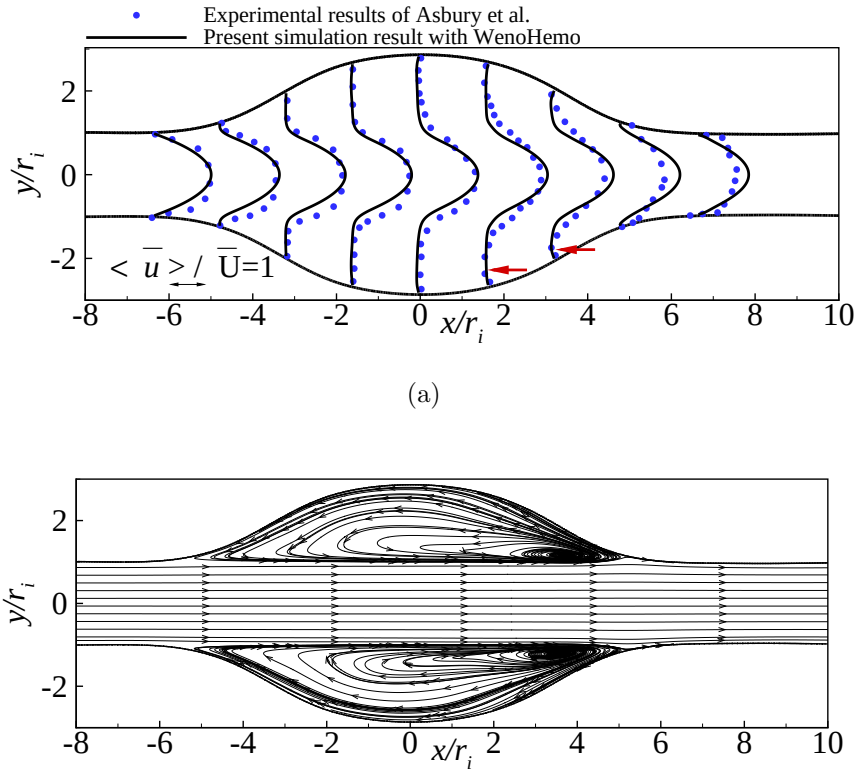

(a)

(b)

Figure 4.4. (a) Comparison of mean axial velocity profiles between present simulations and the experimental results of Asbury et al. [6] for a Reynolds number of 2600. Arrow indicates sample location of retrograde flow close to the wall in the aneurysm region. (b) Streamlines in the xy-plane at $z = 0$, depicting the recirculating zone in the aneurysm region.

shown in Figure 4.5. As we can see from this figure the turbulence intensity increases in the distal portion of the AAA. Towards the distal end both the experimental and present simulations show a match with a value of 14% turbulence intensity, however, in the range $2 \leq x/r_i \leq 10$ only the upward trend is captured. This deviation could be due to differences in inlet turbulence levels between the experiments and the simulations.

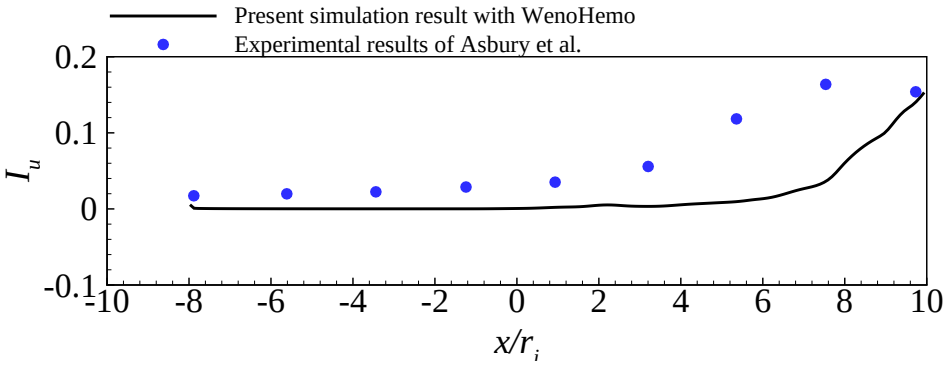

Figure 4.5. Comparison of variation of turbulence intensity along the center line of the AAA at a $Re = 2600$ between simulation and experiment.

4.3 Steady Inflow in a Thoracic Aortic Aneurysm (TAA)

In this section, first investigate steady inflow in TAA. The geometry of TAA together with a multiblock decomposition into 100 blocks is shown in Figure 4.6(a). The particular geometry considered here has an additional 90° bend towards the distal end when compared with typical TAA geometries that are studied in the literature [11]. The motivation behind such an additional bend is that it is supposed to create a worst case scenario with maximum loading imparted on a stent graft placed in this geometry. A bisecting plane cut of the geometry on the xy-plane at $z = 0$ is shown in Figure 4.6(b). In the figure, the surface marked *Inlet* is the inflow surface to the domain, through which the blood pumped by heart enters the aorta. The surfaces $O1, O2, O3$ and $O4$ indicate outlets leading to brachiocephalic artery, left common

carotid artery, left subclavian artery and to abdominal aorta respectively. The diameter of aorta at the outlet $O4$ is same as at the inlet and equal to d. The outlets $O1, O2$ and $O3$ have a diameter of $d/4, d/5$ and $3d/10$ respectively. Several point probes $P1$ through $P5$ and line probes $S1$ through $S10$ are also shown marked on the central xy -plane, which enables analysis of mean and turbulent quantities.

A uniform velocity profile is applied at the inlet of the domain. The diameter at the inlet, d and the average velocity at the inlet, $\overline{V}$, are used as the length scale and the velocity scale to define the Reynolds number. An average Reynolds number of 910 and a peak Reynolds number of 3727 are identified for the present geometry, by considering the physiological wave form used by Lantz et al. [11]. At all the outlets $O1$ through $O4$ homogeneous Neumann boundary condition for velocity is applied. Pressure level is set to a Dirichlet value on the front and back faces of the bounding box in z direction and a homogeneous Neumann pressure boundary condition is applied on all other boundaries.

4.3.1 Re = 910

A multiblock domain with 100 blocks as shown in Figure 4.6(a) is used for the steady inflow simulations at a Reynolds number of 910. As each block is assigned to one processor, the simulations are run on 100 processors. Each block consists of $21 \times 21 \times 81$ mesh points, making a total resolution of 3.6 million points. The contours of normalized vorticity magnitude ($|\omega| d/\overline{V}$) are shown in Figure 4.6(c) on the central xy-plane, at $z = 0$. As the flow turns clockwise from the inlet into the aortic arch and into the aneurysm region, the inner wall boundary layer detached from the wall, whereas the outer wall boundary layer follows the outer contour without permanent separation from the wall. The outer wall boundary layer, however, slightly moves inwards at each of the 90 degrees bends in the aneurysm and descending aorta regions. A steady and laminar flow field is observed in the entire domain under steady inflow conditions at a Reynolds number of 910.

The mean velocity profiles ($< \overline{u} > /\overline{V}$ on lines $S1$ and $S2$ and $- < \overline{v} > /\overline{V}$ on lines $S3$ through $S10$) are shown in Figure 4.7 on several lines indicated in Figure 4.6(b). An almost flat velocity profile is seen at the location $S1$, whereas reverse flow can be seen at the stations $S2$ through $S4$. The lines $S3, S4$ are in the aneurysm region and they have reverse flow extending to 50% of the local diameter at the location as can be seen from this figure. The peak value of the retrograde velocities at locations $S3$ and $S4$ is 20% of $\overline{V}$, whereas at the location $S5$, the retrograde velocity is less than 5% of $\overline{V}$ marking the onset of zero retrograde flow. All the sections downstream of $S5$ do not have any retrograde velocities and profiles at the locations $S8, S9$ and $S10$ seem to have attained a close to a fully developed flow profile.

Next, we computed wall shear stress (WSS) on the surface of the TAA at this Reynolds number, to analyze the effect of the slow moving blood flow in the recirculation regions on the wall shear stress. The methodology presented by Mark et al. [42] is used to interpolate and compute the values onto the surface mesh from the Eulerian mesh. Figure 4.8 shows the normalized mean WSS plotted on the surface of the TAA in two different views in frames (a) and (b). Average value obtained from the circumferential average at the inlet of the domain is used for normalizing the WSS throughout the TAA. We can see from this figure that, a peak WSS of 2.0 is noted in regions on the three separating arteries from the aortic arch. The WSS values drop to less than 50% on the inner and outer walls of the aneurysm region.

4.3.2 Re = 3727

The same 100 block configuration as shown in Figure 4.6(a) is used for the peak Reynolds number simulation as well, but with a refined mesh in each block with $25 \times 25 \times 85$ points, making it a total resolution of 5.3 million mesh points. The simulation is run on 100 processors, for a non-dimensional time of 200 and turbulent statistics are collected over the last 100. A steady inflow is applied at the inlet of the domain, but unlike the average Reynolds number case, the flow is found to be unsteady

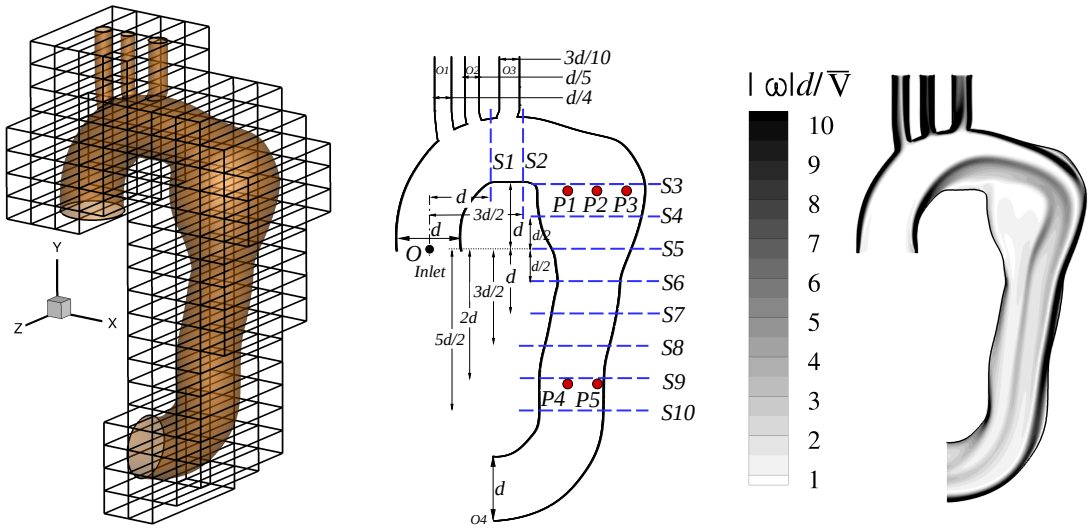

(a) (b) (c)

Figure 4.6. (a) Decomposition of the TAA into 100 multiblocks. (b) Schematic of TAA on the bisecting xy-plane at $z = 0$ depicting the sampling lines $S1$ through $S10$ and sampling points $P1$ through $P5$ in the aneurysm and descending aorta regions where data is collected. The coordinates of indicated points are $O(0, 0)$, $P1(2.2d, 0.9d)$, $P2(2.6d, 0.9d)$, $P3(3.1d, 0.9d)$, $P4(2.2d, -2.1d)$ and $P5(2.6d, -2.1d)$. (c) Contours of non-dimensional vorticity magnitude ($|\omega|d/\overline{V}$) on the bisecting xy-plane at $z = 0$, for steady inflow in the TAA at a Reynolds number of 910.

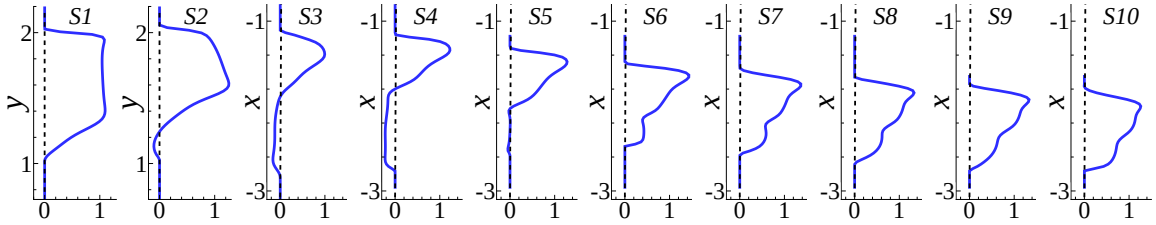

Figure 4.7. Mean axial velocity profiles (locations $S1$ and $S2$ show $< \overline{u} > /\overline{V}$, all other locations show $- < \overline{v} > /\overline{V}$) on indicated lines $S1$ through $S10$ for steady inflow in the TAA at a Reynolds number of 910.

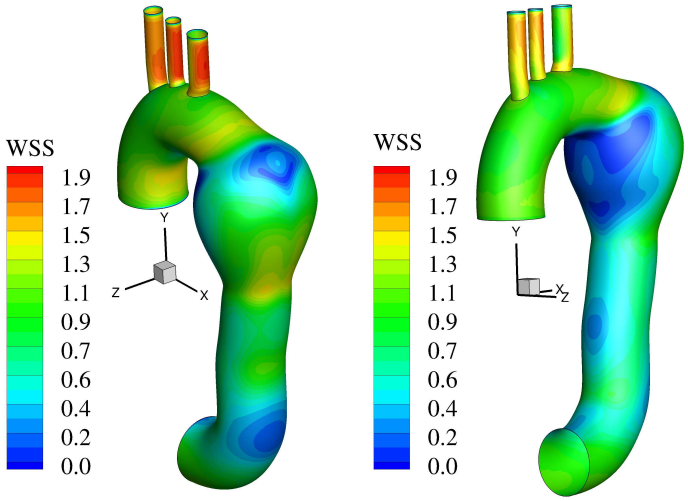

(a) (b)

Figure 4.8. Contours of normalized mean WSS for a steady inflow at a Reynolds number of 910. The average WSS at the inlet is used for normalization. Frames (a) and (b) show the plot from two different views.

in the aneurysm and descending aorta regions. The time history of normalized y-component of velocity fluctuations ($v\prime/\overline{V}$) at five different probe locations $P1$ through $P5$ noted in Figure 4.6(b), is shown in Figure 4.9(a), which indicates the unsteady flow field in the descending aorta region. The time history of normalized v_{rms} values at the probe locations is shown in Figure 4.9(b), which clearly shows the convergence of the root mean square (rms) quantities over the simulation time considered.

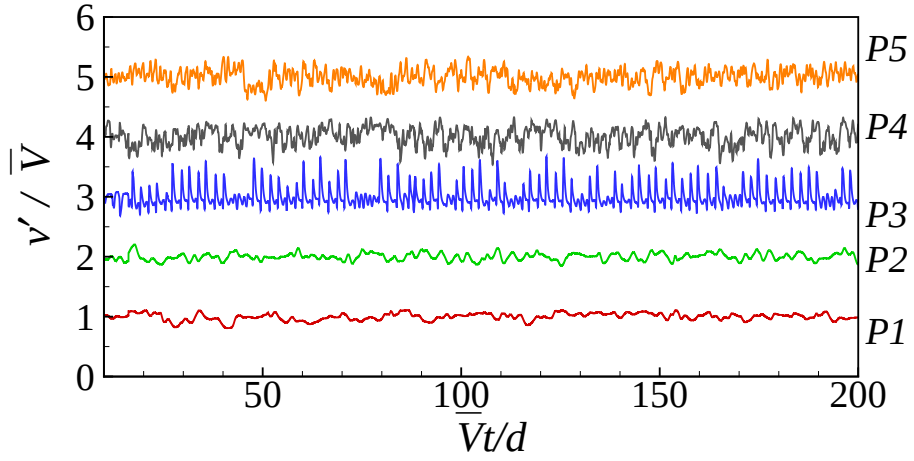

(a)

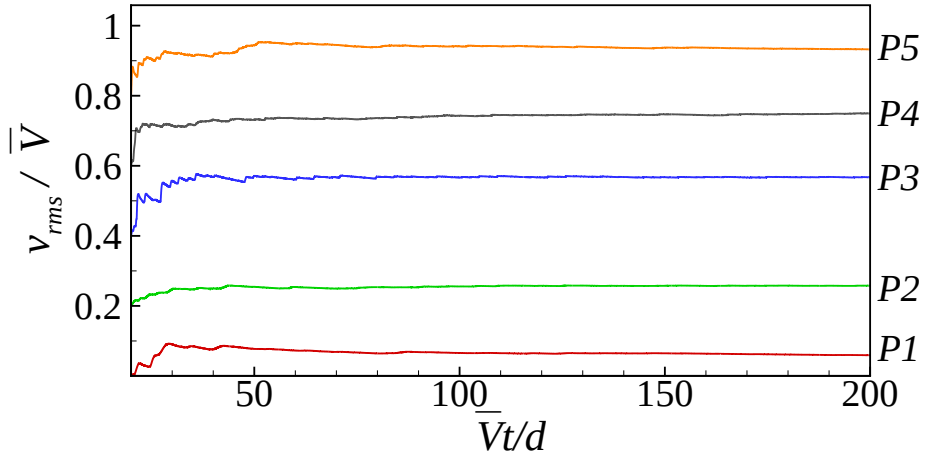

(b)

Figure 4.9. (a) Time history of $v'/\overline{V}$ at locations $P1$ through $P5$. The $v'/\overline{V}$ value at each station is offset by 1 unit. (b) Time history of $v_{rms}/\overline{V}$ at locations $P1$ through $P5$. The $v_{rms}/\overline{V}$ value at each location is offset by 0.2 units.

In order to identify the disturbed flow field occurring in the aneurysm region and extending through the descending aorta, we plot the normalized mean vorticity magnitude contours on the central xy-plane at $z = 0$ in Figure 4.10(a). From this figure, we can see that, the wall boundary layer at the outer wall rolls up similar to a mixing layer and curves down in the aneurysm region. The wall boundary layer at the inner wall, separates similar to the average Reynolds number case, but in this case additionally produces a disturbed flow field in the aneurysm and descending aorta regions as observed from the figure. To visualize the coherent structures forming in this disturbed flow field, the iso-surfaces of λ_2 [56] corresponding to a value of -2.0, colored by normalized mean vorticity magnitude are plotted in Figure 4.10(b). Long vortical structures emanating from the aneurysm and extending towards the distal end with length of the order of $3d$ are noted from this figure. The clinical significance of these long vortical structures needs to be understood yet.

The mean velocity and turbulent statistics in the TAA are analyzed here, similar to the average Reynolds number case by considering the data extracted on the lines $S1$ through $S10$. The normalized mean velocity profiles are shown in Figure 4.11(a) at the indicated locations. The $\overline{u}/\overline{V}$ velocity at the locations $S1$ shows a flat profiles with no re-circulation, whereas at the location $S2$ a small retrograde flow is found from the profile. Similar to the average Reynolds number case, the profiles at the stations $S3, S4$ and $S5$ capture a retrograde flow, extending close to 50% of the local diameter at the stations $S3$ and $S4$, while at $S5$ the retrograde velocity is only over 25% of the local diameter. The peak values of the retrograde velocity at $S3$ and $S4$ are approximately 25% of $\overline{V}$, whereas at the station $S5$ the retrograde velocity has a peak of 11% of $\overline{V}$, which is twice more than the value found in the average Reynolds number case. Further downstream, beginning with the location $S6$, no retrograde flow is found in the profiles extracted. The turbulent statistics, $u_{rms}/\overline{V}$, $v_{rms}/\overline{V}$, $w_{rms}/\overline{V}$ and normalized turbulent kinetic energy ($k/\overline{V}^2$) are shown at indicated locations in Figure 4.11(b), (c), (d) and (e) respectively. The unsteady and the turbulence levels are not present upstream of the aneurysm, in the regions of aortic arch as seen

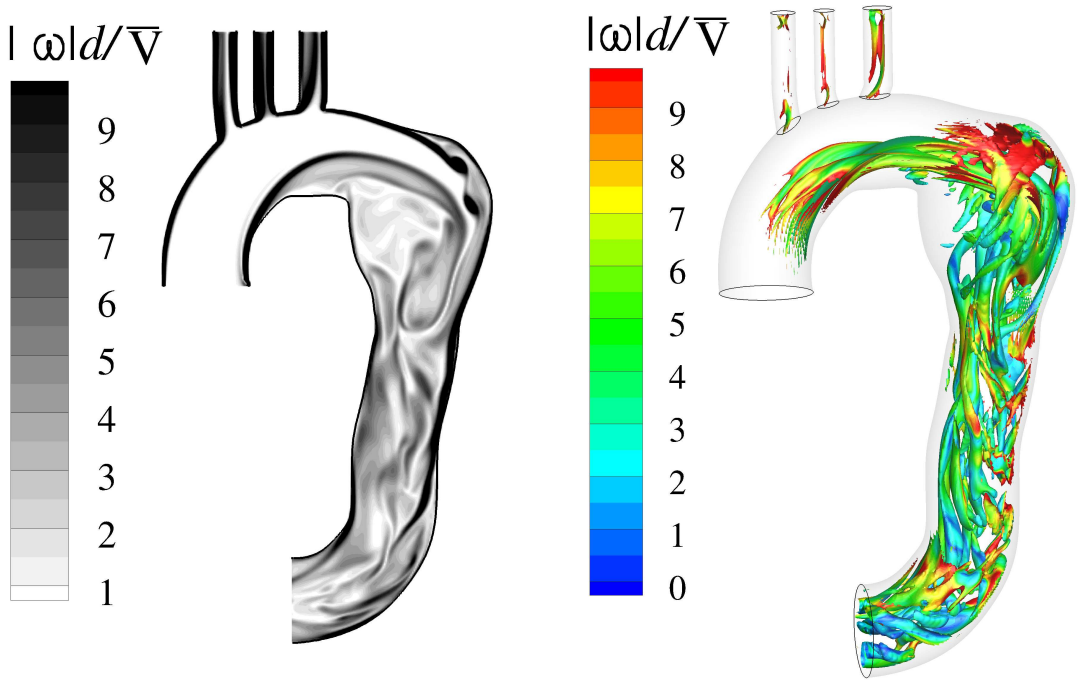

(a) (b)

Figure 4.10. (a) Instantaneous contours of non-dimensional vorticity magnitude on the bisecting xy-plane, at $z = 0$. (b) Instantaneous iso-surface of $\lambda_2 = -2.0$ colored by non-dimensional vorticity magnitude.

from the locations $S1$ and $S2$ for any of the turbulent statistics. From the extracted profiles, $u_{rms}/\overline{V}$ values show a peak value of 30% at the location $S3$ and decreasing as we move downstream, reaching a value close to 25% at the locations $S4$ through $S7$ and further to 20% at the locations $S8$ through $S10$. The $v_{rms}/\overline{V}$ profiles also show a similar pattern with peak values reaching close to 25% at the locations $S3$ and $S4$ and decreasing as we move downstream to values close to 15% at the locations $S5$ through $S10$. The $w_{rms}/\overline{V}$ profiles show close to constant values with peak values reaching to 14% at the location $S3$ and decreasing only to 12% at the location $S10$. The turbulent kinetic energy profiles shown in Figure 4.11(e), also shows a decreasing trend as we traverse from $S3$ towards the distal end at $S10$. The peak turbulent kinetic energy $\langle k/\overline{V}^2 \rangle$ at the location $S3$ reaches a value of 8%, decreasing to a value of 3% at the location $S10$.

In order to characterize the flow in TAA, the energy spectrum of the of the $y-$component of the velocity fluctuations (v') is computed at several points ($P1$ through $P5$, shown in Figure 4.6(b)) in the aneurysm and in the descending aorta regions. The energy spectra obtained are shown in Figure 4.12. The frequency spectra $E_{22}(S)$ are computed by using Welch's method [65], with no overlap. The energy spectra are plotted as a function of the Strouhal number $S = fd/\overline{V}$ where f is the frequency of eddy motions at the probe location. The lines corresponding to $S^{-5/3}$ and S^{-7} have also been shown in the figure. In turbulent flows, the $S^{-5/3}$ variation in the energy spectrum is associated with the energy transfer from low wave number to high wave numbers and is dominated by inertial transfer [66]. This region is also known as inertial subrange and the process of transfer of energy is known as spectral energy cascade. The variation of S^{-7} is a characteristic of dissipation range in which viscous forces dominate [67]. From Figure 4.12, we can see that points $P1$, $P2$, $P4$ and $P5$ seem to have a broader range of frequencies when compared with probe $P3$, for inertial subrange, whereas at higher frequencies all the probes record viscous dissipation.

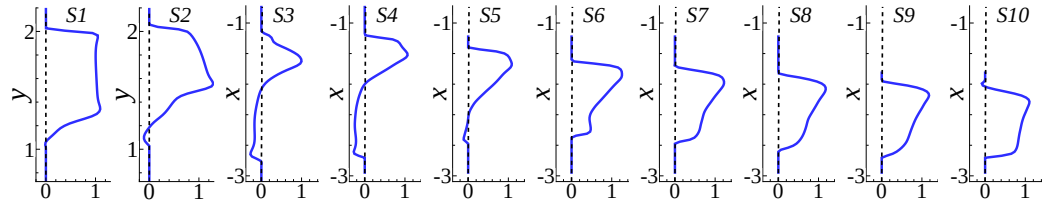

(a) Mean axial velocity profiles (locations $S1$ and $S2$ show $< \overline{u} > /\overline{V}$, all other locations show $- < \overline{v} > /\overline{V}$).

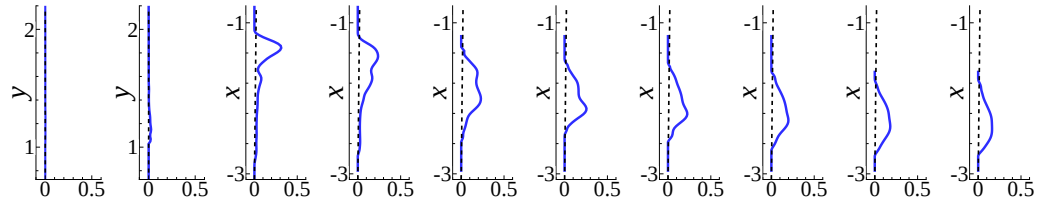

(b) $u_{rms}/\overline{V}$

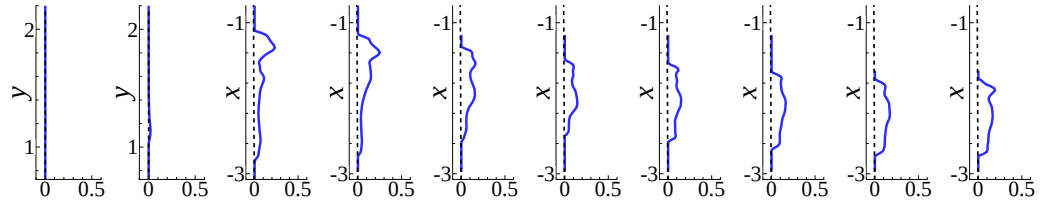

(c) $v_{rms}/\overline{V}$

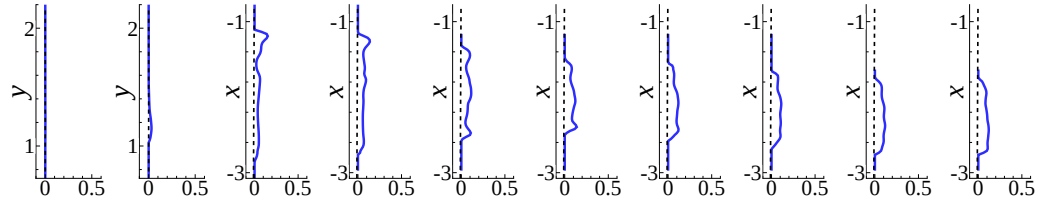

(d) $w_{rms}/\overline{V}$

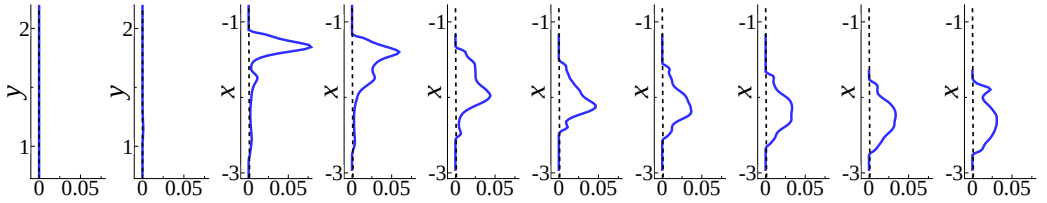

(e) $k/\overline{V}^2$

Figure 4.11. Steady inflow in the TAA at a Reynolds number of 3727. (a) Mean axial velocity profiles (locations $S1$ and $S2$ show $< \overline{u} > /\overline{V}$, all other locations show $- < \overline{v} > /\overline{V}$) (b) $u_{rms}/\overline{V}$ profiles (c) $v_{rms}/\overline{V}$ profiles (d) $w_{rms}/\overline{V}$ profiles (e) Normalized turbulent kinetic energy $\langle k/\overline{V}^2 \rangle$ profiles on indicated lines $S1$ through $S10$.

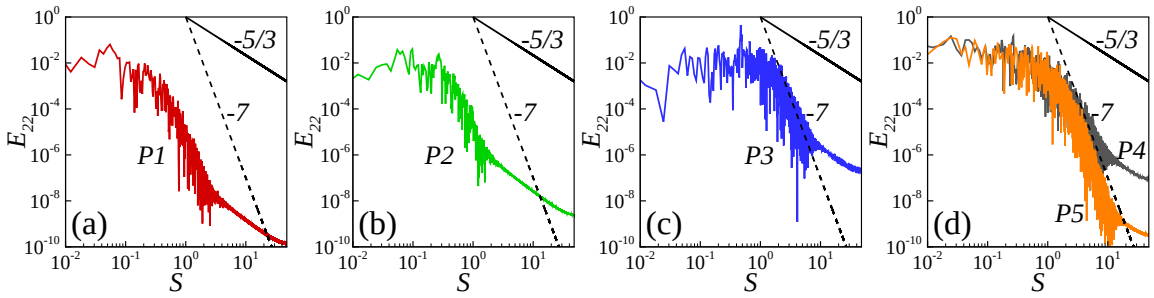

Figure 4.12. Frequency spectra corresponding to the velocity fluctuations (v'). The letter adjacent to each of the curves identifies the point where the signal is measured. The solid and the dashed straight lines correspond to $S^{-5/3}$ and S^{-7} respectively as marked. (a) Spectra at location $P1$ (b) Spectra at location $P2$ (c) Spectra at location $P3$ (d) Spectra at locations $P4$ and $P5$. The locations of the points $P1$ through $P5$ are shown in Figure 4.6(b).

Finally, we compute the normalized WSS similar to the average Reynolds number case and is shown in Figure 4.13 in two different views in frames (a) and (b). As we can see from this figure, the maximum WSS is 6 times the average inlet value and occurs in the distal end of the aorta. The inner and outer walls of the aneurysm region and few portions of descending aorta continue to show smaller values of WSS of the order of 0.5, similar to the average Reynolds number case, but the peak value of WSS obtained in this case is 3 times larger than the one obtained in the average Reynolds number case.

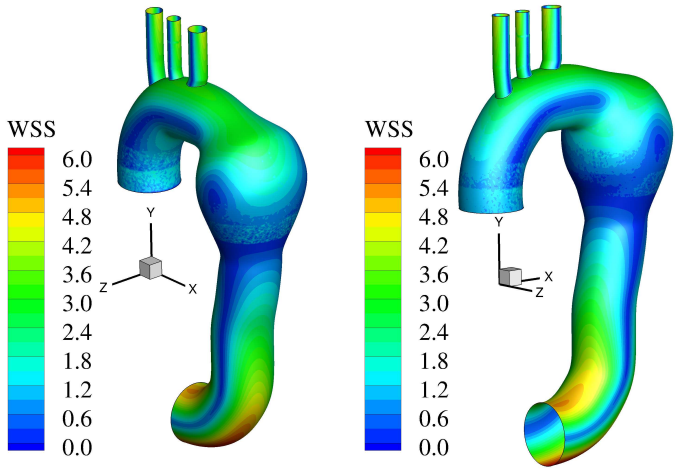

(a) (b)

Figure 4.13. Contours of normalized mean wall shear stress (WSS) for a steady inflow at a Reynolds number of 3727. The average wall shear stress at the inlet is used for normalization. Frames (a) and (b) show the plot from two different views.

4.4 Pulsatile Inflow in a Thoracic Aorta

4.4.1 Geometry and Boundary Conditions

The geometry of the TAA and the thoracic aorta with a stent graft (TASG) used in the present study are shown together with their multiblock decomposition into 325

and 330 uniform blocks respectively in Figure 4.14. The inlets and outlets to the aorta are also shown marked in both the frames. From frame (a) of this figure we can note that post aortic arch there is an aneurysm that formed whereas in frame (b) this aneurysm is totally excluded by making use of a stent graft. The TAA geometry is decomposed into 325 uniform mesh blocks with a grid size of $15 \times 15 \times 90$ in x, y, and z directions respectively, in each block making a total of 6.58 million mesh points, whereas the TASG geometry is decomposed into 330 uniform mesh blocks with a mesh size of $16 \times 16 \times 85$ with a total mesh resolution of 7.18 million mesh points. Several lines and point probes are extracted on the $z = 0$ plane to study the flow dynamics evolving in the TAA and TASG geometries. These are identified in frames (a) and (b) of Figure 4.15 for TAA and TASG respectively.

The velocity profiles used at the Inlet and the three supra-outlets are taken from the measured values used by Lantz et al. [11] in their work and is shown in Figure 4.16. This figure also depicts the corresponding acceleration curve to make it easy to locate the several sampling points ($P1$ through $P6$) which are used for ensemble averaging or a phase locked averaging of the quantities. At the outlet of the domain a homogeneous Neumann boundary condition on the velocity is used. Homogeneous Neumann boundary condition on the pressure is applied at all the inlets and outlets and a Dirichlet value is set on the front and back faces in z direction of the bounding box where the geometry under consideration is in the interior so that the level of the pressure is fixed. The bulk velocity at the inlet $\overline{V}$ is used as the velocity scale and the inlet diameter d is used as the length scale to define a peak Reynolds number as $Re = \overline{V}d/\nu$. The peak Reynolds number is equal to 3727 in the present work.

4.4.2 Assumptions

There are certain assumptions made in the present study and a summary of these together with justifications where applicable are presented. The fluid is assumed to be Newtonian with a constant value of viscosity as blood flow in large arteries

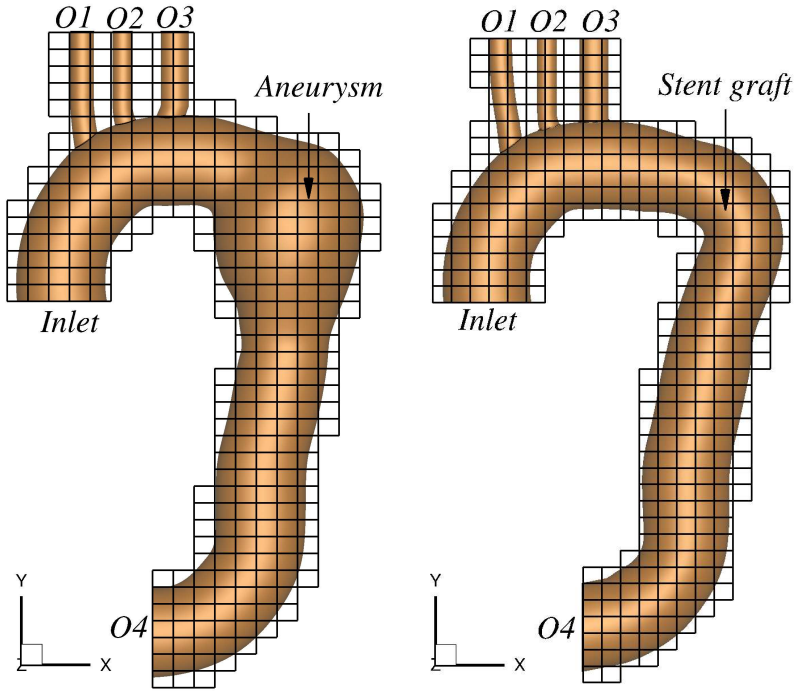

(a) (b)

Figure 4.14. Geometries of the TAA and TASG used in the present study. The inlet to the thoracic aorta, the outlets $O1$, $O2$ and $O3$ carrying blood to brachiocephalic artery, left common carotid artery, and left subclavian artery, respectively and the largest outlet $O4$ which carries blood to abdominal portion of the aorta are shown marked. The aneurysm region and the stent graft that totally excludes blood flow to the aneurysm region are also shown marked in the frames. (a) Decomposition of the TAA geometry into 325 uniform blocks (b) Decomposition of the TASG geometry into 330 uniform blocks.

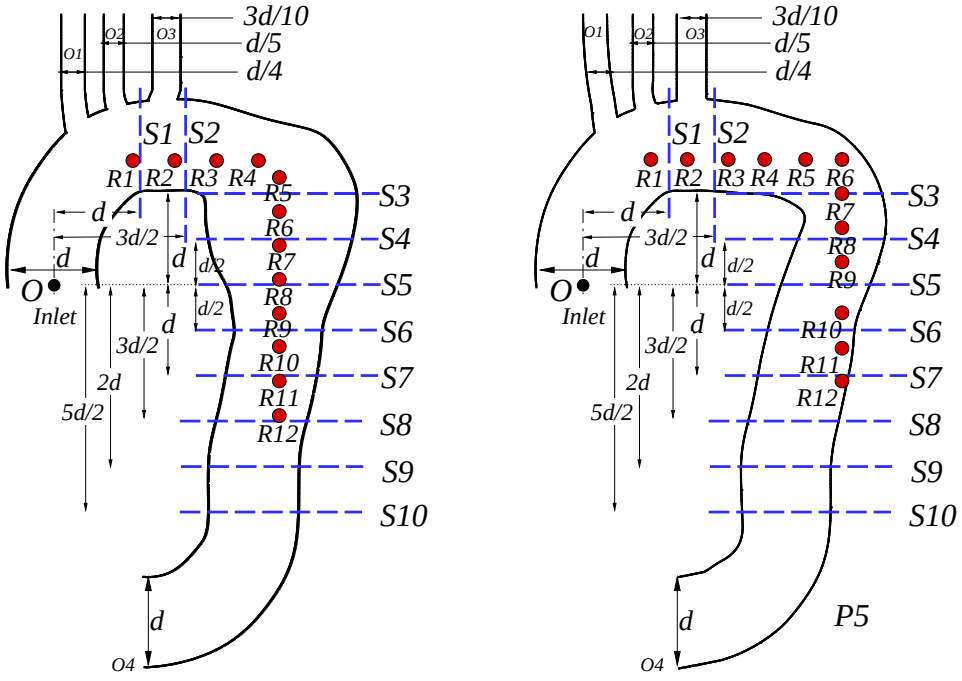

(a) (b)

Figure 4.15. (a) Spatial sampling locations for the TAA geometry. Several point probes R1 through R12, and lines S1 through S10 are extracted on the central $z = 0$ plane to investigate the flow dynamics. The locations of the point probes are R1 $(-3.6d, 1.36d)$, R2 $(-3.1d, 1.36d)$, R3 $(-2.7d, 1.36d)$, R4 $(-2.2d, 1.36d)$, R5 $(-2.0d, 1.18d)$, R6 $(-2.0d, 0.80d)$, R7 $(-2.0d, 0.43d)$, R8 $(-2.0d, 0.06d)$, R9 $(-2.0d, -0.32d)$, R10 $(-2.0d, -0.70d)$, R11 $(-2.0d, -1.1d)$ and R12 $(-2.0d, -1.44d)$. (b) Spatial sampling locations for the TASG geometry. Several point probes R1 through R12, and lines S1 through S10 are extracted on the central $z = 0$ plane to investigate the flow dynamics. The locations of the point probes are R1 $(-3.7d, 1.38d)$, R2 $(-3.3d, 1.38d)$, R3 $(-2.85d, 1.38d)$, R4 $(-2.45d, 1.38d)$, R5 $(-2.0d, 1.38d)$, R6 $(-1.6d, 1.38d)$, R7 $(-1.6d, 1.0d)$, R8 $(-1.6d, 0.60d)$, R9 $(-1.6d, 0.20d)$, R10 $(-1.6d, -0.30d)$, R11 $(-1.6d, -0.70d)$ and R12 $(-1.6d, -1.1d)$.

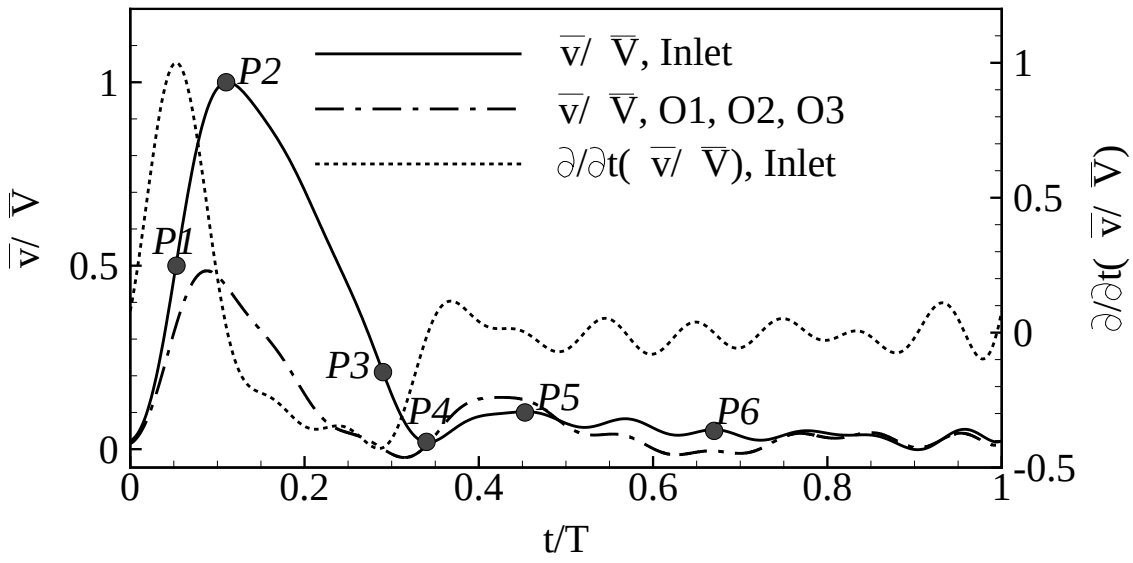

Figure 4.16. Pulsatile velocity profiles at the inlet to the ascending aorta and at the outlets to the supra-arteries (O1, O2 and O3) and the corresponding acceleration profile for the pulsating inflow considered. Several points are marked on the velocity curve for the purpose of phase locked or ensemble averaging. The point $P1$ corresponds to the point of maximum acceleration, $P2$ is the maximum velocity, $P3$ is maximum deceleration, $P4$ is end of systole, $P5$ is the point of second maximum in velocity and $P6$ corresponds to the point of mid diastole.

is previously shown to be having negligible non-Newtonian effects [3]. The walls of the arteries are modeled as rigid walls and with a no-slip, impermeable boundary condition. The rigid assumption of the walls is justified as they become stiff in the case of formation of an aneurysm and the stent grafts can be considered rigid from their present application point of view. Further, it is assumed that the when stent graft is used to exclude the aneurysm region it totally excludes blood flow access to the aneurysm region thereby creating a perfect seal between the walls of the aorta and the stent graft. The thickness of the stent graft is not modeled in the present simulations therefore it is assumed that the internal diameter of the aorta and the stent graft are equal. The geometries used in the present study are generated from patient specific image scan data after a clean up of the raw data. The distal end of both the geometries (TAA and TASG) show an additional bend to the left, this artificial bend introduced is supposed to create a worse case scenario in terms of forces acting on the stent graft.

4.4.3 Pulsatile Inflow in a Thoracic Aortic Aneurysm (TAA)

In this section, pulsatile inflow in TAA is investigated. Several point probes are used along the aortic geometry to record instantaneous time histories as the simulation advanced. Time histories of normalized axial velocity ($\overline{u}/\overline{V}$ or $\overline{v}/\overline{V}$) are monitored and are shown in frame (a) of Figure 4.17. In the present work the first 20 cycles are considered as the initial flow through time and are discarded from the point of view of statistical collection. Only the last 35 pulsatile cycles are used for collecting mean and turbulent statistics. The total number of pulsatile flow cycles simulated is in line with previous LES simulations in the literature [11], however, in the present case the first 20 cycles are discarded owing to the flow development over the entire aortic geometry whereas only first 5 cycles are discarded in Lantz et al. [11]. In frame (b) of Figure 4.17 the corresponding phase averaged velocity profiles are shown over one pulsatile cycle. From frame (b), we note that the flow at these probe location

undergoes flow reversal at locations $R1$ and $R2$, whereas locations $R3$ through $R12$ show no evidence of axial flow reversal. Low frequency oscillations with a time period of $O(10T)$ can be noticed in frame (a) at several probe locations, these are thought of as cycle-to-cycle variation. Part of the flow that is entering the aorta through the inlet, leaves the domain through the supra-arteries, brachiocephalic trunk, left common carotid artery and left subclavian arteries situated at the top of the aortic arch. This is the reason for the decrease in magnitude of peak axial velocities in the distal portions of the aorta as recorded by probes $R7$ through $R12$.

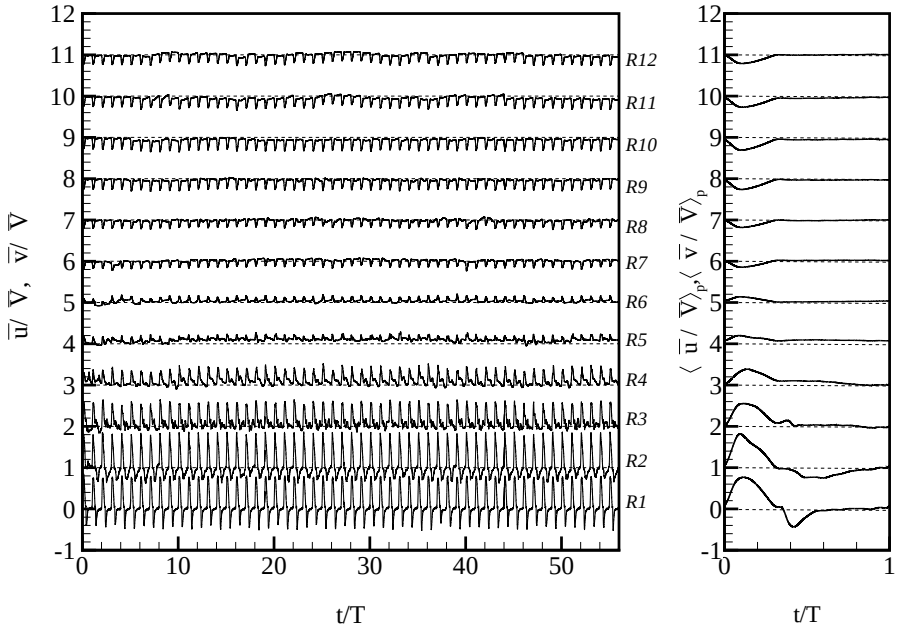

(a) (b)

Figure 4.17. (a) Time history of 55 cycles of normalized axial velocity (R1 through R6 displaying $\overline{u}/\overline{V}$, whereas R7 through R12 displaying $\overline{v}/\overline{V}$), at several locations R1 through R12 for pulsatile flow through the TAA geometry. (b) Normalized ensemble-averaged axial velocity (R1 through R6 displaying $\langle \overline{u}/\overline{V} \rangle_p$, whereas R7 through R12 displaying $\langle \overline{v}/\overline{V} \rangle_p$), at indicated locations.

Mean and Turbulence Profiles

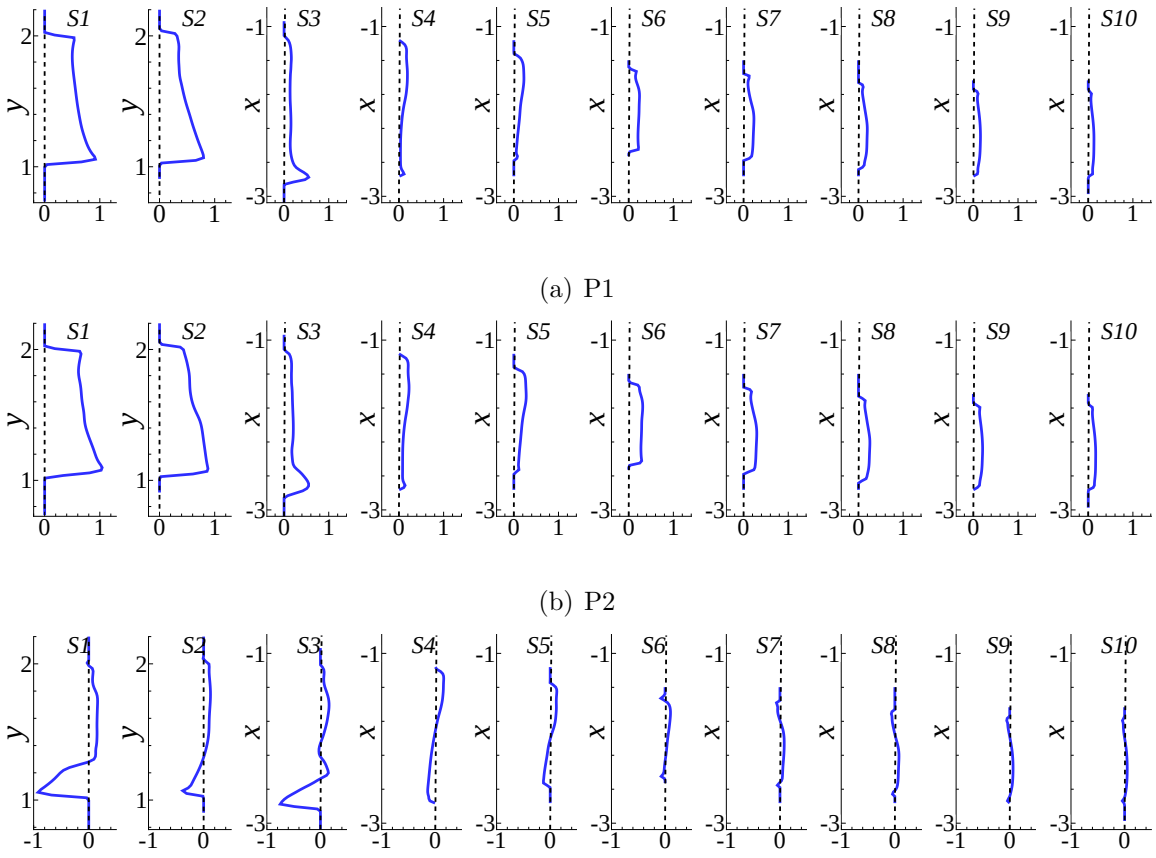

(a) P1

(b) P2

(c) P3

Figure 4.18. Sequence of ensemble-averaged normalized axial velocity profiles (locations S1 and S2 show $\langle \overline{u}/\overline{V} \rangle_p$, all other locations show $-\langle \overline{v}/\overline{V} \rangle_p$) at the indicated time instants, for pulsatile inflow through the TAA geometry.

The phase averaged normalized axial velocity profiles for pulsatile inflow in TAA are shown in Figure 4.18 at several locations ($R1$ through $R12$) along the aorta and at the indicated phase instants. The profiles are extracted on vertical lines on the central plane $z = 0$ in the ascending aorta ($S1$ and $S2$), and on the horizontal lines on the central plane $z = 0$ in the descending aorta ($S3$ through $S10$). Accordingly to best represent the axial velocities on the central plane, $\langle \overline{u}/\overline{V} \rangle_p$ are plotted at

locations $S1$ and $S2$ whereas $-\langle\overline{v}/\overline{V}\rangle_p$ are plotted at all other locations. As we can see from this figure during acceleration phase as indicated by samples at $P1$ and $P2$ forward axial flow can be noticed at all the locations. At $P3$ which is the maximum deceleration point in the pulsatile flow cycle we notice reverse flow almost at all of the locations with varying extents depending on the location. At other sampling points on the pulsatile profile we see similar reverse flow patterns, however, with decreased intensity and are not shown here.

To investigate the overall turbulence levels in the phase averaging sense as defined before, we extracted turbulent kinetic energy profiles (which sums up the collective contribution of all of the root mean square quantities) at the same spatial locations and time instants as was considered in the mean axial velocities before. The variation of normalized phase averaged turbulent kinetic energy (tke) profiles are shown in Figure 4.19 at the indicated spatial and temporal samples. Interestingly, the maximum tke values are obtained at the maximum deceleration time instant $P3$. The peak values in tke at the maximum velocity point $P2$ are smaller than those obtained at the maximum acceleration and those obtained at maximum deceleration. Peak values of tke decrease as one travels along the aorta towards the distal end. Maximum values in tke are observed in the aortic arch region at any given time instant. A maximum of around 1% peak values for tke are observed.

Coherent Structures

The flow shows in Figure 4.18 several recirculation zones as observed before from the mean axial velocity profiles at the maximum deceleration point $P3$. In order to visualize these secondary recirculation patterns together with the associated coherent vortical structures we used the λ_2 criterion coined by Jeong & Hussain [56]. The vorticity magnitude contours on the central $z = 0$ plane are also used to further understand the complex blood flow dynamics arising in the aorta. The nondimensional vorticity magnitude contours are shown in Figure 4.20 at the indicated instants. We

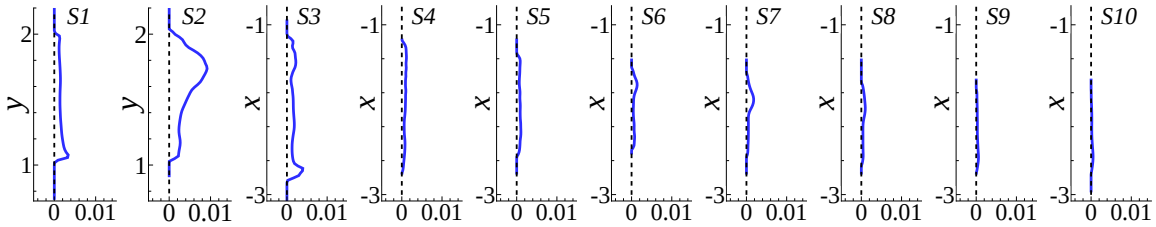

(a) P1

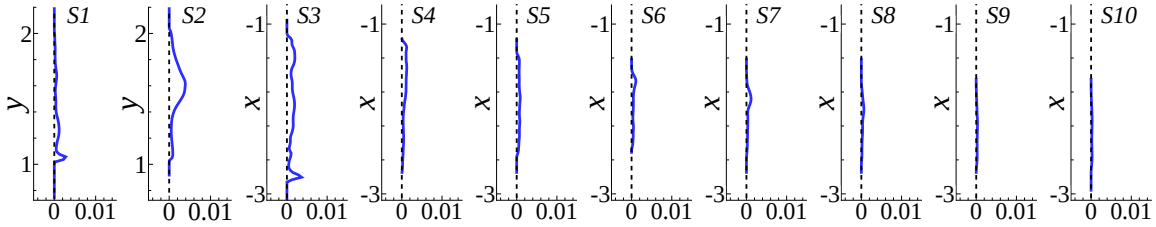

(b) P2

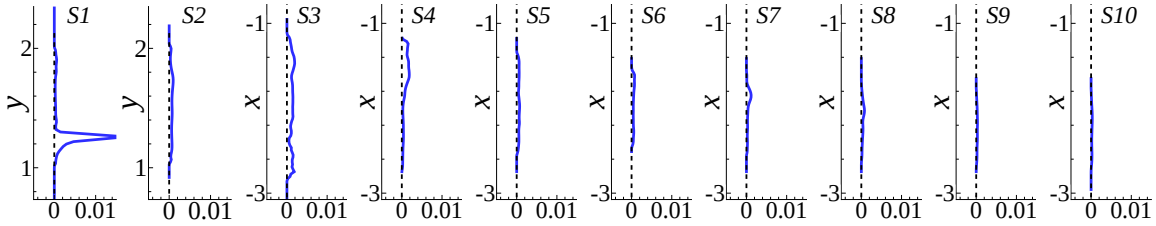

(c) P3

Figure 4.19. Sequence of ensemble-averaged normalized turbulent kinetic energy $\langle k \rangle_p / \overline{V}^2$ profiles at the indicated time instants, for pulsatile inflow through the TAA geometry.

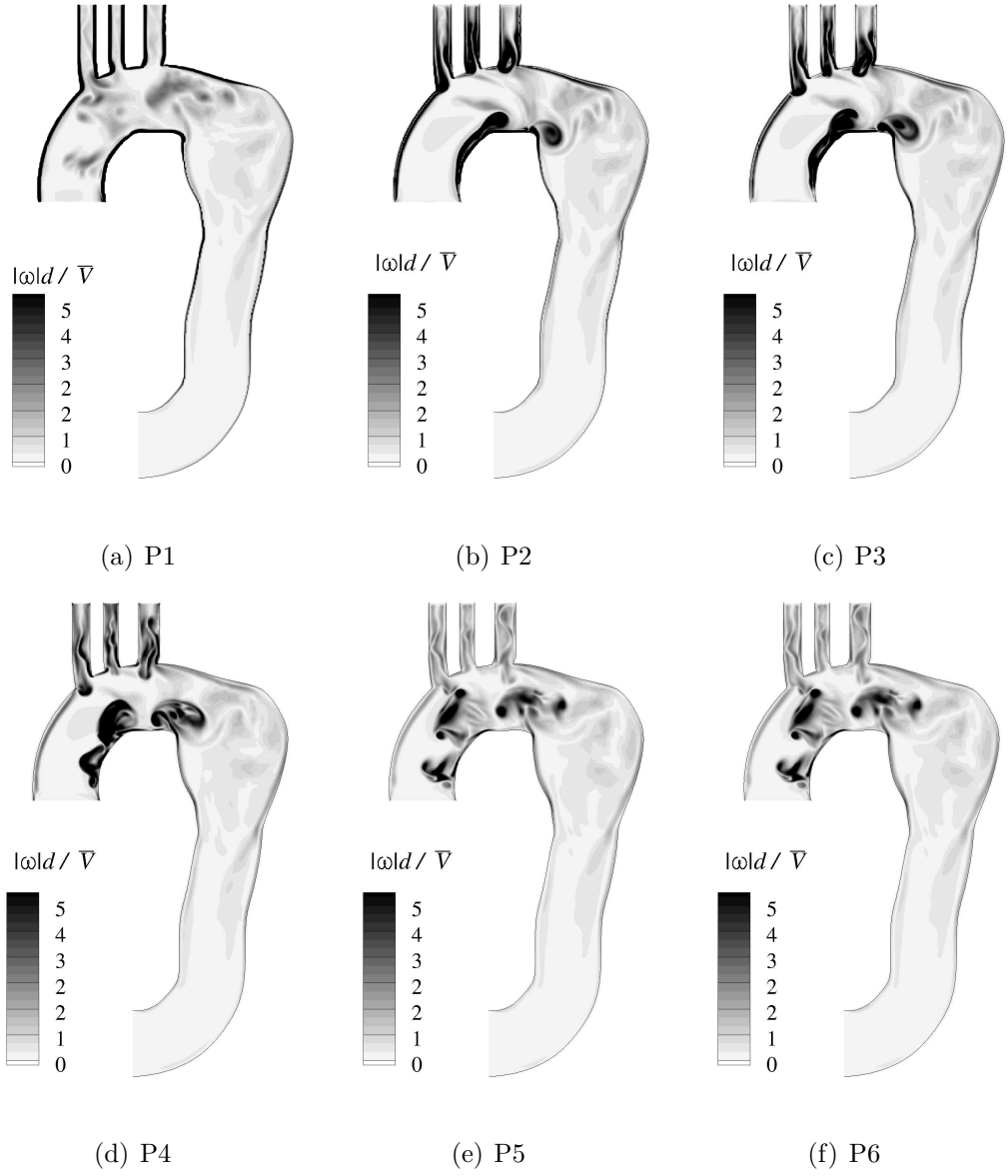

(a) P1 (b) P2 (c) P3

(d) P4 (e) P5 (f) P6

Figure 4.20. Sequence of ensemble-averaged contours of vorticity magnitude, normalized by $\overline{V}/d$, for pulsatile inflow through the TAA geometry.

note from this figure that peak vorticity values are present in the ascending aorta, aortic arch and in the supra-arteries. During the acceleration phase vorticity production takes place and two distinct high vorticity regions can be located close to the inner wall in the aortic arch and also shear layer type vorticity regions can be located in the supra-arteries at time instant $P2$. During the deceleration phase and further into the diastole stroke the the vorticity regions form into three distinct regions and separate away from the inner wall, first one traveling towards the inlet of the domain, the second one traveling towards the brachiocephalic trunk and the last one traveling towards center of the aortic arch below the left subclavian artery. To further understand the complex flow dynamics, we educe the vortical structures using the λ_2 criterion [56] as shown in Figure 4.21. From this figure we can note that ring like vortical structures are present in the ascending and aortic arch regions at instants $P1$ and $P2$. Further, the aneurysm region is composed of elongated vortical structures that originate close to the inner wall of the aortic arch and extend towards the outer wall of the aneurysm region. Interestingly the vortical structures are less populated towards the inner wall region in the aneurysm region. Because of the low velocity during the diastole the vortical structures are hard to differentiate between time instants $P3$ to $P6$.

Turbulence Energy Spectra

The pulsatile flow in TAA is identified in the previous sections to be composed of coherent structures and disturbed flow. To further quantify the range of scales occurring in these types of flows we used single point frequency spectra. The turbulent energy spectra obtained from the fluctuations quantities are shown in Figure 4.22. Frames (a) and (b) denote $E_{u'',u''}$ at locations R1 and R3, whereas frames (c) and (D) denote $E_{v'',v''}$ at locations R9 and R12. The frequency spectra $E_{u'',u''}$ and $E_{v'',v''}$ are computed using the method of Welch [65]. The data sampling is performed at a rate of 1kHz which corresponds to a Nyquist frequency of 500Hz. Along with the

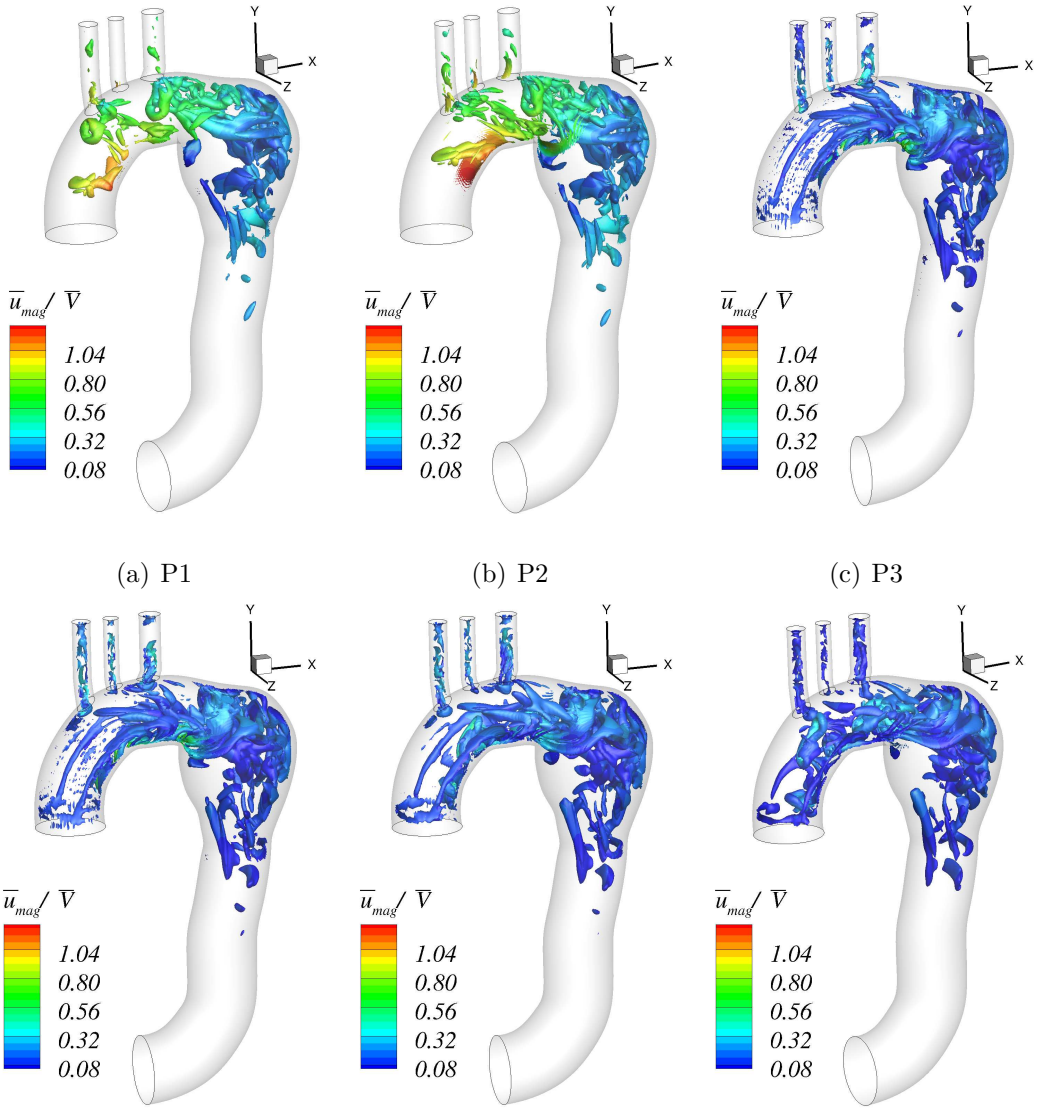

(a) P1 (b) P2 (c) P3

(d) P4 (e) P5 (f) P6

Figure 4.21. Sequence of instantaneous iso-surfaces of $\lambda_2 = -0.1$, colored by normalized velocity magnitude ($\overline{u}_{mag}/\overline{V}$), for pulsatile inflow through the TAA geometry.

spectra, the lines corresponding to $S^{-5/3}$, $S^{-10/3}$ and S^{-7} are also shown, where S is the frequency. In turbulence theory the line $S^{-5/3}$ corresponds to inertial subrange where the eddy motions are determined by inertial effects and viscous effects are negligible [68]. A wide band of inertial subrange in the frequency spectra points to the presence of a turbulent flow in the flow under consideration [66]. The line corresponding to S^{-7} indicates frequencies that are in dissipation range, it means in this the turbulence energy decays because of viscous dissipation. Further, motivated by previous studies [13, 52, 69, 70] in which roll off of spectrum from $-5/3$ to $-10/3$ was observed at a particular frequency that was attributed to arterial murmur in stenotic flows is also shown to enable identification any such behavior. We note from frame (a) that the only a very small range of frequencies can be found that are parallel to $S^{-5/3}$ line, whereas a major portion after $S = 1$ becomes parallel to the viscous dissipation range identified by S^{-7}. However, in frame (b) for point R3 a clearly noticeable range of frequencies from $S = 0.1$ to $S = 2$ can be seen to be parallel to $S^{-5/3}$ and energy values at higher frequencies become parallel to the dissipation range S^{-7} similar to those obtained at point probe R1. The energy in the inertial subrange decreases further as we move down the descending aorta to locations R9 and R12 as indicated by very narrow range of bands parallel to $S^{-5/3}$ and most of the energy falls in the dissipation range S^{-7}. A narrow band of frequencies can be identified to be having energy content parallel to S^{-103} at locations R3 and R9 where the turbulent energy content shifts from the inertial subrange to the dissipation range.

Wall Shear Stress

Now we turn our attention to look at wall shear stresses which is an important parameter in the study of hemodynamics. Ensemble averaged, normalized wall shear stress, referred as skin friction coefficient ($C_f = 2\tau_w/\rho\overline{V}^2$), is shown in Figure 4.23. Maximum values of skin friction coefficient are observed close to inlet to the aorta and the values decay along the aorta as one travels from the inlet towards the distal

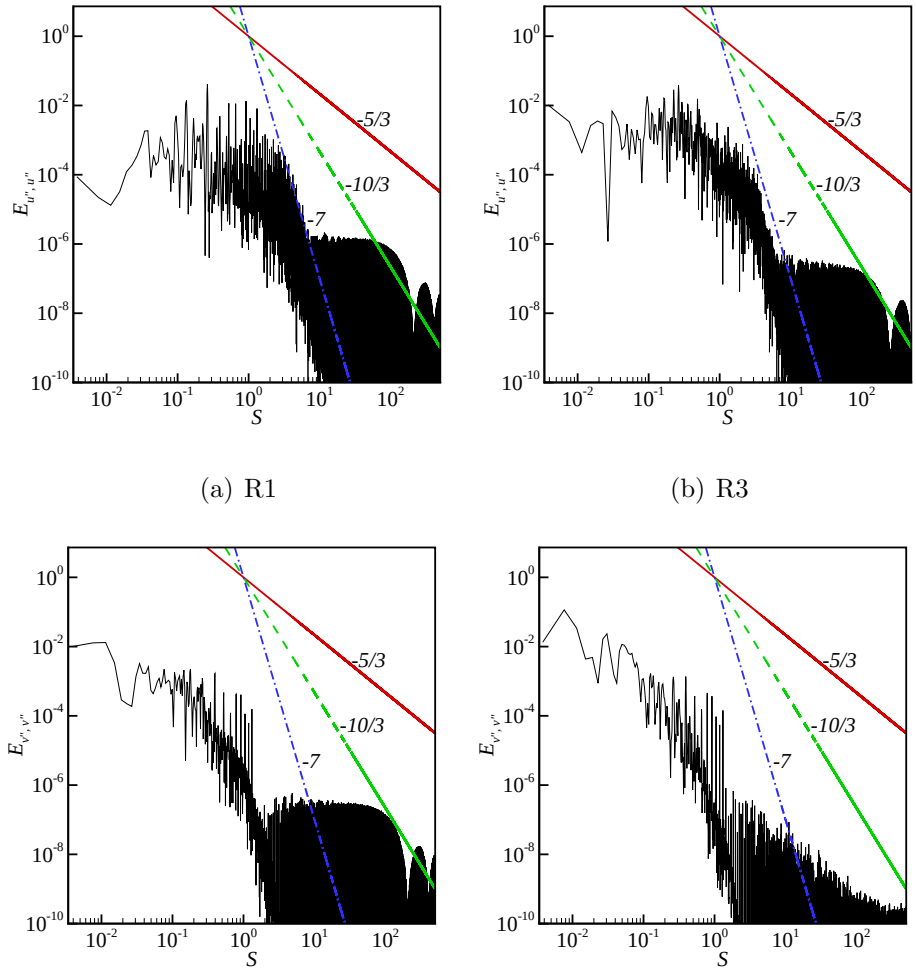

(a) R1

(b) R3

(c) R9

(d) R12

Figure 4.22. Energy spectrum associated with the stream-wise fluctuations (u'' for R1 and R3 and v'' for R9 and R12 for pulsatile inflow through TAA geometry at the indicated locations. Lines with slopes $-5/3$, $-10/3$ and -7 are also shown.

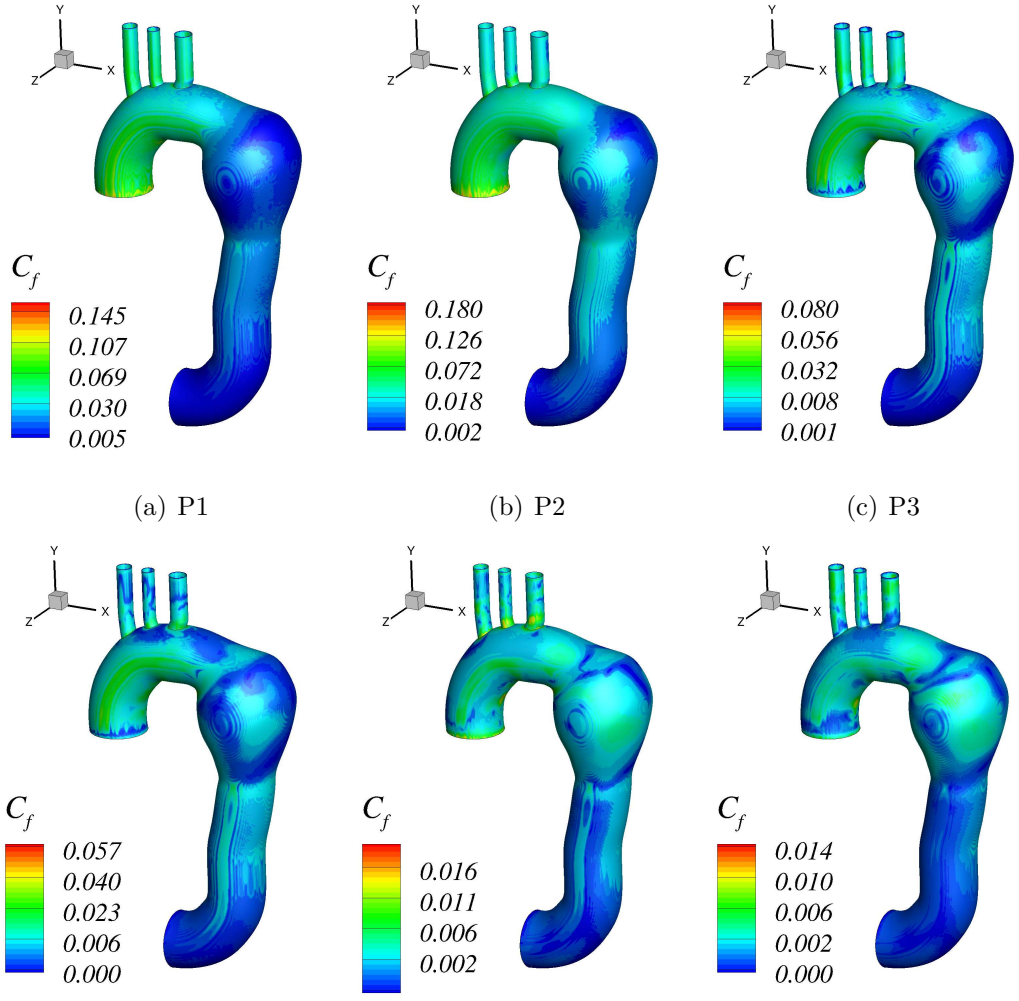

(a) P1 (b) P2 (c) P3

(d) P4 (e) P5 (f) P6

Figure 4.23. Sequence of ensemble-averaged contours of skin friction coefficient for pulsatile inflow through the TAA geometry. Note the contour levels shown are not the same for all frames.

end. The values in the supra-arteries are at the middle of the spectrum at any phase considered. The skin friction values seem to be closely correlated to the variation of inlet velocity profile. For example, maximum velocity point $P2$ also coincides with maximum skin friction values and there after the point $P1$ with next maximum velocity attaining the second peak values for skin friction coefficient and so on. At any given phase, the distal portion of the aorta is subjected middle to low values of the spectrum considered.

Magnitude of Spatial Wall Shear Stress Gradient (SWSSG)

Further to identify the regions that are susceptible for aneurysm formation we investigate the magnitude of spatial wall shear stress gradient (SWSSG). The contours of ensemble averaged SWSSG are shown at indicated phase instants in Figure 4.24. The minimum and maximum values of SWSSG are shown in the upper right corner in each of the frames and the contour levels are only plotted in a small range of the total range to enable easy location of the regions where the SWSSG is maximum. As we can see large values of SWSSG are obtained during the acceleration phase as noted at instants $P1$ and $P2$. Spatial distribution of large values of SWSSG is mainly concentrate in the ascending aorta region as well a small portion just ahead of the aneurysm. This small portion is consistently seen to attain locally large values at any given instant. Previous studies found that the location of high value of SWSSG can make the region predisposed for formation of an aneurysm. In this case, however, the aneurysm has already been formed but an understanding of SWSSG can provide insights into areas that are susceptible for an aneurysm formation.

4.4.4 Pulsatile Inflow in a Thoracic Aorta with Stent Graft (TASG)

Next, we investigate blood flow dynamics in a TAA with a stent graft implanted in it, a thoracic aorta with stent graft (TASG). Similar to the TAA simulation several point probes are used to monitor the evolution of the instantaneous velocities.

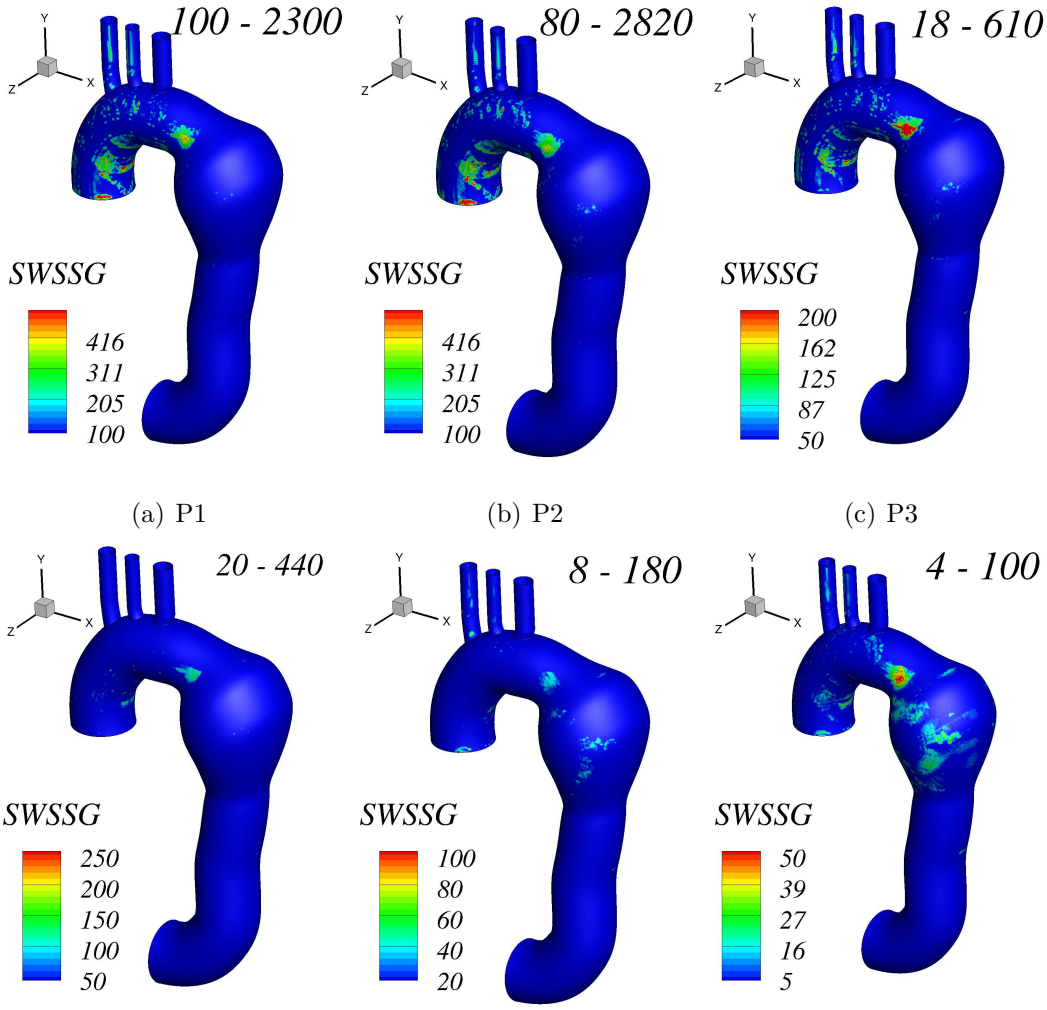

(a) P1 (b) P2 (c) P3

(d) P4 (e) P5 (f) P6

Figure 4.24. Sequence of ensemble averaged contours of spatial wall shear stress gradient for pulsatile inflow through the TAA geometry. Note the contour levels shown are not the same for all frames and the maximum and minimum values are shown on the upper right corner with only a small range of values used for the contour levels indicated.

Instantaneous normalized axial velocity profiles ($\overline{u}/\overline{V}$ at locations S1 through S6 and $\overline{v}/\overline{V}$ at locations S7 through S12) and their corresponding phase averaged profiles are shown in frames (a) and (b) respectively in Figure 4.25. From the profiles recorded by S1, S7 and S10 it can be clearly noticed that the time dependent profiles tend towards an asymptotic pattern and by end of $t/T = 20$ they seem to have attained a completely periodic state. This justifies our statistical averaging procedure to rely on only the last 35 periodic cycles discarding the first 20 cycles. From frame (b) of this figure it is observed that at points S7 and S8 the time dependent velocity profiles are more responsive to the diastole at the inlet showing time dependent reverse flow. Only locations S1, S7 and S8 show such a behavior, whereas locations R1 and R2 only showed such a behavior in the case of TAA.

Mean and Turbulence Profiles

The normalized phase averaged axial velocity profiles on the $z = 0$ plane are shown in Figure 4.26 at several locations at the indicated phase instants. From these profiles few observations similar to the flow in TAA can be made. For example, during the acceleration phase (P1 and P2) all the locations show forward flow. During the deceleration phase (P3) locations S1, S2, S4 and S5 show reverse flow as opposed to reverse flow occurring at most of the locations at the same time instant in a TAA. Interestingly, in the present case many locations in the distal end (S7 through S10) show forward flow at P3 time instant. The magnitude of axial velocities seem to be slightly higher at distal locations (S5 through S10) at time instant P2 when compared with TAA. This is attributed to the presence of stent graft providing a close to uniform cross sectional area thus restoring a healthy artery situation. The normalized phase averaged tke profiles are shown in Figure 4.27 at the indicated phase instants and on several locations. Similar to tke profiles in TAA, in the present case also tke decreases its magnitude as one travels from aortic arch towards descending aorta. The peak values of tke reached during P1 and P2 phases is only 0.5% unlike TAA in which the

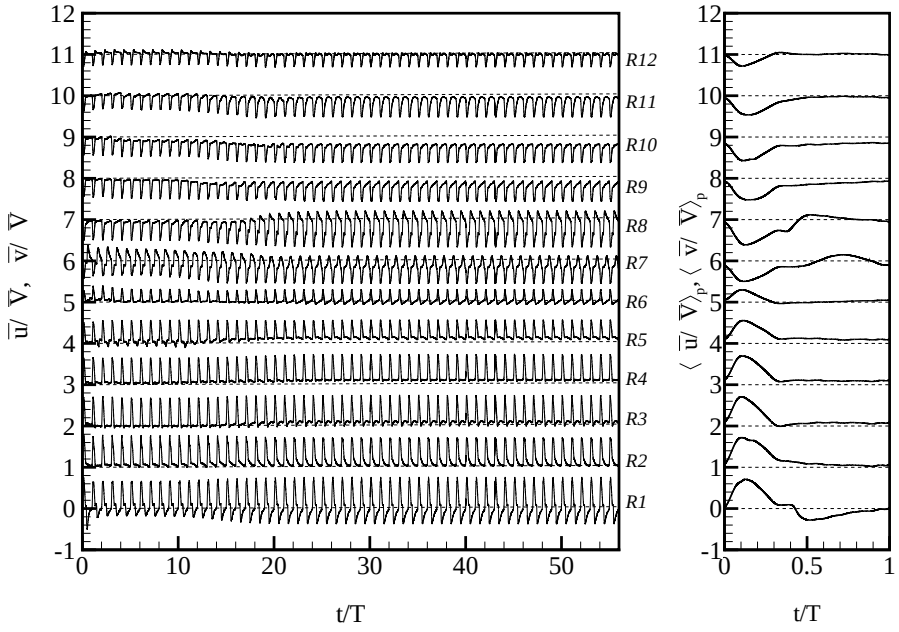

(a) (b)

Figure 4.25. (a) Time history of 55 cycles of normalized axial velocity (S1 through S6 displaying $\overline{u}/\overline{V}$, whereas S7 through S12 displaying $\overline{v}/\overline{V}$), at several locations S1 through S12 for pulsatile flow through the TASG geometry. (b) Normalized ensemble-averaged axial velocity (S1 through S6 displaying $\langle \overline{u}/\overline{V} \rangle_p$, whereas S7 through S12 displaying $\langle \overline{v}/\overline{V} \rangle_p$), at indicated locations.

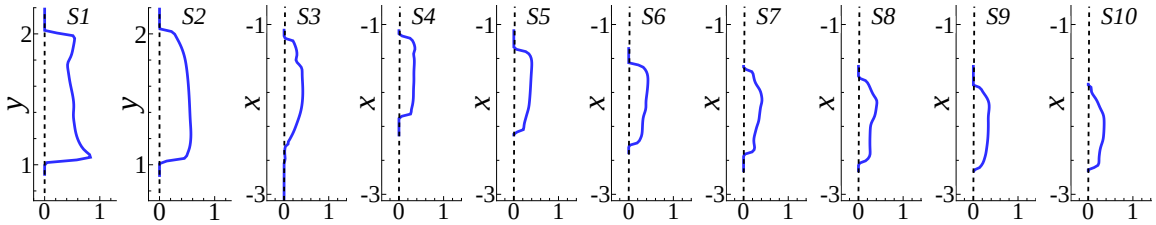

(a) P1

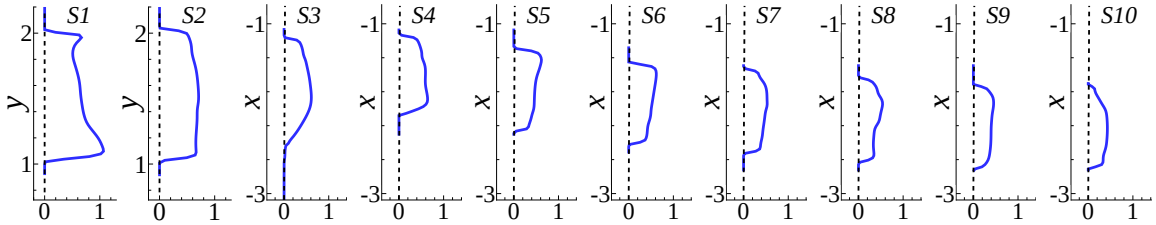

(b) P2

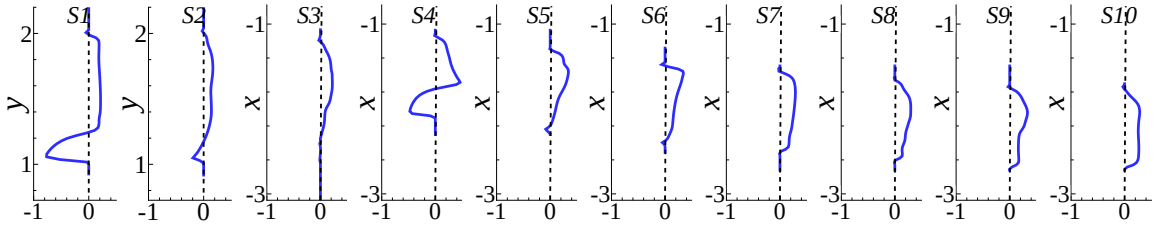

(c) P3

Figure 4.26. Sequence of ensemble-averaged normalized axial velocity profiles (locations S1 and S2 show $\langle \overline{u}/\overline{V} \rangle_p$, all other locations show $-\langle \overline{v}/\overline{V} \rangle_p$) at the indicated time instants, for pulsatile inflow through the TASG geometry.

peak values are 1%. The peak values of *tke* reached during the deceleration phase at P3 are however are around 1% which are lower by a value of 5% compared to those obtained in TAA case at location S1.

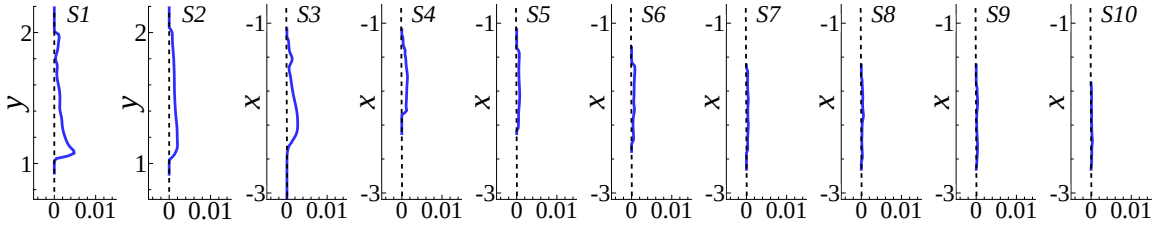

(a) P1

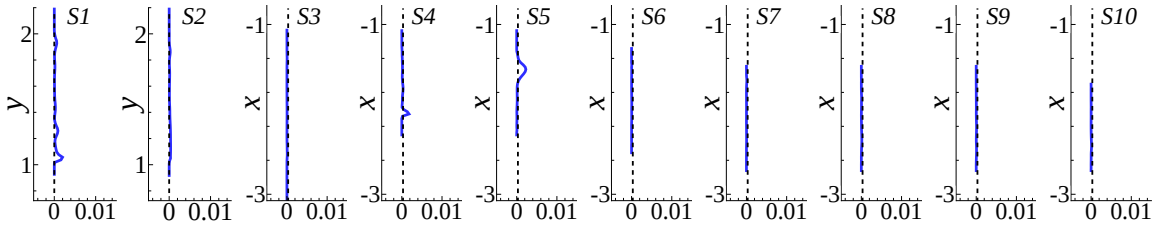

(b) P2

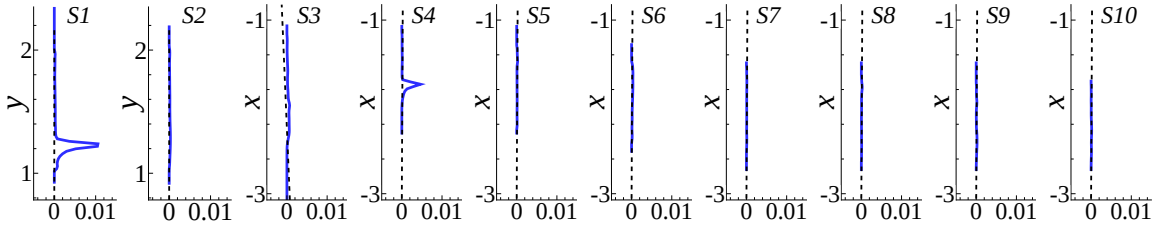

(c) P3

Figure 4.27. Sequence of ensemble-averaged normalized turbulent kinetic energy $\langle k \rangle_p / \overline{V}^2$ profiles at the indicated time instants, for pulsatile inflow through the TASG geometry.

Coherent Structures

To visualize and further understand the complex flow dynamics occurring in the TASG geometry, we make use of vorticity magnitude and λ_2 criterion similar to the TAA case. The nondimensional contours of vorticity magnitude on the $z = 0$ plane

are shown in Figure 4.28 at the indicated time instants. From this figure we note that during the systolic phase shear layer gets developed at two locations on the inner wall of the aortic arch and also in all the supra-arteries. As the inflow enters diastolic phase these shear layers get separated from the inner wall and move towards the center of the aortic arch. The initial two shear layers identified separate into three shear layers in the diastolic phase similar to the TAA case. However, the shear layers in the present case are more sharp and simple than those observed in the case of TAA, which has multiple concentrated vorticity regions within the three main shear layers identified. The vorticity production in the supra-arteries seems to be similar between the TASG and the TAA cases with high values obtained at P3 and P4 phase instants.

Further, the iso surfaces of instantaneous $\lambda_2 = -0.1$ are shown in Figure 4.29 at the indicated phases colored by nondimensional velocity magnitude. These iso surfaces of λ_2 obtained are different than those obtained in the TAA case. Longitudinal vortical structures seem to be present in the distal end of the aorta. Ring like vortical structures are identified in the ascending aorta and arch regions similar to the TAA case. However, vortical structures observed in the TAA case such as those originating from the aortic arch and extending towards the outer wall in the aneurysm region are absent in the present case. This can be understood given the absence of the aneurysm itself in the TASG case. The stent graft acting to provide a uniform cross sectional area enhances the flow and the pulsatile inflow nature can be observed farther down in the descending aorta with packets of vortical structures convecting downstream. These coherent packets of vortical structures seem to be slowly convecting downstream the descending aorta as one moves from the phase instants P3 through P6. Similar to the TAA case the vortical structures observed at phase instants P4 through P6 are hard to distinguish owing to the smaller inlet flow velocity.

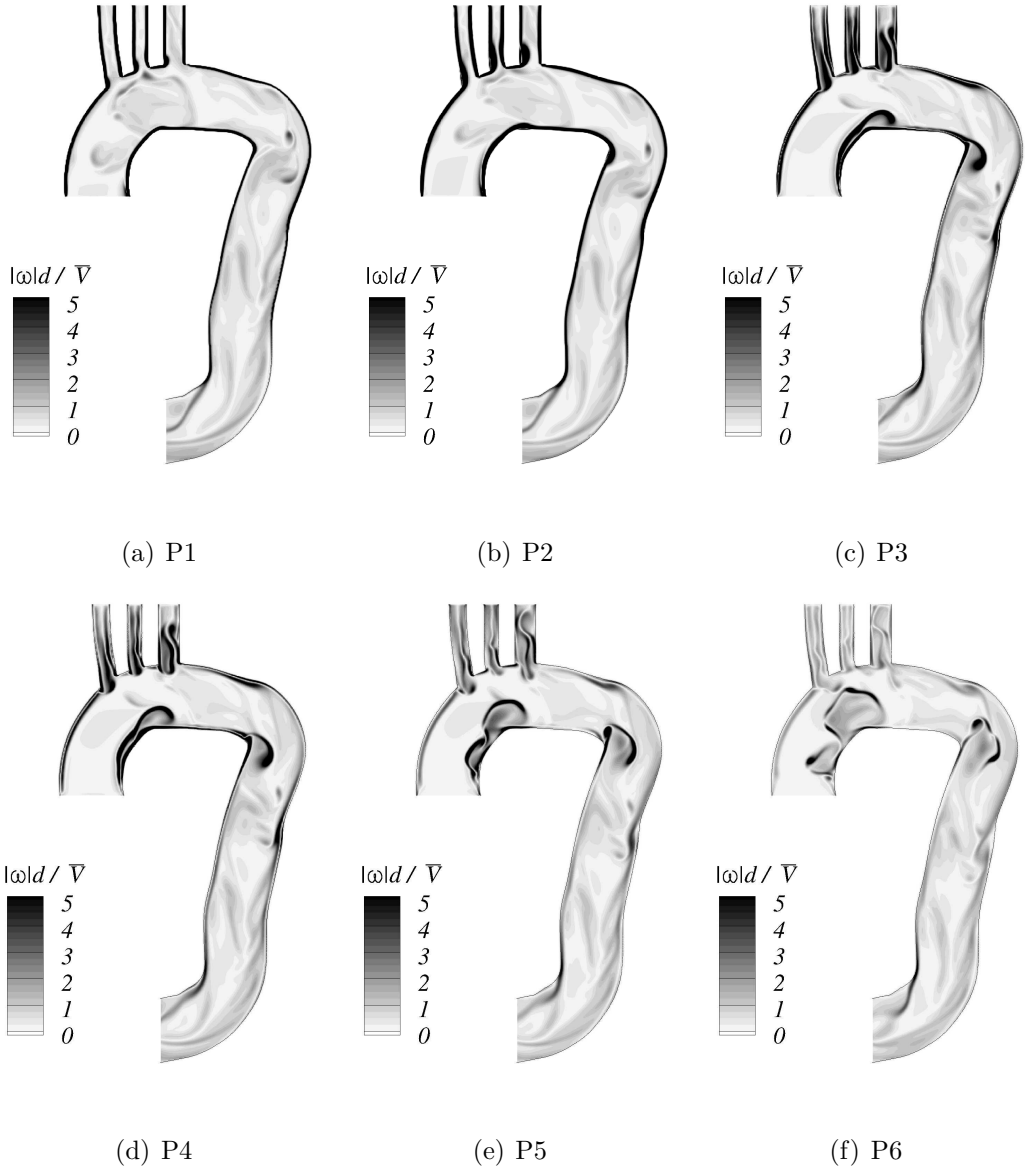

(a) P1 (b) P2 (c) P3

(d) P4 (e) P5 (f) P6

Figure 4.28. Sequence of ensemble-averaged contours of vorticity magnitude, normalized by $\overline{V}/d$, for pulsatile inflow through the TASG geometry.

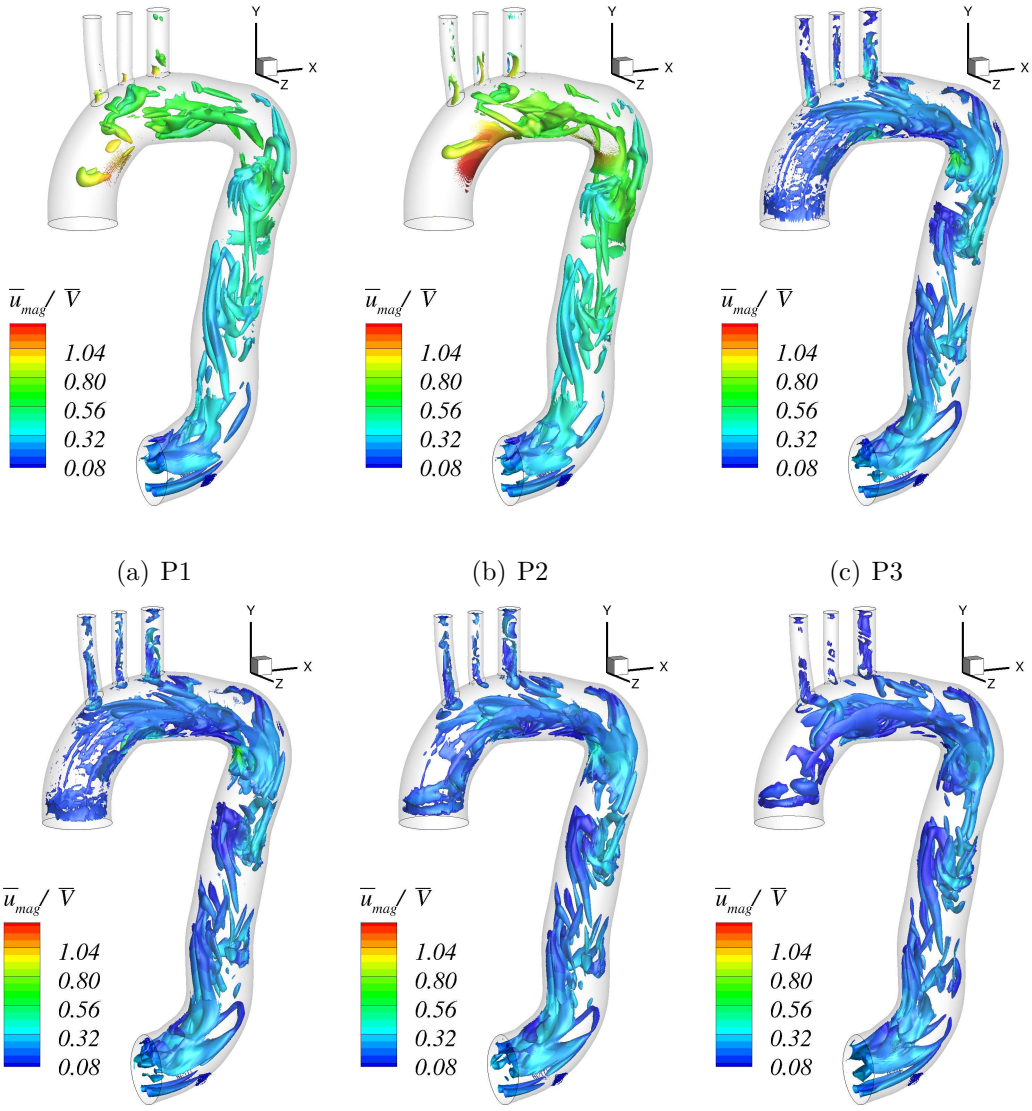

(a) P1 (b) P2 (c) P3

(d) P4 (e) P5 (f) P6

Figure 4.29. Sequence of instantaneous iso-surfaces of $\lambda_2 = -0.1$, colored by normalized velocity magnitude ($\overline{u}_{mag}/\overline{V}$), for pulsatile inflow through the TASG geometry.

Turbulence Energy Spectra

To further understand the range of scales obtained in the present case, we calculate frequency spectra at several probe locations. The spectra $E_{u'',u''}$ for points R1 and R3 are shown in frame (a) and $E_{v'',v''}$ obtained for points R9 and R12 are shown in frame (b) of Figure 4.30. Unlike the frequency spectra obtained for the TAA case, here we notice distinct peaks. Spectra at R1 shows a quickly decaying energy by $S = 0.1$ followed by distinct peaks of large amplitude. The first two peaks after $S = 0.1$ are identified corresponding to $S = 0.135$ and $S = 0.27$. These peaks with approximately at the same frequency are also seen at point R3. A clear turbulent spectrum either parallel to the inertial subrange or dissipation range cannot be noticed from frames (a) and (b) of the figure. The spectra at locations R9 shows similar trend with the corresponding peaks slightly shifted to values of $S = 0.139$ and $S = 0.273$. These frequencies slightly change further at location R12 to $S = 0.143$ and $S = 0.265$. At location R9 the spectrum seems to be parallel to the inertial subrange $S^{-5/3}$ over a small range of frequencies between $S = 0.1$ to $S = 1$. The spectra at any of the locations considered also do not show a clear range of frequencies in which they are parallel to the $S^{-10/3}$ line.

Wall Shear Stress

To evaluate the effect of stent graft on the wall shear stress we further compute the phase averaged wall shear stress. The variation of nondimensional wall shear stress is shown in Figure 4.31 at the indicated time instants. The peak values of skin friction coefficient are of the same order of magnitude as those obtained for the case of TAA, however, slightly lower peak values are observed consistently at any given phase instant in the case of TASG as compared to TAA. At peak velocity point and maximum deceleration point the skin friction values in the ascending aorta are in the upper to middle range of the spectrum considered. At the other phases a mixture of values is obtained over the entire surface of the aorta.

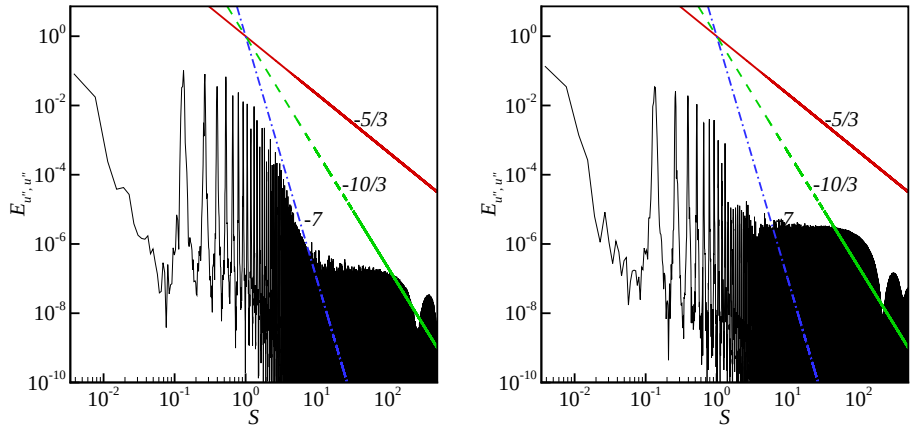

(a) R1 (b) R3

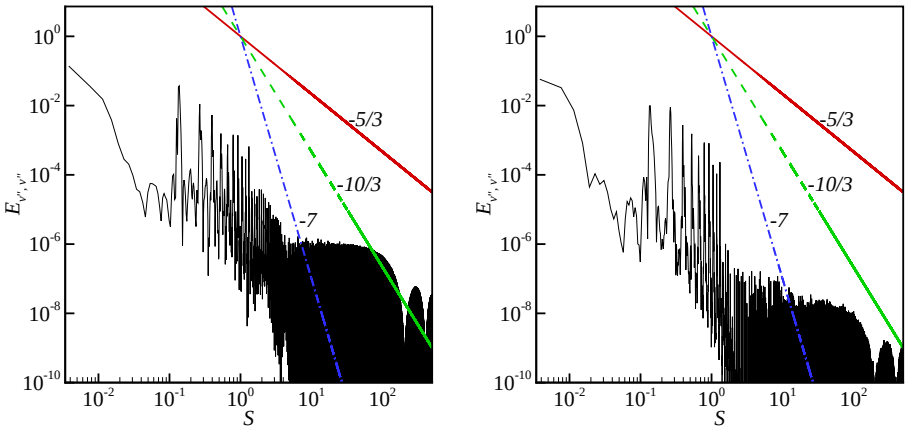

(c) R9 (d) R12

Figure 4.30. Energy spectrum associated with the stream-wise fluctuations (u'' for R1 and R3 and v'' for R9 and R12 for pulsatile inflow through TASG geometry at the indicated locations. Lines with slopes $-5/3$, $-10/3$ and -7 are also shown.

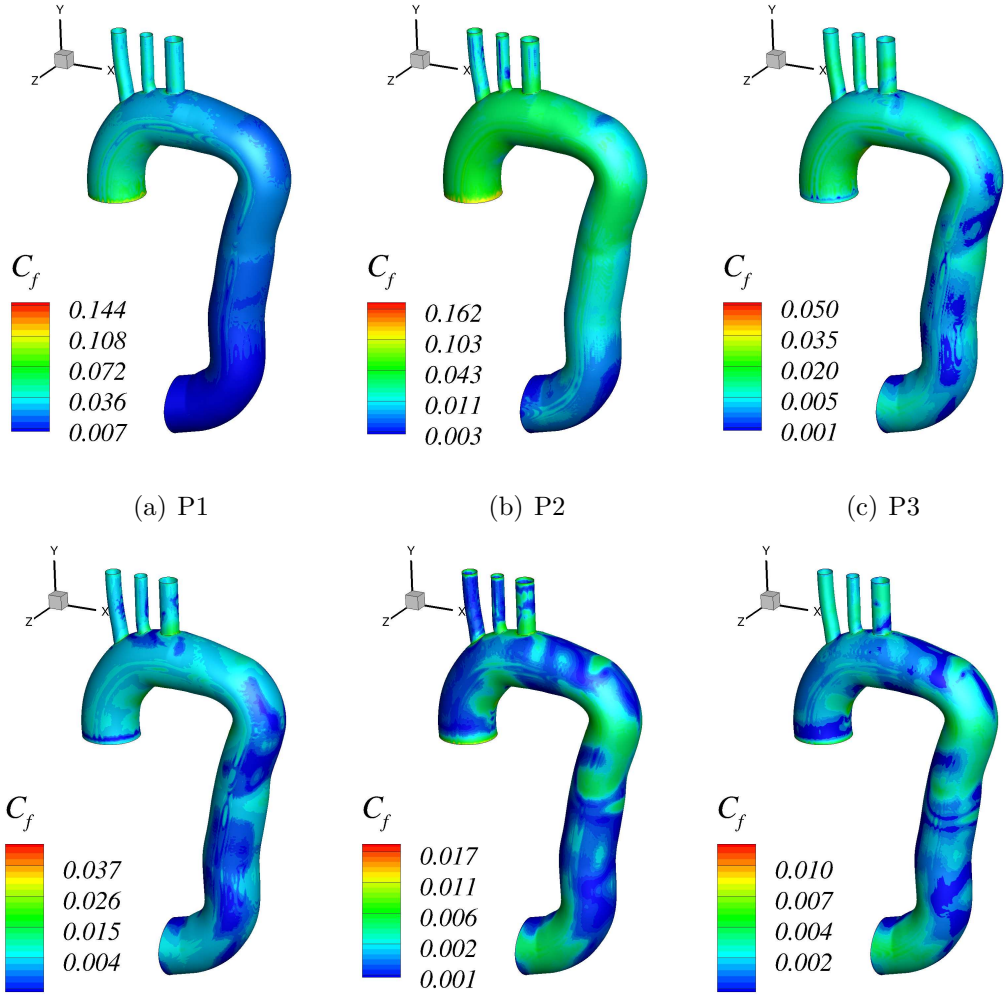

(a) P1 (b) P2 (c) P3

(d) P4 (e) P5 (f) P6

Figure 4.31. Sequence of ensemble-averaged contours of skin friction coefficient for pulsatile inflow through the TASG geometry.

Magnitude of Spatial Wall Shear Stress Gradient (SWSSG)

Similar to the TAA case, here we study the regions that are susceptible for possible formation of aneurysm in a TASG geometry. The contours of ensemble averaged SWSSG are shown at indicated phase instants in Figure 4.32. Similar to the case of TAA we see large values of SWSSG are obtained during the acceleration phase as noted at instants $P1$ and $P2$. Spatial distribution of large values of SWSSG is mainly concentrate in the ascending aorta region unlike in the regions in the aortic arch like in the case of TAA. This shows that the ascending aorta region is subjected higher values of SWSSG and may be susceptible for aneurysm formation.

4.4.5 Discussion and Conclusions

The focus of the present study is to compare the changes brought about to blood flow in an endovascular treated thoracic aortic aneurysm. In order to evaluate the same, two different geometries one corresponding to the patient specific pathological aorta, TAA, and the other one corresponding to the medical device solution, TASG, are studied for same inflow and outflow boundary conditions. A scale resolving turbulence model such as LES is used with Vreman SGS stress turbulence model with a motivation to capture and quantify the transitional, turbulent flow behavior that exists in this types of flows. A large number of pulsation cycles amounting to 55 are considered, which is consistent with the previous LES studies [11], however, only the last 35 cycles are used for data reduction purposes discarding the first 20 cycles as it was observed from the temporal evolution of the velocity a visually periodic state is only reached by then. Since, the cycle to cycle variations contribute directly to the turbulence energy levels, by definition in pulsatile flows, the statistics collection undertaken in the present work is thought to be justified.

Overall, the enhanced blood flow rate in the descending aorta is observed in the TASG geometry when compared with TAA. This could be attributed to the presence of aneurysm in the TAA geometry which poses higher resistance to the flow thereby

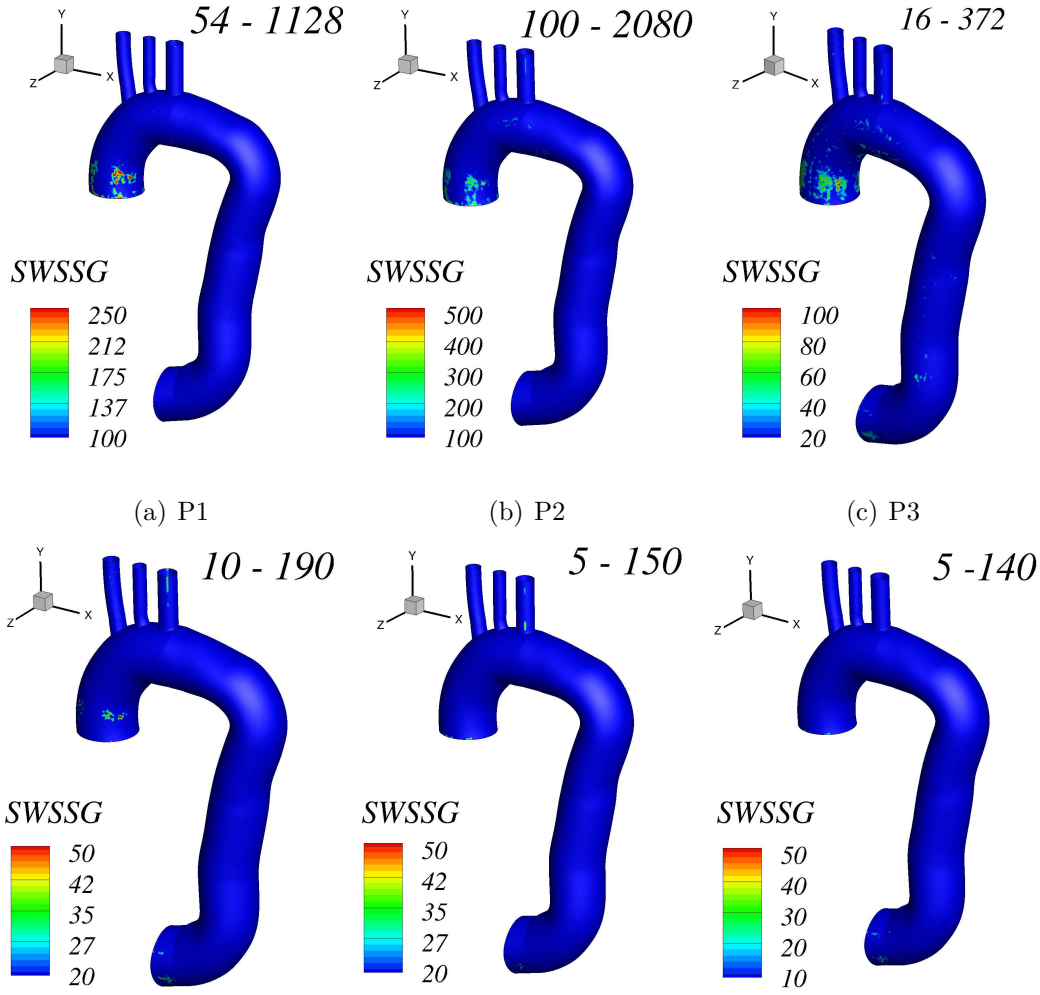

(a) P1 (b) P2 (c) P3

(d) P4 (e) P5 (f) P6

Figure 4.32. Sequence of ensemble-averaged contours of spatial wall shear stress gradient for pulsatile inflow through the TASG geometry. Note the contour levels shown are not the same for all frames and the maximum and minimum values are shown on the upper right corner with only a small range of values used for the contour levels indicated.

decreasing the blood flow rate downstream. Further lower levels of turbulence kinetic energy are found in the aortic arch region in TASG geometry in comparison to the TAA geometry. TAA is characterized with vortical structures dominated in the aortic arch and aneurysm region whereas in TASG the vortical structures are identified as corresponding to the vortex shedding that is taking place because of the more uniform cross sectional area of the TASG geometry from inlet to outlet. A comparison of vorticity magnitude indicates several small shear layers present within the three main shear layer roll-up in the aortic arch region in the TAA geometry, whereas the TASG geometry shows presence of three distinct shear layers rolling up in the arch region as the flow decelerates during diastole. Nondimensional wall shear stress are compared by means of skin friction coefficient values. Overall slightly lower skin friction coefficients are observed at any phase in TASG compared to TAA, however, these differences are too small to make definitive conclusion on the lowering of wall shear stress values because of a medical device solution. Investigation of turbulence energy spectra indicate well developed inertial subrange at certain location in aortic arch in the TAA geometry, whereas TASG shows distinct peaks in the spectrum corresponding to the vortex shedding frequency of the shear layers.

There are several limitations of the present study, which result from the many assumptions made in the simulation as described in the section 4.4.2, as a consequence, the results obtained cannot be directly transferred to clinically relevant data. But it is thought that the flow dynamics observed and the conclusions drawn hold good under the assumptions made for the geometries considered providing insights into reducing post repair complications.

5. LARGE EDDY SIMULATION OF A BI-LEAFLET MECHANICAL HEART VALVE

5.1 Introduction

During the systolic phase the aortic valve opens and blood flow takes places out of the contracting ventricle into the aorta. The Mitral valve serves a similar purpose in transmitting blood between the atrium and ventricle on the left side of the heart. In most of the population the aortic valve is a tri-cuspid valve; however, in 1% of the population it is found to be bi-cuspid, whereas the Mitral valve is a bi-cuspid valve. Natural heart valves are thin, flexible leaflets that open and close under the action of blood pressure allowing it to pass through ensuring blood circulation throughout the body. Heart valves are prone to plaque formation eventually leading to a stenosed or a modified configuration which becomes leaky. Leaky heart valves cannot hold the blood during diastolic phase of the ventricle and as a result the blood pumping capacity of heart during systolic phase becomes weak thereby disrupting the physiological function of the heart. This condition is considered pathological and a surgeon would consider replacing it with prosthetic heart valve depending on the severity and urgency of the need. These artificial heart valves can be of one of 50 mechanical heart valve designs that are in use or they can be a tissue or a biological valve. The number of leaflets, valve material and type of passive (operated by blood pressure alone) oscillating mechanism for opening and closing constitute the main differences between several existing valve designs.

5.2 Previous Studies

In this section, we review previous experimental and numerical studies on prosthetic heart valves. Existing types of mechanical heart valves, fluid mechanics and

simulation modeling approaches applied to them are reviewed by Yoganathan et al. [71]. As described in this review article [71] three major types of prosthetic heart valve designs are in use, they are caged ball, tilting disc and bi-leaflet heart valves. The focus of the present study is only limited to evaluating a bi-leaflet mechanical heart valve (BMHV) placed in a model aorta. A quick survey of few major artificial heart valves can also be found in Dasi et al. [72] who discussed the fluid mechanics and how advances in experimental and computational techniques are shaping the artificial heart valve designs.

There have been several experimental studies using particle image velocimetry with a motivation to understand the flow field characteristics and blood flow complications that occur with the use of medical devices [73–77]. Leo et al. [78] performed experimental investigations of a polymeric heart valve that forms the latest heart valve design which emulates a natural aortic valve. However, the BMHV design is the most widely used heart valve design to date.

Krafczyk [79] et al. studied a stationary mechanical configuration at two opening angles of 40 deg and 12 deg with pulsatile inflow conditions using lattice Boltzmann methods. Although, it is not consistent to keep the valve leaflets fixed and apply a pulsatile inflow conditions it served as one of first approximation studies to gain insight into the flow dynamics and fluid shear stresses in the model artery fitted with a mechanical heart valve. Grigioni et al. [80] also considered static leaflets in fully open position and simulated the flow field for the peak velocity. They used a tri-fold symmetric aortic root geometry which is more realistic but their assumptions of laminar flow field at a peak Reynolds number of 3350 made a mismatch of the numerically computed results with the accompanying *in vitro* observed mixing downstream of the leaflets. De Tullio et al. [81] performed DNS studies on pulsatile flow through a BMHV placed in a realistic aortic root geometry. They employed a fluid structure interaction algorithm together with IBM to compute the forces acting on the valve leaflets and update their kinematics. They compare the leaflet dynamics and velocity profiles obtained from phase averaging 10 simulated flow cycles to experimental

results obtained for a similar geometry. They conclude that viscous and turbulent shear stresses attain comparable magnitudes in different flow regions pointing to the need to consider them in hemolysis and platelet activation studies. They, however, suggest need for further improvement in these simulations by using a greater number of simulated flow cycles to get converged root mean square quantities. In a similar study to compare the numerically simulated leaflet dynamics with the experimentally obtained results Dasi et al. [82] imposed experimentally measured leaflet kinematics in the numerical simulations and studied the evolution of vorticity and coherent structures in an impulsively started simulation. In spite of many simplifications employed in the numerical simulations, such as plug flow velocity inlet profile, cycle-to-cycle asymmetries in the motion of the leaflets, inlet disturbances etc., they found the simulated vorticity dynamics to be in good overall agreement with the measurements. Motivated by the effect of viscous stresses levels on the red blood cells and platelet activation, Ge et al. [83] performed numerical simulations in an axisymmetric aortic geometry with a BMHV in tandem with $2D$ high resolution particle image velocimetry measurements. The numerical algorithm in their simulations utilized a curvilinear immersed boundary method and the leaflet kinematics are imposed as a boundary condition. Through both their simulations and experiments they conclude that the viscous stresses in the downstream region of the leaflets could potentially damage platelets, however, stresses obtained are too low to effect red blood cells.

While the aforementioned numerical studies employed IBM as the main methodology for valve leaflet modeling, Nguyen et al. [84] employed arbitrary Lagrangian Eulerian (ALE) formulation in a finite volume method in their numerical solver. They used RANS equations together with two turbulence models, namely, Spalart-Allmaras (SA) and $k-\epsilon$ models. Their study was motivated by the validation of their numerical solver with the experimentally obtained results from PIV measurements at three different Reynolds numbers of 350, 750 and 1000. Like most the previous numerical studies the leaflet kinematics are prescribed accompanied by pulsatile inflow boundary conditions on velocity. Cheng et al. [85] also used ALE formulation for nu-

merical simulations on a one quarter model of the leaflet and the aorta model. Their study showed that large negative pressure transients could occur close to the leaflet edges during closing and rebound phases. Using similar numerical methodology using a commercial fluid dynamics software FLUENT, together with a fully implicit fluid structure interaction coupling procedure available with in that software, Dumont et al. [86] compared the performance of two commercially available bi-leaflet mechanical heart valves, namely, the ATS Open Pivot Valve and the St. Jude Regent Valve. Their study focused on evaluating hemodynamic and thrombogenic performance of these two bi-leaflet heart valve designs which differed mostly in the hinge mechanism used for mounting the leaflets. They conclude that the two designs lead to different potential for platelet activation, especially during the regurgitation phase.

There are several studies which focused on 2D BMHV simulations. Bluestein et al. [87] performed RANS based simulations using $k-\epsilon$ turbulence model in commercial fluid dynamics software FIDAP for 2D BMHV configuration under fully open condition. Their observations from numerical results were also verified by digital particle image velocity (DPIV) measurements. They postulated that the vortex shedding that takes places from the leaflets under unsteady pulsatile inflow conditions provides conducive atmosphere for the generation of cerebrovascular microemboli that carry cardioembolic stroke risk. They hypothesize that vortex shedding from the leaflets promotes free emboli formation and the convection of these downstream through vortex shedding can further cause systemic emboli. Platelet activation is further investigated by Krishnan et al. [88] using highly resolved, adaptive mesh technique in a 2D simulation. They used Lagrangian particle tracking method to incorporate hemodynamic forces on the particles. The motion of the leaflets is computed using a fluid structure interaction algorithm. They conclude that the interaction between the shear layers that get developed downstream of the leaflets create a region of rotating flow with high shear stress and high particle residence times which may lead to platelet activation. Govindarajan et al [89] further extended these simulations to study flow and platelet dynamics in the hinge region of the leaflets. With the insights gained

from the 2D rectangular leaflet simulation they further modify the leaflet geometry to a more streamlined elliptical configuration. Results obtained for this geometry did not change the plate activation parameter, however, the number of particles trapped in vortex roll up got reduced. They point out a need to perform parametric design optimization studies to come up with a leaflet design that reduces platelet activation and thrombus formation. Alemu et al. [90] did pursue this idea of design modifications. They optimize the ATS valve thrombogenic performance, by modifying several design features of the valve, such as, leaflet - housing gap, effective maximum opening angle of the valve, streamlining the gap between leaflet stops of the valve. Through this test case they demonstrate that the Device Thrombogenicity Emulator (DTE) optimization methodology can be used as a test bed for medical device development to achieve significant improvements in thrombogenic performance. In a related study, Fogelson & Guy [91] developed a model to describe the formation of platelet thrombi in coronary-artery sized blood vessels. By using two spatial scales, one representing the microscale of the platelets and the other one representing the macroscale of the blood vessel, they demonstrate that the proposed model produces thrombi growth and occlude the blood vessel and their geometrical shapes get effected by the fluid shear-stresses.

Mechanical heart valve implants pose a risk of blood damage, thromboembolic events, blood coagulation, hemolysis and material failure of the device. Some of these events are believed to be caused because of non-physiological blood flow patterns created by the implanted device. There have been cases of mechanical heart valve failure in the past where a particular heart valve design was withdrawn from the market after it was observed that the valve material got deteriorated and one of the leaflets escaped causing severe valve insufficiency and embolism [92–99]. Klepetco et al. [100] further investigated two cases of this valve failure from two patients following complications that arose at 36 and 38 months after implantation. The embolized leaflet parts are detected in the iliac artery region using a computed tomographic scan and removed. Evaluation of these parts showed crack growth which is indica-

tive of fatigue failure. Scanning electron microscope examination revealed areas of pitting and erosion on the recovered parts. They point out that the exact mechanical disruption is speculative; however, the material used for the leaflets which is pyrolytic carbon could be susceptible to fatigue fracture as well as erosion damage. This type of erosion damage resembled the damages caused by cavitation, which is also observed in other engineering machinery such as steel turbines, ship propellers, journal bearings, and impellers [101–104]. Cavitation occurring in mechanical heart valve erosion damage is first pointed out in 1976 by Zubarev et al. [105]. They also suggested that thrombogenesis is qualitatively related to the turbulence of the blood stream on the prosthesis. They observed structural changes on the surfaces of the material to a depth of 0.05 mm. This observed erosion damage is presumed to be related to saturation of the material of the surfaces with the gases released as a result of cavitation in the close vicinity of prosthesis. A review of cavitation in mechanical heart valves is presented by Johansen [106]. Kafesjian et al. [107] documented cavitation erosion damage for over a hundred BMHV designs collected from simulators and animal studies. They reported location, type and severity of cavitation damage on the observed *in vitro*. Most of the fractures they studied have a focal pit indicating pitting as the primary damage mechanism. They suggest that the leaflets made of pyrolytic carbon components be highly polished with fewer micro-pores so that cavitation nucleation sites are drastically reduced and the leaflets may be able to withstand cavitation forces. Graf et al. [108] performed *in vitro* studies to investigate causes and formation of cavitation in BMHV. They found that cavitation is produced primarily because of the deceleration of the closing leaflet of the valve which they measured to be a very high value of $900g$. Such a high value of deceleration falls in the range of cavitation induced material erosion. They conclude that future BMHV designs need to reduce unsteadiness in the back flow during the valve closure phase. In a related study [109], they performed *in vitro* studies on ten different types of commercially available heart valves to detect cavitation thresholds for temporal pressure gradients. They measured cavitation bubbles with a diameter of up to 1.8 mm and

with a collapse time of 0.1 ms in all most all the models considered and the temporal pressure gradient threshold to be sometimes within the physiological range of 2000 mm Hg/s. Lee et al. [110] have also performed *in vitro* studies on Medtronic tilting disc valve to understand the cavitation effect during the valve closure. They found surprisingly low threshold values for pressure loading rate in the range of 300 to 400 mm Hg/s. There are several *in vitro* studies [111–113] which focused on visualizing the cavitation bubble in the inlet region of the valve. Wu et al. [113] specifically point out that the mounting compliance plays a significant role in cavitation inception and subsequent bubble growth. They also suggest the possibility of detecting cavitation by using a high frequency pressure transducer placed in the atrial chamber. While most of the cavitation detection experiments discussed above focused on visualizing the cavitation bubble and making qualitative comparisons, Garrison et al. [114] developed a quantitative measure to determine cavitation level. Their proposed method is based on measuring high frequency pressure fluctuations downstream of the valve leaflets. They have also shown that hemolysis increases with increase in cavitation level.

5.3 Present Study

There are several *in vitro* experimental efforts towards predicting, understanding and reducing initiation of cavitation in BMHV as discussed in Section 5.2, and further there are several efforts also towards numerically simulating the blood flow dynamics in the BMHV. However, numerical simulations towards understanding and predicting cavitation are still lacking. The difficulty to detect cavitation *in vivo* provides a strong motivation to pursue numerical or *in vitro* studies towards designing BMHV and understanding the associated blood flow dynamics. In the following, we first study a stationary BMHV configuration at the peak velocity and corresponding maximum opening of the leaflets, followed by an oscillating BMHV configuration with imposed

kinematics of the leaflets. However, the study of predicting and simulating cavitation that may form is not accomplished in the present work.

5.4 Geometry and Boundary Conditions

The geometry of the BMHV considered in the present study is shown in frames (a) and (b) of Figure 5.1 in two views. Both the leaflets are at the maximum opening configuration and the inflow velocity corresponds to peak velocity. The diameter of each of the valves (d) is taken to be the length scale and the maximum velocity ($\overline{U}$) at the inflow is taken as the velocity scale. The peak Reynolds number defined based on this length and velocity scales is taken to be 3727, which is equal to the peak Reynolds number considered in the earlier studies on TAA and TASG. The model aorta used in the present study is a pipe with uniform diameter equal to $1.2d$ and a length equal to $5d$. The leaflets are placed at the origin located $1d$ from the inlet of the aorta to account for the back flow that takes place during the deceleration phase of the pulsation. A uniform velocity inlet boundary condition is applied with a steady value corresponding to $\overline{u}/\overline{U} = 1$ in the case of static leaflets case whereas a model time dependent velocity profile as shown in Figure 5.2 is used in the case of dynamic leaflets case. As can be seen from Figure 5.2, flow accelerates and decelerates during systolic phase ($0 < t/T < 0.5$) which occupies a period of $t/T = 0.5$ and during the rest of the time period no flow occurs through the inlet and the leaflets are in closed position making right angle with $y/d = 0$ plane. The leaflets begin from a fully closed position at $t/T = 0$ and start rotating at constant angular velocity of 2π rad/sec. The top leaflet (identified as the one in $y/d > 0$ region) starts rotating clockwise about z axis whereas the bottom leaflet (identified as the one in $y/d < 0$ region) starts rotating counter clockwise about z axis. At the end of the time period of $t/T = 0.25$ both leaflets attain fully open or horizontal position and they reverse their respective rotation directions keeping axis of rotation the same so as to reach a fully closed position by a time of $t/T = 0.5$. During the diastolic phase ($0.5 <= t/T <= 1.0$)

during which no inlet flow takes places as shown in Figure 5.2 both the valves remain stationary in the fully closed position. In both static and dynamic valve simulations a homogeneous Neumann boundary condition on velocity components ($\frac{\partial \overline{u_i}}{\partial x} = 0$) is applied together with a Dirichlet boundary condition on pressure. A no-slip boundary condition is imposed on the walls of the model aorta. The velocity boundary condition the valve leaflets is also a no-slip boundary condition, as follows:

$$\overline{u}_i = \frac{\partial X_i}{\partial t} \tag{5.1}$$

where X_i is the instantaneous location of the valve leaflets, which is a constant value in the static valve case leading to a zero fluid velocity boundary condition on the leaflets, whereas it is computed based on the leaflet rotations during opening and closing phases in the dynamic valve case. The leaflets rotate about locations $y/d = \pm 0.05$ when measured in the fully open phase. These locations are supposed to the places where the leaflets are mounted on hinges in reality. The leaflets only occupy an area corresponding to a diameter d whereas the model artery fluid flow cross sectional area corresponds to a diameter of $1.2d$ which gives a blockage diameter ratio of 0.833 for the flow to pass through. This blockage ratio will be close a value of 1 in the real BMHV geometry with allowances for placing the mechanical hinges. Also, in the real BMHV configuration the opening and closing of the leaflets is achieved only over a rotation angle close to 55 degrees unlike a rotation angle of 90 degrees considered in the present study.

5.5 Stationary Bi-leaflet Mechanical Heart Valve (BMHV)

A stationary BMHV simulation corresponding to maximum opening of leaflets and maximum inflow velocity (corresponding to $Q2$ point in Figure 5.2) is considered in the present section. This flow configuration corresponds to a peak Reynolds number of 3727. The geometry and boundary conditions are applied as discussed in Section 5.4. This flow setting corresponds to the configuration depicted in Figure 5.1. A mesh resolution of $15 \times 20 \times 120$ is used with $30 \times 6 \times 1$ blocks in each of the x, y and z

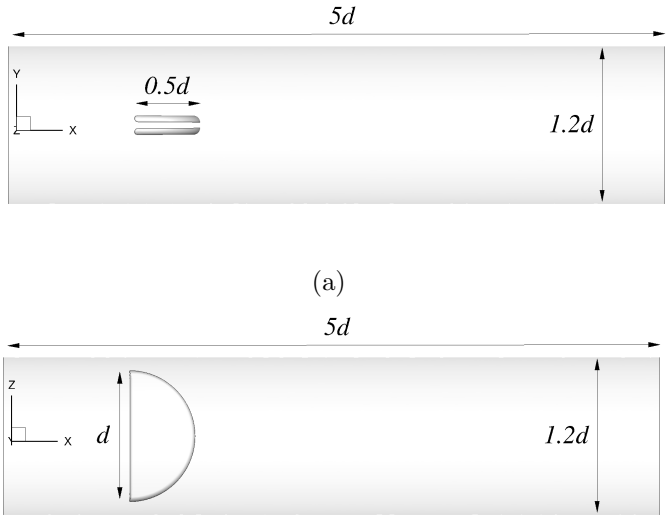

Figure 5.1. Schematic of the bi-leaflet mechanical heart valve placed in a model artery. Each of the leaflets is at the maximum opening phase.

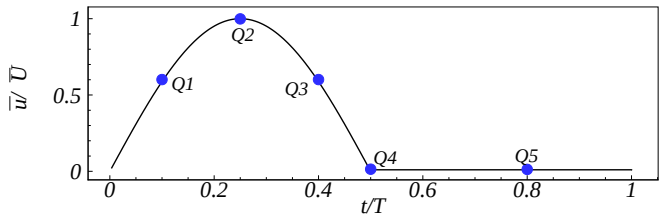

Figure 5.2. Model pulsating inlet velocity profile together with five selected temporal locations ($Q1$ through $Q5$) for phase averaging of the flow field.

directions respectively, amounting to a total resolution of 6.48 million mesh points. A time step of $1e-03$ is used to advance the simulation and the turbulent statistics are collected over a period of 20 nondimensional time which equals 4 flow through time. Time averaged nondimensional axial velocity profiles are shown in Figure 5.3 at indicated x/d locations along the axis of the model aorta on two central planes. Frames (a) and (c) denote the orientation of the leaflets which are located at $x/d = 0$, but shown separately for clarity. The $z = 0$ plane passes right through the leaflets whereas the plane $y = 0$ does not interest with the leaflets. From frames (b) and (d) of this figure we note that the velocity profile at $x/d = -0.5$ which is located upstream of the leaflets is a profile that can be expected in a pipe flow and the similarity of these profiles at this location in both the planes confirms the axisymmetric nature of the flow at this location. As we move downstream, the leaflets cause the flow to stick to them through along their surface causing the flow to split into three separate regions, one between the leaflets and one each between the leaflet and the walls of the model aorta. The no-slip boundary condition on the leaflets can be perceived from the velocity profiles at locations $x/d = 0.0$ and at $x/d = 0.5$. At the same location in frame (d) we see the velocity profile formed in the central jet region. As we move downstream, we note from frame (b) that the velocity boundary layers from both the leaflets merge with the central jet region causing the velocity profile to return to a profile similar to the one noted upstream of the leaflets. However, as we see from frame (d) the velocity profiles on $y = 0$ plane does not return to a similar profile as the undisturbed profile noted at $x/d = -0.5$. As as result the flow field downstream of the leaflets even at $x/d = 4.0$ is not axisymmetric but it seems to be having symmetric profiles about lines $y = 0$ and $z = 0$ in the xz and xy central planes respectively. Next, we turn to look at the turbulence kinetic energy (tke) profiles. The time averaged normalized tke profiles are shown in Figure 5.4. Frames (a) and (c) indicate the orientation of the leaflets whereas frames (b) and (d) show the variation of tke profiles at indicated axial locations along the axis of the model aorta. As we can see from frames (b) and (d) the tke starts to develop downstream

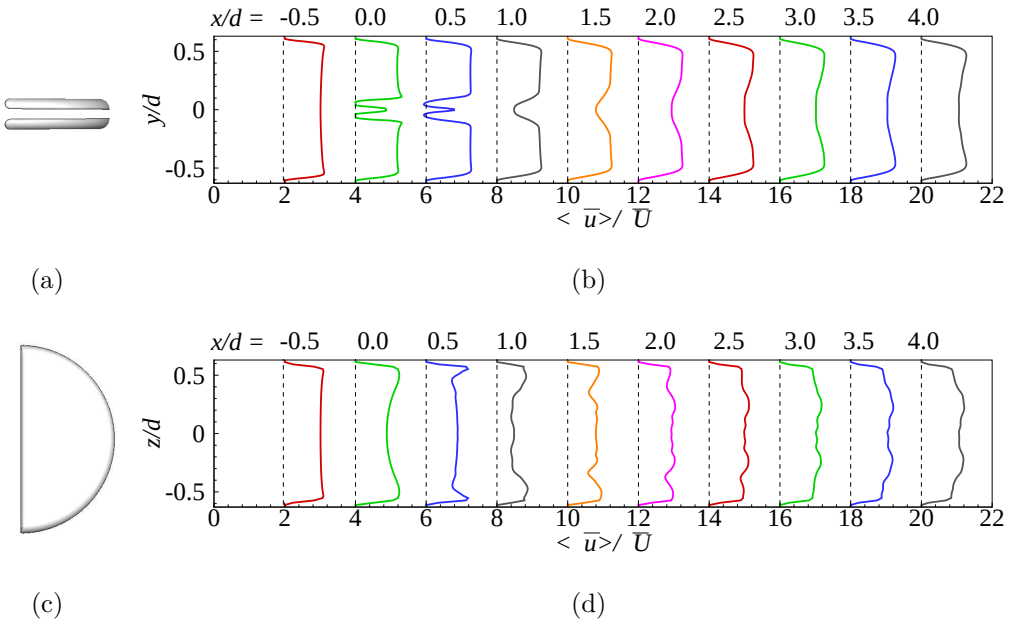

Figure 5.3. (a) Orientation of the leaflets as seen from z = plane. (b) Time averaged axial velocity profiles on $z = 0$ plane, at indicated locations in the steady inflow to the BMHV at the maximum opening phase in a model aorta. (c) Orientation of leaflets as seen from $y = 0$ plane. (d) Time averaged axial velocity profiles on $y = 0$ plane, at indicated locations in the steady inflow to the BMHV at the maximum opening phase in a model aorta. The corresponding phase of the leaflets is shown to the left of the profiles for clarity which are otherwise located at $x/d = 0$. Note the scale on the x and y axes is not the same.

at a location $x/d = 1.0$ which is $0.5d$ downstream of the location from the trailing end of the leaflets. This is an interesting phenomenon showing the interaction of the top and bottom shear layers with the central shear layer only happens downstream of the leaflets. From this figure we can see that a maximum of around 5% *tke* is noted at a location $x/d = 1.5$. The *tke* production starts to increase as we move away from the leaflets at location $x/d = 0.5$ reaching a maximum value at $x/d = 1.5$ and then it starts decreasing as we move further towards the distal end of the model aorta. The profiles start of similar to a Gaussian profile in the $z = 0$ plane but slowly decays into a profile with three peaks towards the distal end. The profiles in the $y = 0$ plane also begin as one resembling Gaussian profile but very quickly a double peak structure followed by a four peak structure and then diffuses into a close to a two peak structure by $x/d = 4.0$. The *tke* production is essentially zero from the inlet of the domain until $x/d = 0.5$. Similar to the mean axial velocity profiles noted above, the *tke* profiles seem to be symmetric in each of the planes considered, but they are not axisymmetric at any of the locations where they are non-zero.

The interaction of the two shear layers with the central jet region can be further appreciated by looking at the vorticity magnitude contours. Instantaneous nondimensional contours of vorticity magnitude are shown in Figure 5.5 on two perpendicular planes $z = 0$ and $y = 0$ in frames (a) and (b) respectively. Equally spaced 20 contour levels ranging from 0 to 20 are used for depicting the vorticity distribution in these figures. We can see the two shear layers on the upper and lower sides of each of the leaflets interacting in frame (a). Alternate vortex shedding takes places similar to von Karman vortex street as if the two leaflets act as a single body. The interaction shows a intense vorticity distribution on the plane $y = 0$ in frame (b) of the figure. The intensity of vorticity seems to be large close to the production region which happens to be on the surfaces of the leaflets and decreases as we move away from them. Vorticity production from the walls of the model aorta is also seen which seems to be interacting with the shed vortices from the leaflets at downstream locations as far as $x/d = 3$.

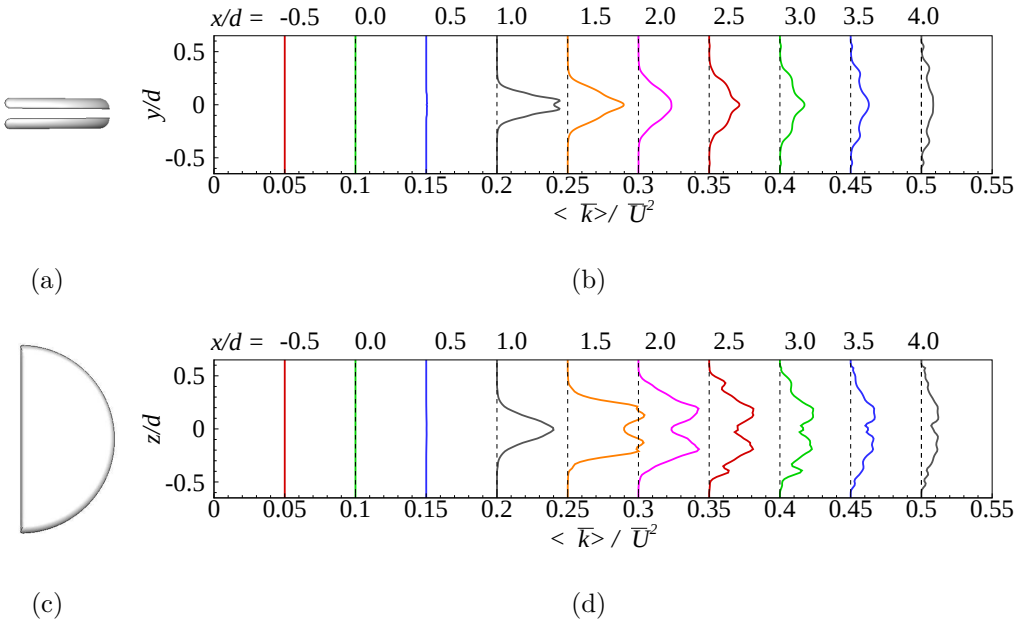

Figure 5.4. (a) Time averaged normalized turbulent kinetic energy ($< \overline{k} > /\overline{U}^2$) profiles on $z = 0$ plane, at indicated locations in the steady inflow to the BMHV at the maximum opening phase in a model aorta. (b) Time averaged normalized turbulent kinetic energy ($< \overline{k} > /\overline{U}^2$) profiles on $y = 0$ plane, at indicated locations in the steady inflow to the BMHV at the maximum opening phase in a model aorta. The corresponding phase of the leaflets is shown to the left of the profiles for clarity which are otherwise located at $x/d = 0$. Note the scale on the x and y axes is not the same.

To further illustrate the interaction of the shear layers we educe the vortical structures using iso-surfaces of λ_2 introduced by Jeong & Hussain [56]. The iso-surfaces of $\lambda_2 = -2$ are shown in Figure 5.6 in two different views as seen from planes $z = 0$ and $y = 0$ in frames (a) and (b) respectively. The colors indicate nondimensional instantaneous velocity. Alternate vortex shedding from each of the leaflets can be seen from frame (a) of this figure. Also long vortical structures emanating from the sides of each of the leaflets can be seen in both the views. The vortex structures grow linearly in size as we move downstream and they also interact with the long coherent structures. Complex interaction of these coherent structures is noted downstream of the leaflets. The configuration studied in the present case under stationary BMHV produces quite a different flow field compared to the physiologically relevant oscillating BMHV case as we will further investigate in the next section.

5.6 Oscillating Bi-leaflet Mechanical Heart Valve (BMHV)

In this section, we imposed the motion of the leaflets and also apply pulsatile inflow boundary conditions to be consistent with it. The pulsatile inflow profile is shown and discussed before in Figure 5.2. Five sampling points $Q1$ through $Q5$ are marked on this figure for the purpose of phase averaging the data. As the leaflets move during the simulation a further refined mesh is employed for the present simulations. A mesh size of $15 \times 14 \times 140$ is used with $30 \times 10 \times 1$ blocks in each of the x, y and z directions, making an overall resolution of 8.82 million mesh points. The simulation was run for a total of 35 nondimensional time which corresponds to 35 pulsatile cycles and only the last 15 cycles were used for statistics collection.

The phase averaged normalized axial velocity profiles are shown in Figure 5.7 at the indicated axial locations along the model aorta. The corresponding orientation of the leaflets is shown to the frames in the left column, for clarity, which are otherwise located at $x/d = 0$. From this figure, we note that axial velocities as high as $3\overline{U}$ are reached in the central jet region during mid acceleration at point $t/T = Q1$. The

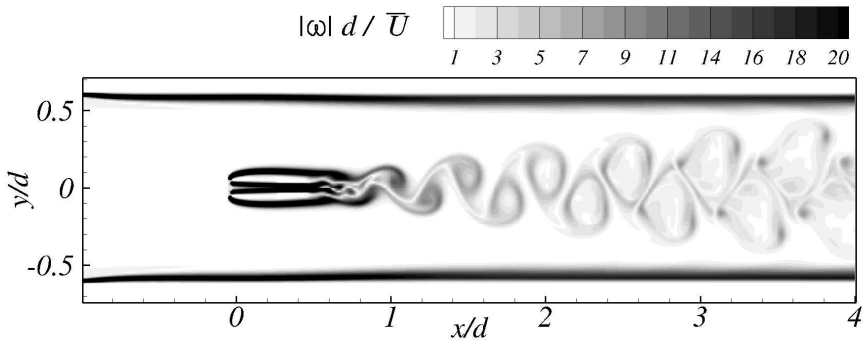

(a) $z = 0$ plane

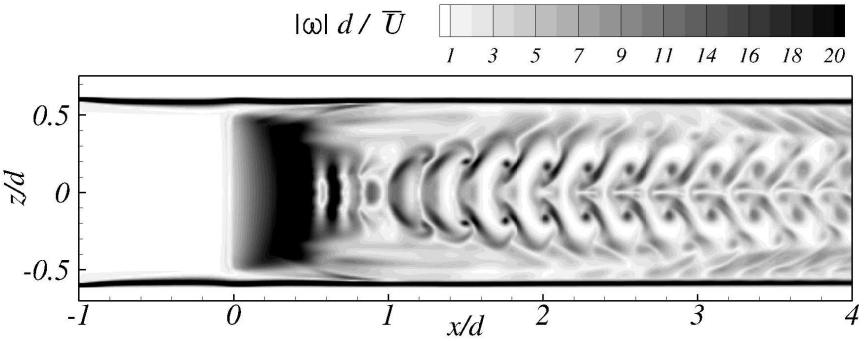

(b) $y = 0$ plane

Figure 5.5. Instantaneous contours of normalized vorticity magnitude shown on (a) $z = 0$ plane (b) $y = 0$ plane, in the steady inflow to the BMHV at the maximum opening phase in a model aorta.

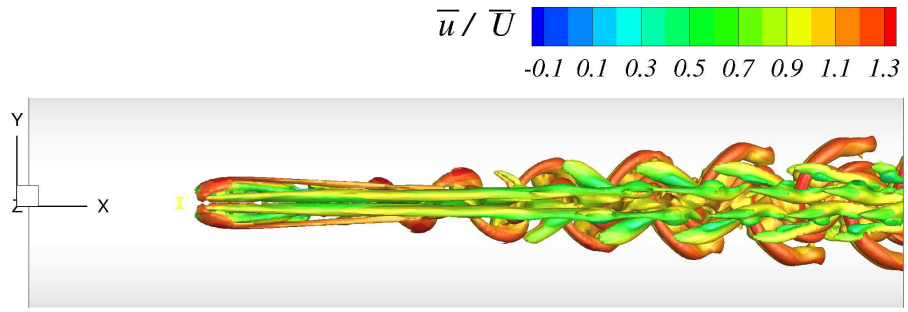

(a) $z = 0$ plane

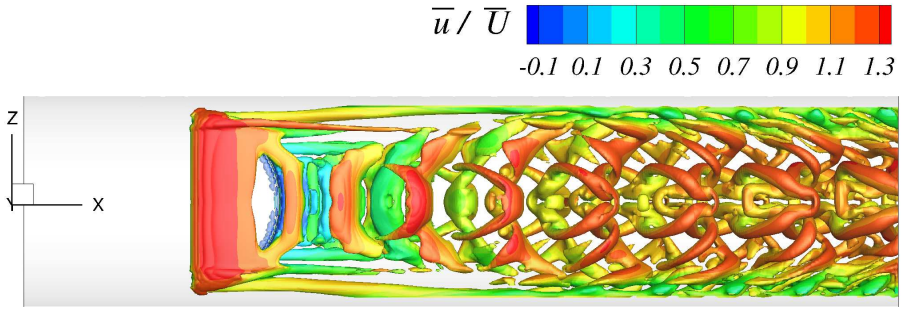

(b) $y = 0$ plane

Figure 5.6. Instantaneous iso-surfaces of $\lambda_2 = -2$ with axial velocity as color code shown in different views (a) $z = 0$ plane (b) $y = 0$ plane, in the steady inflow to the BMHV at the maximum opening phase in a model aorta.

peak velocity in the central jet region reduced to $2\overline{U}$ at peak velocity point $Q2$ and a reverse flow velocity as high as $-1.6\overline{U}$ are noted in the same region at the end of the systole. The average velocity and the profiles towards the distal end at $x/d = 4.0$ look very similar to those observed at locations before the leaflets at $x/d = -0.5$ at any given phase. The axial velocity profiles on $y = 0$ are shown in Figure 5.8 at the same phases. Similar to the previous observations, we note that the peak velocity occurs at point $Q1$ and the distal end velocity profiles look very similar to the ones before the leaflet location. All the velocity profiles on $y = 0$ plane at phases $Q2$ and $Q3$ show forward velocity whereas at other phase instants reverse flow is observed mainly towards the trailing edge of the leaflets at location $x/d = 0.5$ and in the immediate downstream at location $x/d = 1.0$.

Next, we investigate the *tke* production in the model aorta under pulsatile inflow conditions with imposed kinematics of the leaflets. The normalized *tke* profiles are shown in Figure 5.9 on the $z = 0$ plane at indicated x/d locations along the axis of the model aorta. We can see from this figure that the *tke* profiles reach a maximum value of around 12.5%. The profiles start increasing beginning at the trailing edge of the leaflets at $x/d = 0.5$ reaching a maximum values at the location $x/d = 1.0$ and there after they start decreasing reaching close to zero values by $x/d = 3.0$. The same phenomenon is observed with the profiles plotted on $y = 0$ plane in Figure 5.10. This behavior is quite different from that one observed in the case of the stationary BMHV at the maximum velocity condition. In the stationary case it was noted that the *tke* values reached a maximum value at the location $x/d = 1.5$ with close to 5% intensity, however they did not decay to zero values even close to the distal end.

To further understand the vorticity dynamics in the model aorta with moving leaflets. The contours of normalized vorticity magnitude are shown on $z = 0$ plane and $y = 0$ plane in Figure 5.11 and Figure 5.12 respectively. As we can see from phase $Q2$ the central jet with two shear layers from each side of the bottom of the leaflets does not have any undulations. There are two shear layers that get formed from the trailing edge of the leaflets and these get formed during the acceleration phase as can

be noticed from phases $Q1$ and $Q2$ in the $z = 0$ plane in Figure 5.11. The same time frames in Figure 5.12 shows the span wise extent of the vorticity production in the central jet region. As the leaflets retract back in the deceleration phase small undulations are noticed in the vorticity contours in the central jet region at time instant $Q3$ as seen in the $z = 0$ plane contours. The shear layers that got formed from the trailing edge of the leaflets gets shed from the edges and start interacting with the wall shear layers as seen in frame (f) at phase $Q3$ in Figure 5.12. This separation of shear layer is also noticed in the central plane on $y = 0$ plane at the same phase as seen in frame (f) in Figure 5.12. As the leaflets return to the fully closed position at the end of the systole many undulations are seen in both the central jet vorticity as well in the shear layers that got formed at the trailing edges of the leaflets. The location of the interaction of the previously shed vortices with the wall shear layers seems to be stationary between the phases at $Q3$ and $Q4$. The same observation of nearly stationary vorticity distribution is noticed on the $y = 0$ plane. Towards mid diastole, we notice that the intensity of vorticity decreases as can be noticed from frames (j) in both $z = 0$ and $y = 0$ planes. However, a small region of vorticity production is seen ahead of the leaflets in the central jet region in the same frame in Figure 5.11, this is attributed to the back flow that takes place during the diastolic phase of the flow. The same can be noticed in the $y = 0$ plane in frame (j) with non-zero vorticity values seen to the left of $x/d = 0$.

The coherent vortical structures that get generated in this flow are visualized using the λ_2 criterion of Jeong & Hussain [56]. The iso-surface of $\lambda_2 = -2$ are shown in Figure 5.13 at the indicated phase instants. Unlike the vortical structures noticed in the stationary BMHV case, here we notice many small scale structures in the downstream of the leaflets. In the stationary BMHV case, the vortical structures were a consequence of the vortex shedding and linear growth of large structures is noted. However, in the physiologically relevant pulsatile case with moving leaflets we notice that the vortical structures and the *tke* levels decays quickly by a downstream location of $x/d = 2.0$. Vortical structures being separated from the leaflets and

getting shed can be noticed from frames $Q2$ and $Q3$ in this figure. Maximum velocity is seen in the gaps between the leaflets and model aorta at phase $Q2$. Further, the back flow of the central jet during diastole is seen at phase $Q5$ in this figure.

5.7 Discussion and Conclusions

In the present work, we performed both stationary and moving leaflet simulations under steady and pulsatile inflow conditions. The stationary simulations correspond to the peak velocity condition in the pulsatile inflow simulation. It is observed that the stationary leaflet with steady inflow condition yields strikingly different results when compared with the same point in the pulsatile inflow conditions. In the stationary leaflet simulation periodic vortex shedding similar to von Karman vortex street was observed with both the leaflets acting as a single body. The *tke* production took place downstream of the leaflets around $x/d = 1.0$ reaching a peak value at $x/d = 1.5$ and there after they decreased as we move downstream. The *tke* values did not reach non zero values even close to the exit of the domain. The educed vortical structures also showed large vortices shed both from the top and bottom leaflets. There were long vortical structures that were observed that emanated from the sides of the leaflets. Downstream these vortices interacted with those that were shed form top and bottom leaflets.

The pulsatile inflow simulation with imposed kinematics of the leaflets showed high velocities in the central jet region and the velocity profiles at the distal end represented close to the corresponding profiles at a location before the leaflets. Reverse flow was observed in the central jet region at the end of the systolic phase. The *tke* production started right from the edges of the leaflets and decayed to zero values by a downstream location of $x/d = 3.0$. During deceleration phase undulations in the central jet shear layers were noted together with the shear layers there were shed from the leaflet edges interacting with the wall shear layers. Small coherent structures were found in the immediate downstream of the leaflets and the reverse flow generated from the central

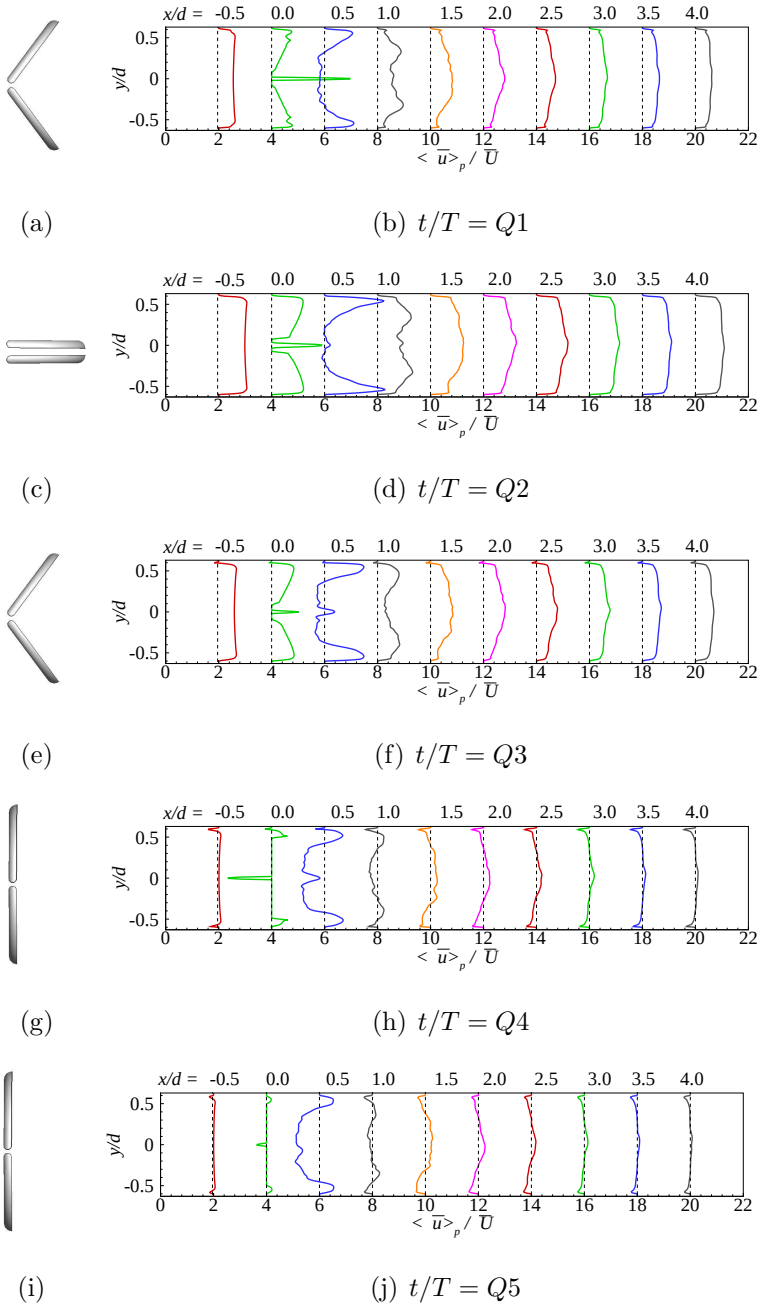

Figure 5.7. Ensemble averaged axial velocity profiles on $z = 0$ plane, at indicated locations and at indicated time instants in the pulsatile inflow to the BMHV in a model aorta. The corresponding phase of the leaflets is shown to the left of the profiles for clarity which are otherwise located at $x/d = 0$. Note the scale on the x and y axes is not the same.

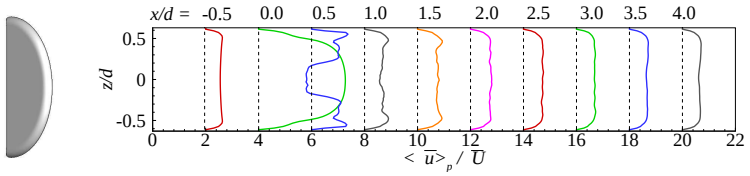

(a) (b) $t/T = Q1$

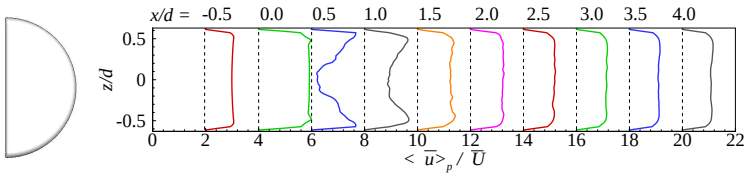

(c) (d) $t/T = Q2$

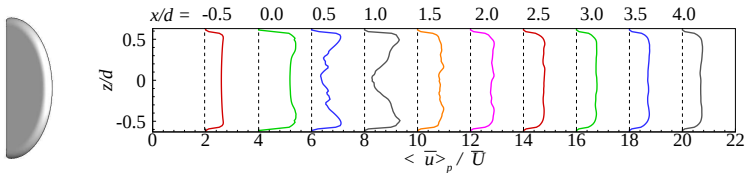

(e) (f) $t/T = Q3$

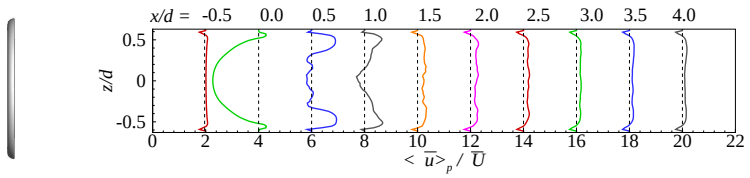

(g) (h) $t/T = Q4$

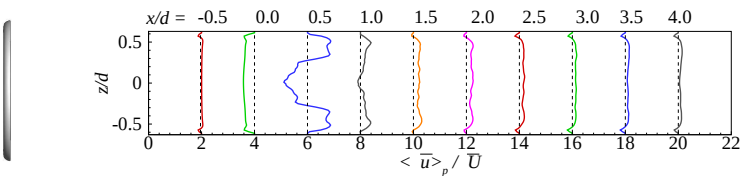

(i) (j) $t/T = Q5$

Figure 5.8. Ensemble averaged axial velocity profiles on $y = 0$ plane, at indicated locations and at indicated time instants in the pulsatile inflow to the BMHV in a model aorta. Note the scale on the x and z axes is not the same.

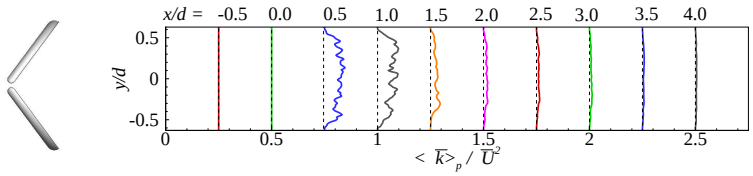

(a) (b) $t/T = Q1$

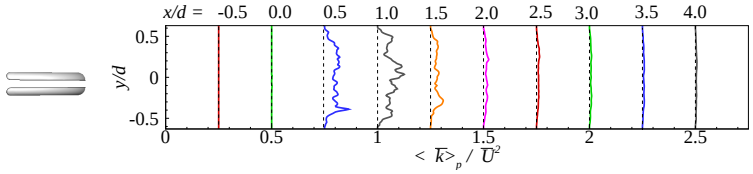

(c) (d) $t/T = Q2$

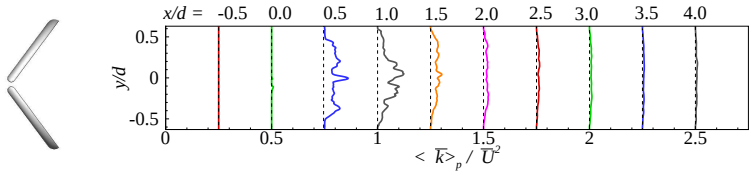

(e) (f) $t/T = Q3$

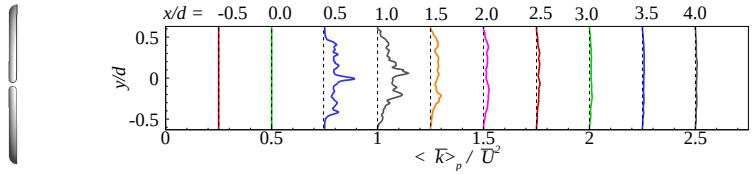

(g) (h) $t/T = Q4$

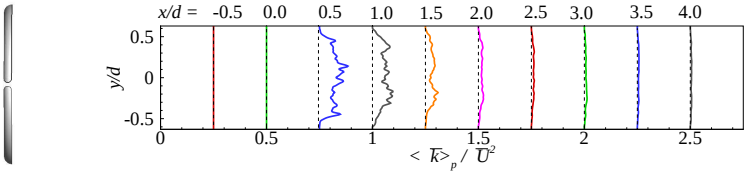

(i) (j) $t/T = Q5$

Figure 5.9. Ensemble averaged turbulent kinetic energy profiles on $z = 0$ plane, at indicated locations and at indicated time instants in the pulsatile inflow to the BMHV in a model aorta. The corresponding phase of the leaflets is shown to the left of the profiles for clarity which are otherwise located at $x/d = 0$. Note the scale on the x and y axes is not the same.

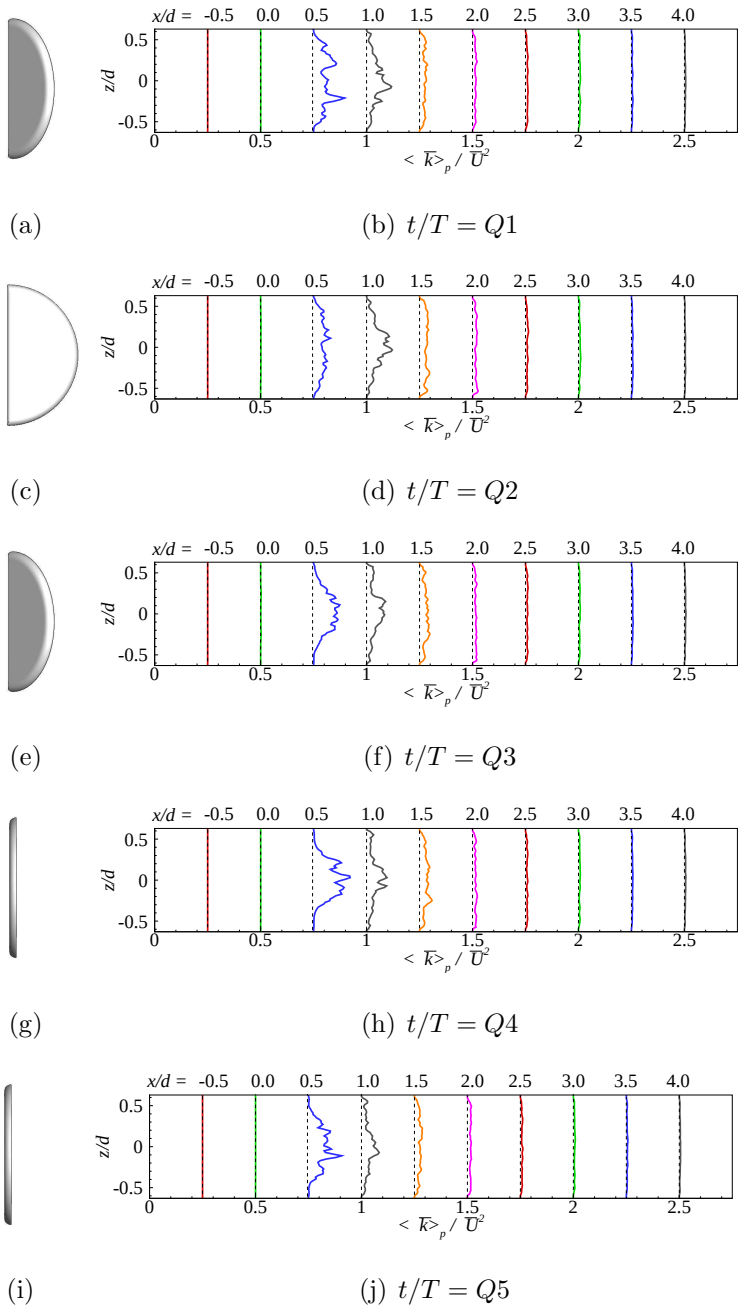

Figure 5.10. Ensemble averaged turbulent kinetic energy profiles on $y = 0$ plane, at indicated locations and at indicated time instants in the pulsatile inflow to the BMHV in a model aorta. The corresponding phase of the leaflets is shown to the left of the profiles for clarity which are otherwise located at $x/d = 0$. Note the scale on the x and z axes is not the same.

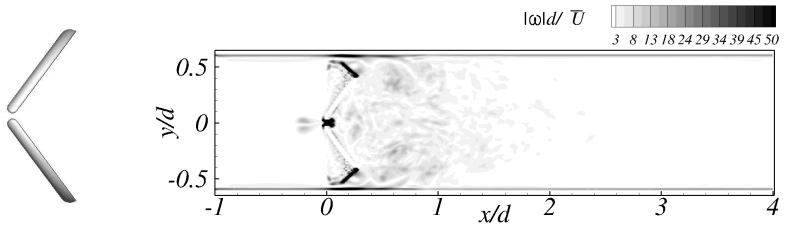

(a) (b) $t/T = Q1$

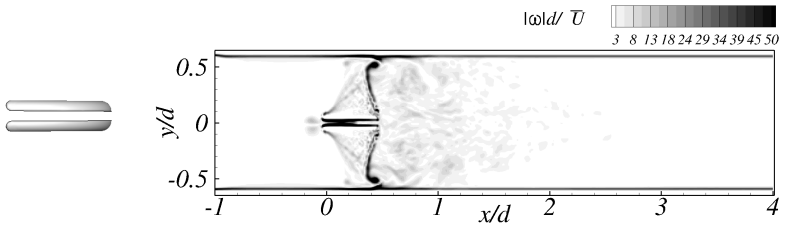

(c) (d) $t/T = Q2$

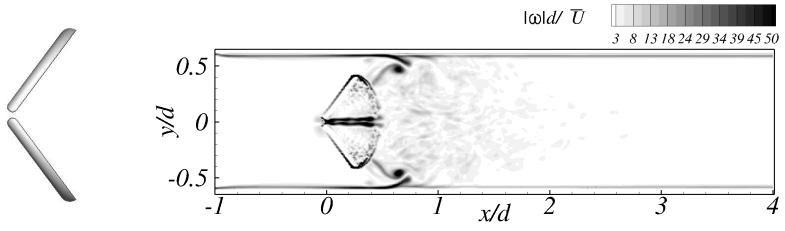

(e) (f) $t/T = Q3$

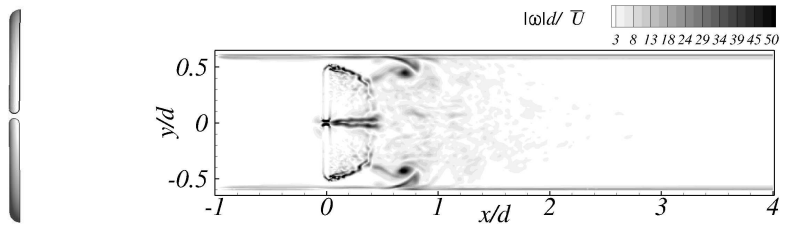

(g) (h) $t/T = Q4$

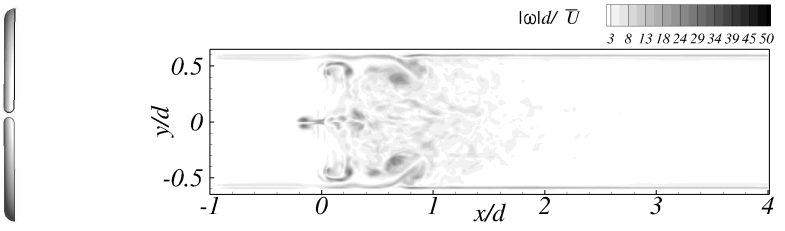

(i) (j) $t/T = Q5$

Figure 5.11. Contours of normalized and ensemble averaged vorticity magnitude on $z = 0$ plane, at indicated time instants in the pulsatile inflow to the BMHV in a model aorta.

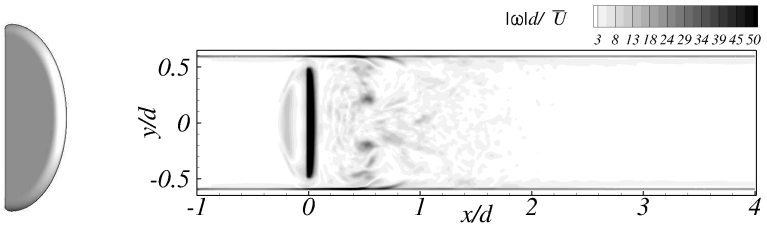

(a) (b) $t/T = Q1$

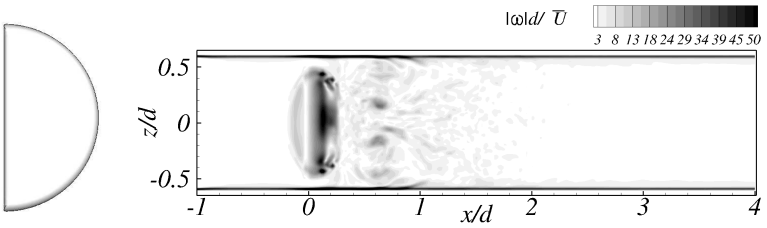

(c) (d) $t/T = Q2$

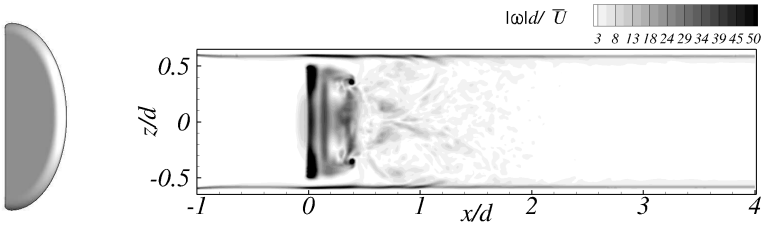

(e) (f) $t/T = Q3$

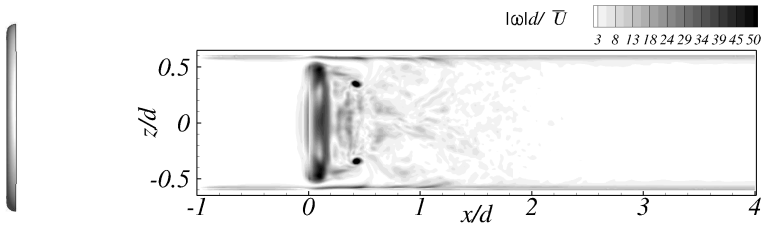

(g) (h) $t/T = Q4$

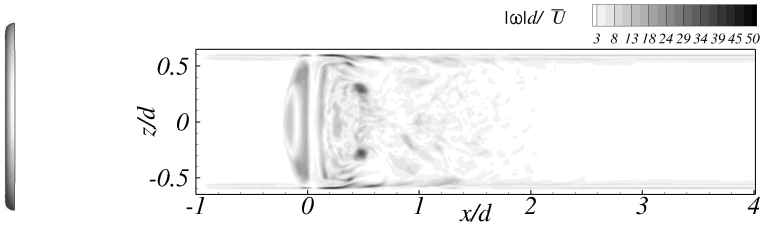

(i) (j) $t/T = Q5$

Figure 5.12. Contours of normalized and ensemble averaged vorticity magnitude on $y = 0$ plane, at indicated time instants in the pulsatile inflow to the BMHV in a model aorta.

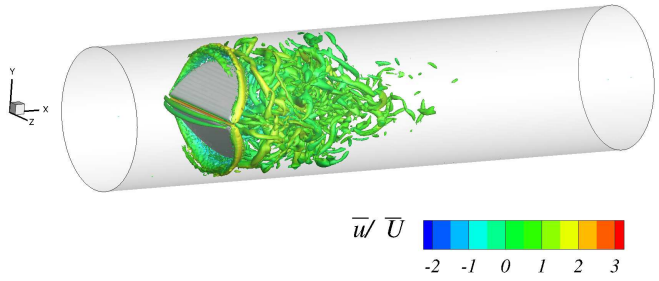

(a) $t/T = Q1$

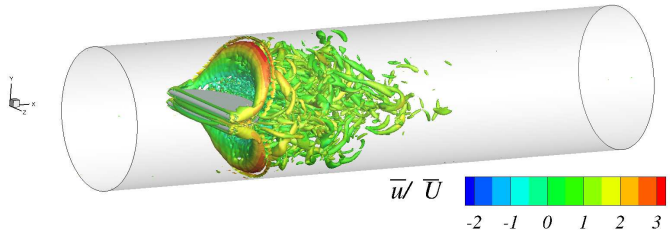

(b) $t/T = Q2$

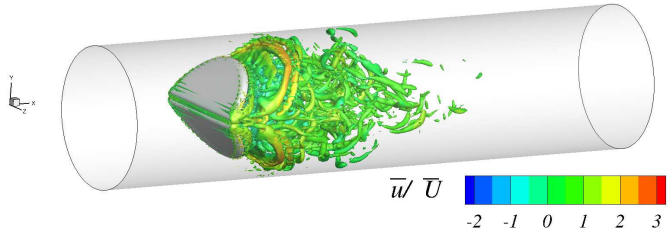

(c) $t/T = Q3$

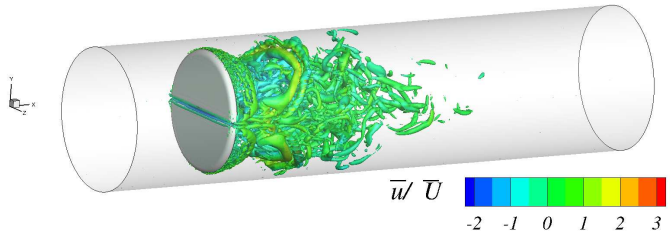

(d) $t/T = Q4$

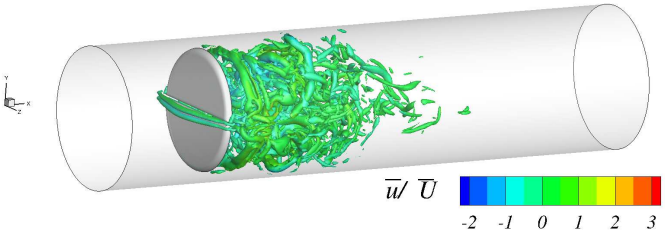

(e) $t/T = Q5$

Figure 5.13. Iso surfaces of λ_2 criterion colored by instantaneous axial velocity at indicated time instants in the pulsatile inflow to the BMHV in a model aorta.

jet region in the diastolic phase resulted in two long vortical structures that move ahead into the gap between the inlet and leaflets.

6. CONCLUSIONS AND FUTURE WORK

6.1 Conclusions

The following conclusions can be arrived at from the present research work within the limits of the assumptions made for each of the simulations performed. The developed WenoHemo solver is applied to study two clinically relevant bio-fluid dynamics problems. Results obtained from TAA and TASG indicate that, turbulence levels are lower in the TASG configuration compared to the pathological TAA configuration. Well developed turbulence is detected from the energy spectrum in the case of TAA, whereas TASG only shows vortex shedding. Analysis of WSS and SWSSG indicates that although WSS levels remains almost same between the TAA and TASG configurations, the SWSSG levels are large in the regions close the inlet and in the neighborhood of the aneurysm whereas large SWSSG values are noted only in the inlet region in the case of TASG. This indicates that TAA configuration is more predisposed to the formation of an aneurysm in the aortic arch region.

The study of blood flow over BMHV configuration placed a model aorta reveals totally different results between the stationary leaflet configuration and the moving leaflets configuration. In the case of moving leaflets the kinematics are imposed and the turbulence levels increase behind the leaflets and quickly damp within one diameter of the leaflets. Complex vortical structures are produced behind the leaflets that disintegrate into small scale structures during the deceleration phase that need to be considered in the design of the mechanical heart valves for reliability and to reduce post surgical complications.

6.2 Future Work

6.2.1 Solver Development

The following solver improvements could be undertaken in future.

- The present solver, WenoHemo, currently can only handle uniform mesh sizes. Future work needs to focus on implementing Adaptive Mesh Refinement (AMR) using which the mesh can be refined in regions where it is necessary without a need to refine the mesh everywhere.

- The file input/output is presently supported using PLOT3D format. However, there is an inherent limitation to use this format with a large number of processors. As the file input/output is performed through a serial mode, all the processors will send their own data to the host process which writes the data files. This behavior can be improved by using HDF5 file format which allows for parallel writing of files.

6.2.2 Simulations of TAA/TASG

- A non-Newtonian model could be implemented in the using which the differences in results obtained between Newtonian and non-Newtonian models can be delineated.

- The walls of the aorta are considered to be rigid. This is severe restriction at least in some locations of the aorta which is not pathologically affected. Future studies can consider implementing a Fluid-Structure Interaction (FSI) model to incorporate the aortic wall deformations in the simulations.

6.2.3 Simulations of BMHV

- Fully coupled fluid structured interaction of the valve leaflets with the blood flow
- Inclusion of non-Newtonian fluid model to evaluate the effect during valve opening and closure phases in which time blood flow takes places through narrow gaps causing high shear rates.
- Inclusion of sinus region near the valve placement and realistic aorta geometry instead of the model aorta considered in the present work.

LIST OF REFERENCES

LIST OF REFERENCES

[1] S. Aggarwal, A. Qamar, V. Sharma, and A. Sharma. Abdominal aortic aneurysm: A comprehensive review. *Experimental and Clinical Cardiology*, 16(1):11–15, 2011.

[2] M. Midulla, R. Moreno, A. Baali, M. Chau, A. Negre-Salvayre, F. Nicoud, J. P. Pruvo, S. Haulon, and H. Rousseau. Haemodynamic imaging of thoracic stent-grafts by computational fluid dynamics (cfd): presentation of a patient-specific method combining magnetic resonance imaging and numerical simulations. *European radiology*, pages 1–9, 2012.

[3] D. N. Ku. Blood Flow in Arteries. *Annual Review of Fluid Mechanics*, 29(1):399–434, 1997.

[4] L. Formaggia, A. Quarteroni, and A. Veneziani. *Cardiovascular Mathematics: Modeling and simulation of the circulatory system*, volume 1. Springer, 2009.

[5] I. G. Currie. *Fundamental mechanics of fluids*. CRC Press, 2012.

[6] C. L. Asbury, J. W. Ruberti, E. I. Bluth, and R. A. Peattie. Experimental investigation of steady flow in rigid models of abdominal aortic aneurysms. *Annals of Biomedical Engineering*, 23(1):29–39, 1995.

[7] L. Morris, P. Delassus, a. Callanan, M. Walsh, F. Wallis, P. Grace, and T. McGloughlin. 3-D Numerical Simulation of Blood Flow Through Models of the Human Aorta. *Journal of Biomechanical Engineering*, 127(5):767, 2005.

[8] A. V. Salsac, S. R. Sparks, J. M. Chomaz, and J. C. Lasheras. Evolution of the wall shear stresses during the progressive enlargement of symmetric abdominal aortic aneurysms. *Journal of Fluid Mechanics*, 560(1):19–51, 2006.

[9] S. S. Varghese, S. H. Frankel, and P. F. Fischer. Direct numerical simulation of stenotic flows. Part 1. Steady flow. *Journal of Fluid Mechanics*, 582:253, June 2007.

[10] S. S. Varghese, S. H. Frankel, and P. F. Fischer. Direct numerical simulation of stenotic flows. Part 2. Pulsatile flow. *Journal of Fluid Mechanics*, 582(2007):281, June 2007.

[11] J. Lantz and M. Karlsson. Large eddy simulation of LDL surface concentration in a subject specific human aorta. *Journal of Biomechanics*, 45(3):537–42, 2012.

[12] J. Biasetti, F. Hussain, and T. C. Gasser. Blood flow and coherent vortices in the normal and aneurysmatic aortas: a fluid dynamical approach to intra-luminal thrombus formation. *Journal of The Royal Society Interface*, 8(63):1449–1461, 2011.

[13] R. Mittal, S. P. Simmons, and F. Najjar. Numerical study of pulsatile flow in a constricted channel. *Journal of Fluid Mechanics*, 485:337–378, 4 2003.

[14] D. A. Shetty, T. C. Fisher, A. R. Chunekar, and S. H. Frankel. High-order incompressible large-eddy simulation of fully inhomogeneous turbulent flows. *Journal of Computational Physics*, 229(23):8802–8822, November 2010.

[15] G. Jiang and C. Shu. Efficient implementation of weighted ENO schemes. *Journal of Computational Physics*, 126(1):202–228, 1995.

[16] Y. Morinishi, T. S. Lund, O. V. Vasilyev, and P. Moin. Fully Conservative Higher Order Finite Difference Schemes for Incompressible Flow. *Journal of Computational Physics*, 143(1):90–124, 1998.

[17] D. A. Shetty, J. Shen, A. J. Chandy, and S. H. Frankel. A pressure-correction scheme for rotational navier-stokes equations and its application to rotating turbulent flows. 2011.

[18] R. D. Falgout and U. M. Yang. hypre: A library of high performance preconditioners, 2002.

[19] J. Smagorinsky. General circulation experiments with the primitive equations. *Monthly Weather Review*, 91(3):99–164, 1963.

[20] A. W. Vreman. An eddy-viscosity subgrid-scale model for turbulent shear flow: Algebraic theory and applications. *Physics of Fluids*, 16(10):3670, 2004.

[21] J. Zhang and T. L. Jackson. A high-order incompressible flow solver with WENO. *Journal of Computational Physics*, 228(7):2426–2442, 2009.

[22] B. Gustafsson, H.-O. Kreiss, and J. Oliger. *Time dependent problems and difference methods*, volume 67. Wiley New York, 1995.

[23] C. Kleinstreuer, Z. Li, and M. A. Farber. Fluid-structure interaction analyses of stented abdominal aortic aneurysms. *Annual review of biomedical engineering*, 9:169–204, January 2007.

[24] Y. Delorme, K. Anupindi, A.E. Kerlo, D. Shetty, M. Rodefeld, J. Chen, and S. Frankel. Large eddy simulation of powered fontan hemodynamics. *Journal of Biomechanics*, 46(2):408 – 422, 2013. Special Issue: Biofluid Mechanics.

[25] C. S. Peskin. Flow patterns around heart valves: A numerical method. *Journal of Computational Physics*, 10(2):252–271, 1972.

[26] R. Mittal, H. Dong, M. Bozkurttas, F. M. Najjar, A. Vargas, and A. Von Loebbecke. A Versatile Sharp Interface Immersed Boundary Method for Incompressible Flows With Complex Boundaries. *Journal of Computational Physics*, 227(10):4825–4852, 2008.

[27] A. Gilmanov and F. Sotiropoulos. A hybrid Cartesian/immersed boundary method for simulating flows with 3D, geometrically complex, moving bodies. *Journal of Computational Physics*, 207(2):457–492, 2005.

[28] J. Choi, R. C. Oberoi, J. R. Edwards, and J. A. Rosati. An immersed boundary method for complex incompressible flows. *Journal of Computational Physics*, 224(2):757–784, June 2007.

[29] C. S. Peskin and D. M. McQueen. A three-dimensional computational method for blood flow in the heart I. Immersed elastic fibers in a viscous incompressible fluid. *Journal of Computational Physics*, 37245:372–405, 1989.

[30] T. B. Le and F. Sotiropoulos. Fluid structure interaction of an aortic heart valve prosthesis driven by an animated anatomic left ventricle. *Journal of Computational Physics*, 2012.

[31] A. Posa, A. Lippolis, R. Verzicco, and E. Balaras. Large-eddy simulations in mixed-flow pumps using an immersed-boundary method. *Computers & Fluids*, 47(1):33–43, August 2011.

[32] R. Mittal and G. Iaccarino. Immersed Boundary Methods. *Annual Review of Fluid Mechanics*, 37(1):239–261, 2005.

[33] C. S. Peskin. The immersed boundary method. *Acta Numerica*, 11(1):479–517, 2003.

[34] T. Colonius and K. Taira. A fast immersed boundary method using a nullspace approach and multi-domain far-field boundary conditions. *Computer Methods in Applied Mechanics and Engineering*, 197(25-28):2131–2146, April 2008.

[35] A. Pinelli, I. Z. Naqavi, U. Piomelli, and J. Favier. Immersed-boundary methods for general finite-difference and finite-volume NavierStokes solvers. *Journal of Computational Physics*, 229(24):9073–9091, December 2010.

[36] M. Vanella, P. Rabenold, and E. Balaras. A direct-forcing embedded-boundary method with adaptive mesh refinement for fluidstructure interaction problems. *Journal of Computational Physics*, 229(18):6427–6449, 2010.

[37] B. E. Griffith, R. D. Hornung, D. M. Mcqueen, and C. S. Peskin. An adaptive, formally second order accurate version of the immersed boundary method. *Journal of Computational Physics*, 223(1):10–49, 2007.

[38] K. Yokoi, F. Xiao, H. Liu, and K. Fukasaku. Three-dimensional numerical simulation of flows with complex geometries in a regular Cartesian grid and its application to blood flow in cerebral artery with multiple aneurysms. *Journal of Computational Physics*, 202(1):1–19, January 2005.

[39] D. de Zélicourt, L. Ge, C. Wang, F. Sotiropoulos, A. Gilmanov, and A. Yoganathan. Flow simulations in arbitrarily complex cardiovascular anatomies An unstructured Cartesian grid approach. *Computers & Fluids*, 38(9):1749–1762, October 2009.

[40] W. K. Liu, S. Jun, and Y. F. Zhang. Reproducing kernel particle methods. *International Journal for Numerical Methods in Fluids*, 20(8-9):1081–1106, 1995.

[41] A. L. F. Lima E Silva, A. Silveira-Neto, and J. J. R. Damasceno. Numerical simulation of two-dimensional flows over a circular cylinder using the immersed boundary method. *Journal of Computational Physics*, 189(2):351–370, August 2003.

[42] A. Mark and B. Vanwachem. Derivation and validation of a novel implicit second-order accurate immersed boundary method. *Journal of Computational Physics*, 227(13):6660–6680, June 2008.

[43] A. Chaudhuri, A. Hadjadj, and A. Chinnayya. On the use of immersed boundary methods for shock/obstacle interactions. *Journal of Computational Physics*, 230(5):1731–1748, March 2011.

[44] M. B. Kennel. KDTREE 2: Fortran 95 and C++ software to efficiently search for near neighbors in a multi-dimensional Euclidean space. *Arxiv preprint physics/0408067*, 2004.

[45] R. D. Falgout and J. E. Jones. Multigrid on Massively Parallel Architectures. In E Dick, K Riemslagh, and J Vierendeels, editors, *Multigrid Methods VI*, volume 14 of *Lecture Notes in Computational Science and Engineering*, pages 101–107. Springer, 2000.

[46] S. F. Ashby and R. D. Falgout. A parallel multigrid preconditioned conjugate gradient algorithm for groundwater flow simulations. *Nuclear Science and Engineering*, 94551(1):145–159, 1996.

[47] T. A. Johnson and V. C. Patel. Flow past a sphere up to a Reynolds number of 300. *Journal of Fluid Mechanics*, 378(-1):19–70, 1999.

[48] N. Tylli, L. Kaiktsis, and B. Ineichen. Sidewall effects in flow over a backward-facing step: Experiments and numerical simulations. *Physics of Fluids*, 14(11):3835, 2002.

[49] R. Wille and H. Fernholz. Report on the first European Mechanics Colloquium, on the Coanda effect. *Journal of Fluid Mechanics*, 23(4):801–819, 1965.

[50] I. Reba. Applications of the Coanda effect. *Scientific American*, 214:84–92, 1966.

[51] R. Mittal, S. P. Simmons, and H. S. Udaykumar. Application of large-eddy simulation to the study of pulsatile flow in a modeled arterial stenosis. *Journal of Biomechanical Engineering*, 123(4):325–332, 2001.

[52] M. M. Molla, B.-C. Wang, and D. C. S. Kuhn. Numerical study of pulsatile channel flows undergoing transition triggered by a modelled stenosis. *Physics of Fluids*, 24:121901, 2012.

[53] V. Aeschlimann, S. Barre, and S. Legoupil. X-ray attenuation measurements in a cavitating mixing layer for instantaneous two-dimensional void ratio determination. *Physics of Fluids*, 23(5):055101, 2011.

[54] C. D. Winant and F. K. Browand. Vortex pairing : the mechanism of turbulent mixing-layer growth at moderate Reynolds number. *Journal of Fluid Mechanics*, 63(02):237–255, 1974.

[55] V. Aeschlimann, S. Barre, and H. Djeridi. Velocity field analysis in an experimental cavitating mixing layer. *Physics of Fluids*, 23(5):055105, 2011.

[56] J. Jeong and F. Hussain. On the identification of a vortex. *Journal of Fluid Mechanics*, 285(-1):69–94, 1995.

[57] B. R. Shin, S. Yamamoto, and X. Yuan. Application of Preconditioning Method to Gas-Liquid Two-Phase Flow Computations. *Journal of Fluids Engineering*, 126(4):605, 2004.

[58] N. Dittakavi, A. Chunekar, and S. Frankel. Large Eddy Simulation of Turbulent-Cavitation Interactions in a Venturi Nozzle. *Journal of Fluids Engineering*, 132(12):121301, 2010.

[59] I. Senocak and W. Shyy. A Pressure-Based Method for Turbulent Cavitating Flow Computations. *Journal of Computational Physics*, 176(2):363–383, 2002.

[60] C. J. Lu, Y. S. He, X. Chen, and Y. Chen. Numerical and Experimental Research on Cavitating Flows. In *Fifth International Conference on Fluid Mechanics*, pages 45–52. Tsinghua University Press & Springer, 2007.

[61] V. Srinivasan, A. Salazar, and K. Saito. Numerical simulation of cavitation dynamics using a cavitation-induced-momentum-defect (CIMD) correction approach. *Applied Mathematical Modelling*, 33(3):1529–1559, 2009.

[62] R. E. Bensow and G. Bark. Implicit les predictions of the cavitating flow on a propeller. *Journal of fluids engineering*, 132(4), 2010.

[63] R. F. Kunz, D. A. Boger, D. R. Stinebring, S. Chyczewski, J. W. Lindau, H. J. Gibeling, S. Venkateswaran, and T. R. Govindan. A preconditioned Navier-Stokes method for two-phase flows with application to cavitation prediction. *Computers & Fluids*, 29(8):849–875, 2000.

[64] J. C. Lasheras. The Biomechanics of Arterial Aneurysms. *Annual Review of Fluid Mechanics*, 39(1):293–319, January 2007.

[65] P. Welch. The use of fast Fourier transform for the estimation of power spectra: A method based on time averaging over short, modified periodograms. *IEEE Transactions on Audio and Electroacoustics*, 15(2):70–73, 1967.

[66] H. Tennekes and J. L. Lumley. *A first course in turbulence*. MIT press, 1972.

[67] D. C. Wilcox. *Turbulence modeling for CFD*. DCW Industries, 2nd edition, 2000.

[68] S. B. Pope. *Turbulent flows*. Cambridge university press, 2000.

[69] B. M. Kim and W. H. Corcoran. Experimental measurements of turbulence spectra distal to stenoses. *Journal of Biomechanics*, 7(4):335–342, 1974.

[70] P. C. Lu, D. R. Gross, and N. H. C. Hwang. Intravascular pressure and velocity fluctuations in pulmonic arterial stenosis. *Journal of Biomechanics*, 13(3):291–300, 1980.

[71] A. P. Yoganathan, Z. He, and S. C. Jones. Fluid mechanics of heart valves. *Annu. Rev. Biomed. Eng.*, 6:331–362, 2004.

[72] L. P. Dasi, H. A. Simon, P. Sucosky, and A. P. Yoganathan. Fluid mechanics of artificial heart valves. *Clinical and Experimental Pharmacology and Physiology*, 36(2):225–237, 2009.

[73] K. B. Manning, V. Kini, A. A. Fontaine, S. Deutsch, and J. M. Tarbell. Regurgitant flow field characteristics of the st. jude bileaflet mechanical heart valve under physiologic pulsatile flow using particle image velocimetry. *Artificial organs*, 27(9):840–846, 2003.

[74] H. A. Simon, H.-L. Leo, J. Carberry, and A. P. Yoganathan. Comparison of the hinge flow fields of two bileaflet mechanical heart valves under aortic and mitral conditions. *Annals of biomedical engineering*, 32(12):1607–1617, 2004.

[75] D. Bluestein. Research approaches for studying flow-induced thromboembolic complications in blood recirculating devices. *Expert review of medical devices*, 1(1):65–80, 2004.

[76] Ch. Brücker, U. Steinseifer, W. Schröder, and H. Reul. Unsteady flow through a new mechanical heart valve prosthesis analysed by digital particle image velocimetry. *Measurement Science and Technology*, 13(7):1043, 2002.

[77] Y. T. Chew, T. C. Chew, and H. T. Low. Particle image velocimetry in the investigation of flow past artificial heart valves. *Annals of biomedical engineering*, 22(3):307–318, 1994.

[78] H. L. Leo, L. P. Dasi, J. Carberry, H. A. Simon, and A. P. Yoganathan. Fluid dynamic assessment of three polymeric heart valves using particle image velocimetry. *Annals of biomedical engineering*, 34(6):936–952, 2006.

[79] M. Krafczyk, M. Cerrolaza, M. Schulz, and E. Rank. Analysis of 3d transient blood flow passing through an artificial aortic valve by lattice boltzmann methods. *Journal of Biomechanics*, 31(5):453–462, 1998.

[80] M. Grigioni, C. Daniele, C. Del Gaudio, U. Morbiducci, A. Balducci, G. D'Avenio, and V. Barbaro. Three-dimensional numeric simulation of flow through an aortic bileaflet valve in a realistic model of aortic root. *ASAIO journal*, 51(3):176–183, 2005.

[81] M. D. De Tullio, A. Cristallo, E. Balaras, and R. Verzicco. Direct numerical simulation of the pulsatile flow through an aortic bileaflet mechanical heart valve. *Journal of Fluid Mechanics*, 622(-1):259, 2009.

[82] L. P. Dasi, L. Ge, H. A. Simon, F. Sotiropoulos, and A. P. Yoganathan. Vorticity dynamics of a bileaflet mechanical heart valve in an axisymmetric aorta. *Physics of Fluids*, 19:067105, 2007.

[83] L. Ge, L. P. Dasi, F. Sotiropoulos, and A. P. Yoganathan. Characterization of hemodynamic forces induced by mechanical heart valves: Reynolds vs. viscous stresses. *Annals of Biomedical Engineering*, 36(2):276–297, 2008.

[84] V.-T. Nguyen, Y. H. Kuan, P.-Y. Chen, L. Ge, F. Sotiropoulos, A. P. Yoganathan, and H. L. Leo. Experimentally Validated Hemodynamics Simulations of Mechanical Heart Valves in Three Dimensions. *Cardiovascular Engineering and Technology*, 3(1):88–100, 2012.

[85] R. Cheng, Y. G. Lai, and K. B. Chandran. Three-dimensional fluid-structure interaction simulation of bileaflet mechanical heart valve flow dynamics. *Annals of Biomedical Engineering*, 32(11):1471–1483, 2004.

[86] K. Dumont, J. Vierendeels, R. Kaminsky, G. Van Nooten, P. Verdonck, and D. Bluestein. Comparison of the hemodynamic and thrombogenic performance of two bileaflet mechanical heart valves using a cfd/fsi model. *Journal of Biomechanical Engineering*, 129(4):558–565, 2007.

[87] D. Bluestein, E. Rambod, and M. Gharib. Vortex shedding as a mechanism for free emboli formation in mechanical heart valves. *Journal of Biomechanical Engineering*, 122(2):125–134, 2000.

[88] S. Krishnan, H. S. Udaykumar, J. S. Marshall, and K. B. Chandran. Two-dimensional dynamic simulation of platelet activation during mechanical heart valve closure. *Annals of Biomedical Engineering*, 34(10):1519–1534, 2006.

[89] V. Govindarajan, H. S. Udaykumar, and K. B. Chandran. Two-dimensional simulation of flow and platelet dynamics in the hinge region of a mechanical heart valve. *Journal of Biomechanical Engineering*, 131(3):031002, 2009.

[90] Y. Alemu, G. Girdhar, M. Xenos, J. Sheriff, J. Jesty, S. Einav, and D. Bluestein. Design optimization of a mechanical heart valve for reducing valve thrombogenicity-a case study with ats valve. *ASAIO Journal*, 56(5):389–396, 2010.

[91] A. L Fogelson and R. D. Guy. Platelet–wall interactions in continuum models of platelet thrombosis: formulation and numerical solution. *Mathematical Medicine and Biology*, 21(4):293–334, 2004.

[92] F. E. Deuvaert, J. Devriendt, J. Massaut, G. Van Nooten, J. De Paepe, and G. Primo. Leaflet escape of a mitral duromedics prosthesis. case report. *Acta chirurgica Belgica*, 89(1):15, 1989.

[93] J. Alvarez and C. W. Deal. Leaflet escape from a Duromedics valve. *The Journal of Thoracic and Cardiovascular Surgery*, 99(2):372, 1990.

[94] K. Sudo, N. Sasagawa, H. Ide, M. Nunokawa, T. Fujiki, and K. Tonari. Late leaflet fracture and embolization of a Duromedics mitral prosthesis. *The Japanese Journal of Thoracic and Cardiovascular Surgery*, 48(8):520–523, 2000.

[95] F. J. Baumgartner, A. I. Munro, and W. R. Jamieson. Fracture embolization of a Duromedics mitral prosthesis. *Texas Heart Institute Journal*, 24(2):122, 1997.

[96] E. Tatou, M. Saleh, J. C. Eicher, R. Brenot, and M. David. Fracture-embolization of Duromedics valve prosthesis and microscopic uncommon lesions. *The Annals of Thoracic Surgery*, 71(4):1366–1369, 2001.

[97] K. Yamazaki, K. Nishimura, A. Iwakura, K. Uehara, T. Okada, and T. Sugita. Fracture Embolization of an Edwards-Duromedics Valve with Asymmetrical Closure. *Asian Cardiovascular and Thoracic Annals*, 16(3):242–245, 2008.

[98] D. Kim, S. S. Hun, I.-J. Cho, C.-Y. Shim, J.-W. Ha, N. Chung, H. C. Ju, J. W. Sohn, and G.-R. Hong. Prosthetic Mitral Valve Leaflet Escape. *Journal of Cardiovascular Ultrasound*.

[99] N. Kumar, S. Balasundaram, M. Rickard, Z. Al Halees, and C. M. G. Duran. Leaflet embolisation from Duromedics valves: a report of two cases. *The Thoracic and Cardiovascular Surgeon*, 39(06):382–383, 1991.

[100] W. Klepetko, A. Moritz, J. Mlczoch, H. Schurawitzki, E. Domanig, and E. Wolner. Leaflet fracture in Edwards-Duromedics bileaflet valves. *The Journal of Thoracic and Cardiovascular Surgery*, 97(1):90–94, 1989.

[101] R. T. Knapp, J. W. Daily, and F. G. Hammitt. *Cavitation*. McGraw-Hill New York, 1970.

[102] C. E. Brennen. *Cavitation and bubble dynamics*. Number 44. Oxford University Press, 1995.

[103] F. R. Young. *Cavitation*. McGraw-Hill London, 1989.

[104] A. Z. Szeri. *Fluid film lubrication*. Cambridge University Press Cambridge, 2011.

[105] R. P. Zubarev, E. V. Kolpakov, G. V. Morov, and R. Gabeskiriia. Problems of thrombogenesis and destruction of the superficial layer of implanted artificial heart valves. *Meditsinskaia Tekhnika*, (4):26, 1976.

[106] P. Johansen. Mechanical heart valve cavitation. *Expert Review of Medical Devices*, 1(1):95–104, 2004.

[107] R. Kafesjian, M. Howanec, G. D. Ward, L. Diep, L. S. Wagstaff, and R. Rhee. Cavitation damage of pyrolytic carbon in mechanical heart valves. *The Journal of Heart Valve Disease*, 3:S2, 1994.

[108] T. Graf, H. Reul, C. Detlefs, R. Wilmes, and G. Rau. Causes and formation of cavitation in mechanical heart valves. *The Journal of Heart Valve Disease*, 3:S49, 1994.

[109] T. Graf, H. Fischer, H. Reul, and G. Rau. Cavitation potential of mechanical heart valve prostheses. *The International Journal of Artificial Organs*, 14(3):169, 1991.

[110] C. S. Lee, K. B. Chandran, and L. D. Chen. Cavitation dynamics of medtronic hall mechanical heart valve prosthesis: fluid squeezing effect. *Journal of Biomechanical Engineering*, 118(1):97–105, 1996.

[111] A. D. Haubold, J. L. Ely, and G. L. Chahine. Effect of cavitation on pyrolytic carbon in vitro. *The Journal of Heart Valve Disease*, 3(3):318–323, 1994.

[112] Z. Jon Wu, M. C. S. Shu, D. R. Scott, and N. H. C. Hwang. The closing behavior of Medtronic Hall mechanical heart valves. *ASAIO journal*, 40(3):M702–M706, 1994.

[113] Z. J. Wu, B. Z. Gao, and N. H. Hwang. Transient pressure at closing of a monoleaflet mechanical heart valve prosthesis: mounting compliance effect. *The Journal of Heart Valve Disease*, 4(5):553–567, 1995.

[114] L. A. Garrison, T. C. Lamson, S. Deutsch, D. B. Geselowitz, R. P. Gaumond, and J. M. Tarbell. An in-vitro investigation of prosthetic heart valve cavitation in blood. *The Journal of Heart Valve Disease*, 3:S8, 1994.

VITA

VITA

Kameswararao Anupindi was born on April 22, 1983 in Yelamanchili, Andhra Pradesh, India. He did his schooling, intermediate and undergraduate studies from Kakinada, Andhra Pradesh. He graduated with a degree in mechanical engineering from Jawaharlal Nehru Technological University College of Engineering, Kakinada in 2004. Subsequently, he pursued his post graduate studies from Indian Institute of Technology Kanpur, Uttar Pradesh, India. He graduated with a master of technology degree in Aerospace Engineering in the year 2006. He worked as a software development engineer on the FLUENT 12.0 project in the solver meshing team after his graduation in August 2006 until December 2009. In January 2010, he started his doctoral studies in the School of Mechanical Engineering, Purdue University, West Lafayette, IN, USA.